Drivers of Coastal Morphodynamics on a Deltaic Barrier in the Colombian Caribbean

by

Juan Felipe Gómez

A Dissertation Submitted in Partial Fulfillment of the

Requirements for the Degree of

DOCTOR OF PHILOSOPHY

in the Department of Geography

University of Victoria

We acknowledge and respect the Lək̓ʷəŋən (Songhees and Esquimalt) Peoples on whose traditional territory the university stands, and the Lək̓ʷəŋən and W̱SÁNEĆ Peoples whose historical relationships with the land continue to this day.

Drivers of Coastal Morphodynamics on a Deltaic Barrier in the Colombian Caribbean

by

Juan Felipe Gómez

Supervisory Committee

Dr. Eva Kwoll, Co-supervisor

Department of Geography

Dr. Ian Walker, Co-supervisor

Department of Geography

Dr. David Atkinson, Departmental Member

Department of Geography, University of Victoria

Dr. Edwin Nissen, Outside Member

School of Earth and Ocean Sciences

ABSTRACT

This research presents results from a series of analyses focussed on the overarching goal of identifying and understanding drivers of coastal morphodynamics on a deltaic barrier in the Colombian Caribbean coast, eastward from the Magdalena River mouth. Forcing mechanisms operating at different temporal scales were considered, including the influence of vertical land motion (VLM), storms, river discharge, trade winds, and wave conditions. These forcing mechanisms were related to geomorphic changes determined from satellite imagery taken before and after specific events.

Satellite imagery and synthetic aperture radar acquisitions were used to assess decadal-scale coastline changes and VLM for the period 2007–2021. The findings revealed that VLM rates are highly variable alongshore, and that subsidence occurs mainly landward of highly erosive stretches of coastline associated with former mangrove forest.

Drivers of coastal morphodynamics operating on time spans from days to seasons were assessed by focusing on four lagoons located along the back-barrier to better understand the interplay between extreme events and the breaching and healing of inlets that are temporarily formed between the lagoons and the ocean. Satellite data in conjunction with hourly readings from weather stations spanning the past 50 years helped to determine the conditions that enabled the breaching and healing processes to transpire in the lagoons. Aligned with the predominantly erosive regime along the study area, the findings indicated that the cumulative effect of the breaching and healing of the lagoons resulted in a deltaic barrier that has rolled over the lagoons, modifying their size over time.

The occurrence of meteotsunamis and their role in coastal morphodynamics was investigated using a wavelet analysis applied to water-level readings in three tide gauges for the period 2013–2022. After the discovery of one event with meteotsunami-like characteristics, the atmospheric conditions and total water levels associated with this event were analyzed. The results indicated that total water levels related to the meteotsunami are similar to those produced by moderate storms and both phenomena can induce breaching of lagoons.

To date, the barrier has responded to external forcers through a landward displacement of the coastline driven by cycles of lagoon breaching and healing as well as overwashes on lagoons, wetlands, and beaches. Seasonal storms have been critical in forcing these processes and have substantially influenced the barrier evolution during the last 50 years. Taken as a whole, this body of work provides knowledge about the response of deltaic barriers to geomorphologic forcers based on a study area in an understudied region of the Caribbean. At a regional level, the findings are relevant for science-based coastal planning and managing policies. Moreover, this research used a variety of methodological approaches to track causality on coastal landscapes in a

manner that can be replicated in other areas with limited pre-existing information and without ongoing monitoring programs.

Contents

List of Figures

List of Tables

List of Equations

List of Appendices

Acknowledgements

Far from being a solo journey, this thesis is a collective effort that was benefited from the collaboration of many colleagues, family and friends in Colombia and Canada.

I have been fortunate in having the continual advice and encouragement of two academic advisors that come from different fields. As such, I am equally grateful to Dr. Ian Walker and Dr. Eva Kwoll.

My career would have taken a very different path had Ian not accepted me as part of his laboratory at the University of Victoria. By pushing me beyond my intellectual comfort zone, Ian helped me to put together the backbones of this thesis. I am inspired by his gentle approach to teaching and endless curiosity about coastal morphodynamics.

Eva's guidance was crucial to consolidate into doable manuscripts the different chapters of this manuscript. Thanks to Eva's support, I was able to run endless uncommented lines of code. I will be always beholden to Eva for her support in cleaning out the weeds of this project to get the big picture and amazed by her capacity to work for long hours, no matter the conditions, until the work is done.

My other two committee members, Dr. David Atkinson and Dr. Edwin Nissen, were always available to promptly answer my questions and guide me to find data and see evidence, that otherwise, would have remained unrevealed to me. I hope that this thesis reflects the high standards that my committee set.

I also want to express my gratitude to Dr. Andrew Cooper at Ulster University for the external evaluation of my dissertation.

During various stages of this project, I felt pleasantly surprised by the collaborative spirit of many academics that, without any interest beyond pure altruism and scientific curiosity, gave me support and guidance to improve the articles included in this manuscript. Despite the uncharted waters that we all navigated before and during the lockdown period, Dr. Manoochehr Shirzaei (Manoo) always showed up for our weekly meetings and patiently walked me through the programs he had created to assess vertical land motion. I am extremely indebted to him for all his teaching and collaboration with my work.

I have not met personally Dr. Alexander Rabinovich and Dr. Jadranka Šepić. Yet, the advice and suggestions provided through emails were fundamental to improve Chapter 4 and to access literature that was previously unknown for me. I appreciate their gracious insights. I also want to express my appreciation to Dr. Gregory Dusek at NOAA, who provided me with codes that were fundamental for the development of Chapter 4.

I am equally grateful to the following colleagues and friends at UVic, who just by listening to my initial ideas and providing insights, gave me support during the project: Daniel Brendle-Moczuk, Alison Root, Amanda Wild, Alex Lausanne, Alana Rader, Michael Grillot, Katie Hughes, Derek Heathfield, Narges Raee, Wyatt Maddox, Kinga

Menu, Rick Sykes, Robbie Newton, Felix Parkinson, Francisco Nieto, and K. Darcy Harrison. Special thanks are given to Dr. Jaime Ojeda, who, through extended conversations, provided advice with R codes and relevant references out of my field.

Thank you to Janette Delong and Sally Johnson, graduate secretaries in the Department of Geography, for all their assistance with administrative matters.

Dr. Robin Davidson-Arnott has been an inspiring professor and colleague since I met him in 2013. I truly appreciate Robin's support to start and finish my PhD program.

I would also like to recognize the contribution of the following professionals at Invemar, who encouraged me to start and move forward in the initial stages of this research: Blanca Posada, David Morales, Constanza Ricaurte, Julio Bohorquez, and Marco Elías González. In Dimar, Engineer Ruby Viviana Ortiz was always diligent in her efforts to facilitate access to information gathered at their stations. During the final stages of this project, Dr. Daniel Peters at ECCC, provided me with invaluable support and encouragement.

Field work developed in the study area would not have been feasible without the assistance of the staff at the facilities of Isla Salamanca National Park. Also, Professors Oscar Alvárez and María Isabel Vélez gave me advice and logistical support for field activities. Field assistants Evaristo Rada and Ismael Fernández took a break from their daily labours to join me in the field. Despite the long shifts and scorching sun, they were always caring and enthusiastic company.

The commitment and dedication to geological work of my Colombian friends, Edgar Jaramillo, Carlos Cuartas and Jorge González, have been a source of inspiration for my own work. In their own subtle ways, they taught me that it is possible to shine even during the darkest moments.

Together with my dad, mom and sister, we used to take the winding road from Medellín to Santa Marta, a city near the study site of this project, during the holidays. Back in the 1980s, Santa Marta was for me an exotic and pristine place for me. Through a few snapshots over the years, we witnessed first-hand the rapid transformation of the once natural beaches, coral reefs and lagoons into a tamed landscape. Many years later, I came back to Santa Marta for a job position and was unsettled by how little we knew (and continue to know) about the specific processes behind coastal erosion in the area. In a way, this project is the result of the time spent with my family in Santa Marta. No matter the detours taken, I have always counted on their support. Thank you for keeping me company and for your love Luz Helena and Diana. Las quiero mucho.

My wife, Luisa Fernanda Ramírez, has been always supportive throughout my doctorate program. Neither this manuscript, nor the many years that I invested gathering and processing data, would have been possible without her constant care and love.

Dedication

To my drivers, Luisa Fernanda and Abigail Lucia.

Chapter 1. Introduction

1.1 Background and Objectives

Coastal deltas occupy only 1% of the surface of the Earth, yet they are home to 6.7% of earth's inhabitants (Bianchi, 2016). Delta formation results when the deposition of sediment at the mouth of a river exceeds the redistribution of sediment by marine processes (Galloway and Hobday, 1983). In dynamic terms, deltas are coastal bulges formed where sediment input exceeds the combined effect of relative sea-level rise (hereafter, SLR) and the reworking capacity of marine processes (Swift and Thorne, 1991). In the absence of waves and tides, channel bifurcation and levees lead to the development of deltas with crenulated shorelines characteristic of fluvial-dominated processes. Wave-dominated deltas, in contrast, tend to have a smooth cuspate shape consisting of shoreline-parallel beach ridges (Nienhuis et al., 2015).

A landform frequently found fronting deltas are barrier islands, a type of barrier disconnected from the mainland by a lagoon, a bay, a saltmarsh or wetland; barrier islands usually have inlets between the islands or from a laterally adjacent mainland (Hesp and Short, 1999). Deltaic barrier are those which genesis is closely related to a river mouth and its sediment supply. About 30% of barrier islands are deltaic barriers, which accounts for a total global length of over 4000 kilometers (Stutz and Pilkey, 2002).

Understanding the current assemblage of a coastal landscape, such as a deltaic barrier, requires recognizing that different processes within coastal systems operate at different temporal and spatial scales (Murray-Wallace and Woodroffe, 2014; Pugh and Woodworth, 2014; van Heteren, 2014). While some of these processes last only minutes (tsunamis) or days (storms, hurricanes), others influence the landscape over decades (subsidence) to centuries or millennia (crustal movements) (Figure 1). Predictions of barrier-system behaviour at timescales of decades to centuries have far-reaching implications for society due to the location of human infrastructure on, or next to, barrier systems (Cooper et al., 2018). Nevertheless, the interplay of drivers influencing barrier behaviour for different timescales is still insufficiently known (van Heteren, 2014), and research that integrates knowledge at distinct spatial-temporal scales is still uncommon (Walker et al., 2017). Currently, numerical, conceptual, and analytical modelling in conjunction with real-world observations provide the bases for short- (days to seasons) and long-term (centuries to millennia) model parameterizations, simulated prototypes, and tests for model results (Moore and Murray, 2018).

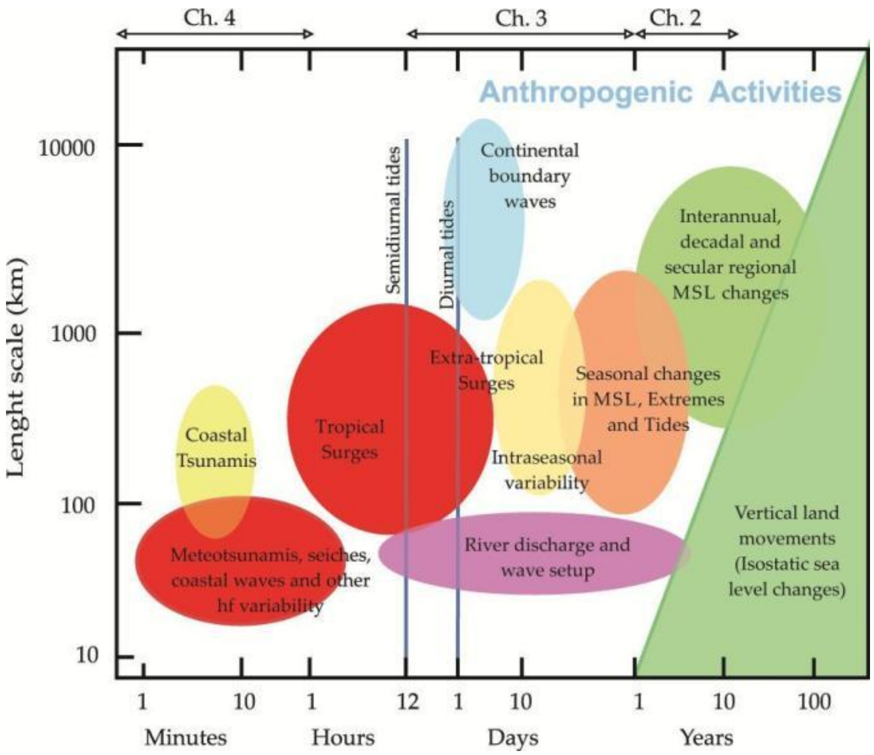

Figure 1. Drivers of barrier morphodynamics and their interaction at different spatial and temporal scales. Processes operating at a range of temporal and spatial scales are addressed in Chapters 2, 3, and 4 (Modified from Pugh and Woodworth, 2014).

As early as the 1970s, it has been recognized that, driven by overwashes and inlet breachings, coastal barriers can migrate landward (or roll over) when facing external forcers such as sea-level rise, frequent storms, or a reduction in sediment supply (Swift, 1975; Leatherman et al., 1977; Leatherman, 1979). The rates of landward sediment transport via overwashes and temporary breaches are critical to allow narrow barriers to keep pace with rising sea levels (Leatherman, 1979).

Whether a barrier migrates landward or drowns in place has been modelled for different sea-level rise scenarios and barrier configurations (e.g., Moore et al., 2010; Lorenzo-Trueba and Ashton, 2014; Ashton and Lorenzo-Trueba, 2018; Portos-Amill et al., 2023). Recently developed numerical models have recognized that the most influential parameters on barrier drowning are the rate of SLR and significant wave height; whereas SLR is notable as an increase in the width and/or number of inlets on barriers, higher waves result in more frequent inlet closures and more rapid barrier drowning (Portos-Amill et al., 2023). Despite the increasing sophistication of computer models to better understand the dynamics of barrier systems, the response of a barrier to the interplay of multiple forcing mechanisms acting at different spatial-temporal scales has not been fully constrained. For example, on the timescales ranging from decadal to millennia, which are the most relevant for barrier formation and evolution, accounting for the variability in intensity and direction of flows, particularly for wind waves and swell, and how this variability relates to shoreface dynamics over time has not been parameterized (Cowell and Kinsela, 2018). Furthermore, barrier models such as BRIE-D, although able to reproduce many of the variables involved in barrier dynamics, simplify reality by rendering overwash transport independent of wave height (Portos-Amill et al., 2023).

Accordingly, the incorporation of well-constrained process-response relationships from onshore data as well as historical reconstructions is a complementary approach to numerical models and the foundation for running prototype conditions to test the reliability of simulations. This dissertation is an observation-based investigation that examines different drivers of coastal morphodynamics and how they have contributed to shaping the subaerial fringe of a highly erosive deltaic barrier. Specifically, by analyzing the forcers of change on a deltaic barrier including data gathered since 1973, this project aims to better understand the role that individual drivers operating at different spatial and temporal scales have played on the current configuration of a deltaic barrier. The research objectives are as follows:

1. Establish the role that vertical land motion (VLM) has played in the evolution of the coastal area and to relate the findings to historic coastal changes.

2. Evaluate the forcing mechanisms that favour lagoon breaching and healing in a microtidal environment.

3. Investigate the role of meteotsunamis as an external forcing of coastal morphodynamics and provide insights of the conditions under which meteotsunamis occur in the Colombian Caribbean.

4. Provide feasible methodological approaches to track coastline morphodynamics in areas with limited pre-existing information and lack of ongoing monitoring programs.

1.2 Background and Dissertation Structure

This research examines instantaneous (minutes to hours), short- (days to seasons) and medium-term drivers (years to half centuries) of coastal dynamics along a stretch of coast where coastal retreat and accretion processes have been instrumental in shaping a deltaic barrier at least since the 1960s (von Erffa, 1973). The deltaic barrier is located in a relative pristine coastal National Park in the Colombian Caribbean, encompassing 60 kilometers of shoreline eastward from the Rio Magdalena mouth, the largest watershed (257,438 km^2) and longest river (1,612 km) in Colombia (Restrepo et al., 2006). The park, together with the lagoon known as Ciénaga Grande de Santa (CGSM), were designated as Ramsar site and UNESCO Biosphere Reserve in 1998 and 2000, respectively (Figure 2).

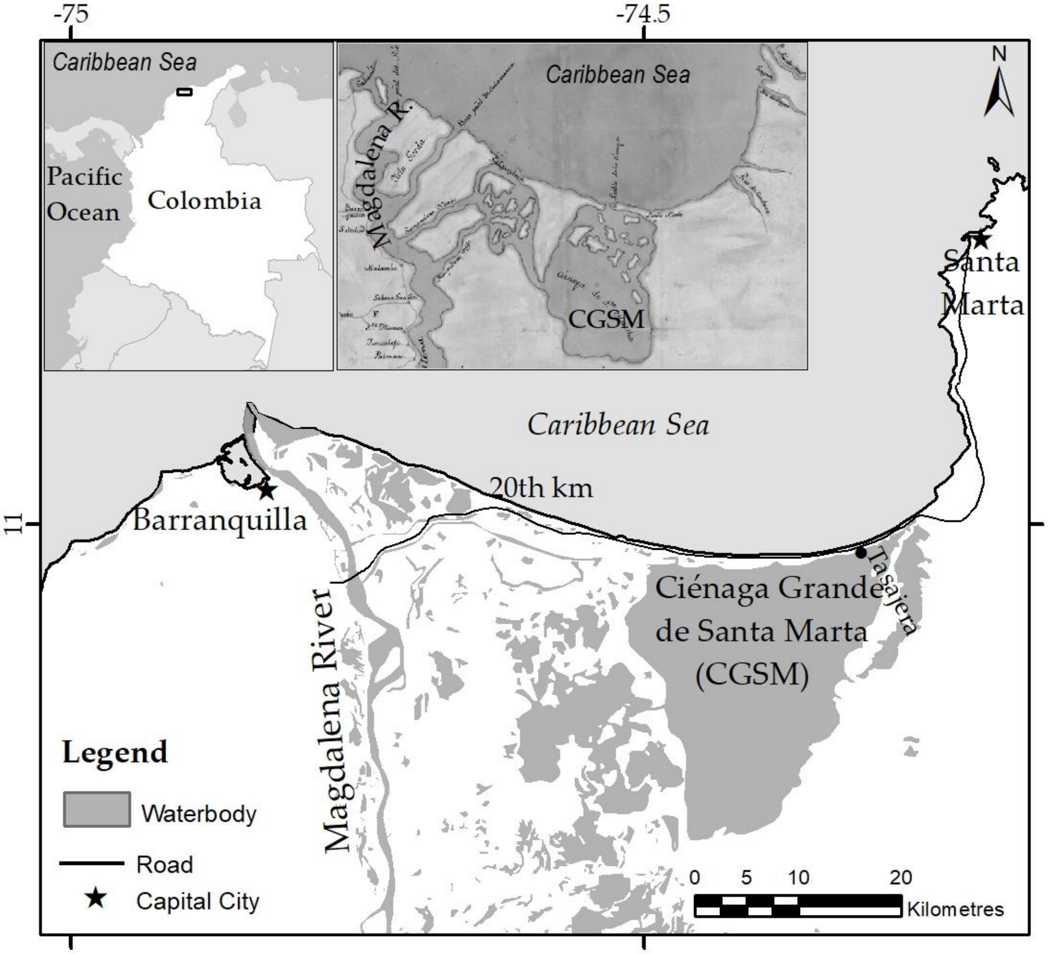

Figure 2. Study area. The Magdalena River mouth and its associated wetlands are located in north Colombia, east of Barranquilla. The CGSM is the largest lagoon in Colombia (approx. 4000 km^2).The inset in the middle illustrates the study area as depicted in a map dating from 1766 (Modified from Gómez et al., 2016).

The major anthropogenic interventions within the area are the development of a port starting in 1925 (Rico, 1967) that included the building of two levees on each side of the river mouth, and the construction of a road parallel to the coastline in the 1950s to connect the nearby cities of Barranquilla and Santa Marta (Figure 2). Together, these interventions modified the otherwise natural sediment supply distribution into the delta and hampered the interchange of waters between ocean and back-barrier lagoons, resulting in widespread mangrove mortality in the 1980s (Elster et al., 1999).

The decision to build this infrastructure, in conjunction with the cumulative effect of other small decisions (*sensu* Odum, 1982) such as armoring sections of the coastline with rip-rap or the conversion of small tracts of wetlands associated with the Ciénaga Grande de Santa Marta for livestock, have had long-lasting environment impacts on the barrier. Particularly, the construction of the harbour and its associated jetties was a crucial point in driving the transition from fluvial to wave-dominated conditions along the deltaic system (Gómez et al., 2016).

In addition to the broad diversity of research investigating patterns of barrier island evolution (e.g., Dillenburg and Barboza, 2009; Lentz et al., 2013; Fruergaard and Kroon, 2016; Conery et al., 2018), sediment transport across barriers (e.g., Hudock et al., 2014; Sherwood et al, 2014; Lazarus, 2016; Zăinescu et al., 2019) and their response to past (e.g., Rampino and Sanders 1981; Storms et al., 2008; Hein et al., 2013) and predicted sea-level changes (e.g., Ashton and Lorenzo-Trueba, 2018; Portos-Amill et al., 2023), this dissertation builds on previous work in the study area that mapped coastal landforms, identified vegetation associated with accretive and erosive regimes along the coastline, and assessed coastline changes over time (von Erffa, 1973; Bernal, 1996; Gómez, 2015; Gómez et al., 2016).

A portrait of the modern and Holocene evolution of the Magdalena River delta was obtained using historical maps dating back to the early 1800s (Gómez et al., 2016), and offshore seismic profiles (Romero-Otero et al., 2015). An analysis of more recent coastal changes in the delta helped to envision the negative impact that erosive processes would have over the road that crosses the park by the 2000s (von Erffa, 1973).

The analysis of the complexities associated with the spatial-temporal drivers that influence the barrier is tackled using a multifaceted approach that laid out in three distinct but related manuscripts. Overlaying the reductionist approach followed throughout this project exists a recognition that the current configuration of the study area is the result of the overlapping influence of the geomorphological processes investigated in Chapters 2–4 added to others that are out of the scope of this research (e.g., eustatic sea-level changes, global atmospheric circulation patterns, ecological interactions, underlying geology, nearshore processes).

In Chapter 2, I address a medium term driver of coastal morphodynamics. The primary aim of this manuscript is to assess vertical land motion (VLM) and how it relates to coastal morphodynamics (Gómez et al., 2021). Rates of VLM were quantified using interferometric synthetic aperture radar (InSAR), and their spatial distribution related to recent coastline changes measured over satellite imagery.

In Chapter 3, I provide an analysis of short-term drivers of coastal evolution, including the effect that storms and washouts have had in the evolution of four lagoons behind stretches of a deltaic barrier regime that range from accretive to erosive (Gómez et al., 2023). This chapter aims to improve our understanding of historical coastline change and how lagoon morphology adjusts to short-term drivers of geomorphological change. Satellite imagery, in combination with hourly readings from meteorological and oceanographic stations, support the findings of Chapter 3.

In Chapter 4, I investigate an event that produced tsunami-like waves which resulted in the flooding of coastal areas in the study area. By using radar data and readings from meteorological and oceanographic stations prior to and during the event, I aim to elucidate the mechanisms that forced the sudden short-lived sea-level oscillation as well as to quantify total water levels associated with this event.

Chapter 5 goes over the key factors driving coastal morphodynamics in the study area, which points to the relative importance of the studied drivers and suggests future paths to develop research based on the response of lagoons to the drivers of change.

Collectively, the findings of this dissertation aim to provide a more complete understanding of the influence of a range of temporal drivers on the recent changes of a highly dynamic deltaic barrier in order to support evidence-based policymaking.

Chapter 2. Vertical land motion as a driver of coastline changes on a deltaic system in the Colombian Caribbean

Chapter published on July 20, 2021 as:

Gómez, J.F., Kwoll, E., Walker, I.J., Shirzaei, M., 2021. Vertical Land Motion as a Driver of Coastline Changes on a Deltaic System in the Colombian Caribbean. Geosciences 11, 300. https://doi.org/10.3390/geosciences11070300

Abstract

To face and properly mitigate coastal changes at a local level, it is necessary to recognize and characterize the specific processes affecting a coastline. Some of these processes are local (e.g., sediment starvation), while others are regional (e.g., relative sea-level change) or global (e.g., eustatic sea-level rise). Long tide gauge records help establish sea-level trends for a region that accounts for global (eustatic, steric) and regional (isostatic) sea-level changes. Local sea-level changes are also the product of vertical land motion (VLM), varying depending on tectonic, sedimentological, and anthropogenic factors. We investigate the role of coastal land subsidence in the present-day dynamics of a delta in the Colombian Caribbean. Satellite images and synthetic aperture radar acquisitions are used to assess decadal-scale coastline changes and subsidence rates for the period 2007–2021. We found that subsidence rates are highly variable alongshore. Local subsidence rates of up to −1.0 cm/yr correspond with an area of erosion rates of up to −15 m/yr, but coastal erosion also occurs in sectors where subsidence was not detected. The results highlight that local coastline changes are influenced by multiple, interacting drivers, including sand supply, coastline orientation and engineering structures, and that subsidence alone does not explain the high rates of coastal erosion along the study area. By the end of the century, ongoing coastal erosion rates of up to −25 m/yr, annual rates of subsidence of about −1 cm/yr, and current trends of global sea-level rise are expected to increase flooding levels and jeopardize the existence of the deltaic barrier island.

Keywords: sea-level rise; InSAR; Magdalena River; coastal changes; subsidence; mangroves; sediment compaction.

2.1 Introduction

The Intergovernmental Panel on Climate Change forecasts rates of sea-level rise (SLR) between 8 and 16 mm/yr by the end of the century, resulting in a global sea-level rise between 0.52 to 0.98 m for a high greenhouse gas emission scenario (Church et al., 2013). Adding to the predicted increases of global mean sea level (GMSL), the upward or downward movement of the land surface—also known as vertical land motion (VLM)—may exacerbate relative sea-level (RSL) changes at local scales. Changes in RSL result from the combined effect of the mean sea-level height (i.e., GMSL) and VLM (Gregory et al., 2019), and it is measured relative to a local tide gauge benchmark (Pugh, 2004). The most common triggers of VLM are glacial isostatic adjustments (GIA), earthquakes and tectonics, aquifer compaction and sediment consolidation (Pugh, 2004; Pugh and Woodworth, 2006). Where VLM takes place near the coast, it may modify the coastline by the emergence or submergence of the terrain (Gregory et al., 2019), resulting in, for example, shoreline progradation or retreat, respectively. Within the various causes of VLM, this work focuses on subsidence, defined as the downward movement of the land surface with respect to a datum or point of reference (Dokka, 2006), and how it relates to coastal morphodynamics. Subsidence is driven by factors such as natural sediment compaction (Zoccarato et al., 2018), fault displacements (Dokka, 2006), or human actions (e.g., groundwater extraction (Minderhoud et al., 2020) withdrawal of petroleum and natural gas (Yuill et al., 2009), soil desiccation (Dixon and Dokka, 2008).

Deltas are common coastal landforms formed by the deposition and reworking of sediments from river systems where they enter larger bodies of water, such as oceans or lakes. Worldwide, most large deltas are subsiding at rates faster than the present global sea-level rise (Syvitski et al., 2009). In the case that abundant sediment supply exists, a trade-off can be established between sediment delivery and subsidence in deltaic areas: the sediment deposition that triggers subsidence also helps compensate for or exceeds the subsidence. For instance, in some locations of the Mekong Delta in Vietnam, sediment accretion exceeds compaction rates, resulting in a net elevation gain of the delta surface (Zoccarato et al., 2018). However, when the delivery of fluvial sediment supply decreases, sediment compaction is no longer balanced by sediment deposition (Zoccarato et al., 2018). In this case, as the sediment matrix compresses and dehydrates, fluid pressure decreases and organic carbon-rich materials, if present, oxidize to carbon dioxide, resulting in a total mass and volume loss within the soil column (Dixon and Dokka, 2008) (Figure 3). Törnqvist et al. (2008) noted that, adding to the sizeable natural component of subsidence due to isostatic flexure and the compaction of young sediments, subsidence caused by artificial drainage of wetlands and groundwater withdrawal can be up to an order of magnitude faster. For instance, using interferometric synthetic aperture radar (InSAR), VLM of up to −8 mm/yr have been measured in the coastal plain of the Selle River mouth (southern Italy) (Di Paola et al., 2018) and of up to −5 mm/yr in the Tiber Delta in Rome (Polcari et al., 2018). Additionally, Zhang et al. (2015) reported average VLM rates of −5.1 mm/yr in the modern Yellow River Delta from 1992 to 2000.

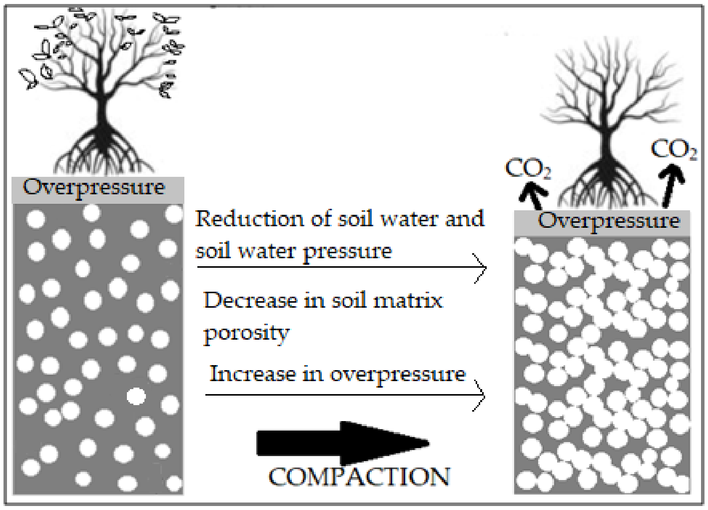

Figure 3. Properties of soil structure before (left) and after (right) compaction takes place. Emission of CO_2 occurs when dehydrated organic-rich soils are exposed to atmospheric oxygen (modified from Yuill et al. (2009)).

Whilst the role of subsidence as a natural driver of delta growth and abandonment has been recognized and coined as the cyclic evolution of deltas (Roberts, 1997), its influence in the evolution of coastal landscapes and the seaward progradation (i.e., accretion) or landward retreat (i.e., erosion) of coastlines has not been fully addressed. Despite subsidence being recognized as one of the key controls on coastline changes (El-Fishawi, 1989; Anthony et al., 2015; Polcari et al., 2018), the majority of research has focused on the added impact of current subsidence rates and rising sea levels for future scenarios of inundation and erosion (e.g., Di Paola et al., 2018; Shirzaei and Bürgmann, 2018). However, local-scale studies can help to better understand how VLM (subsidence or emergence) translates to coastline changes and related geomorphic responses. Accordingly, this study aims to support evidence-based policymaking by (i) testing the application of InSAR interferometry to estimate the rates and spatial distribution of VLM in a coastal setting, and (ii) linking VLM to recent coastline evolution derived from satellite imagery along a deltaic barrier.

2.1.1 Study Site

The study area is located in the Colombian Caribbean, between the municipalities of Ciénaga and Barranquilla (Figure 4). The area extends 70 km along the coastline eastward from the mouth of the Magdalena River. As the largest basin in Colombia, the Magdalena River and its tributaries cover 257,438 km^2 (Restrepo et al., 2006) and its discharge averages 10,287 and 4,068 m^3/s during high and low flows, respectively (Torregroza-Espinosa et al., 2020). Eight major shifts in delta location have been reported for the river since the Pliocene, the latest of which has occurred since the mid-

Holocene, by way of a westward migration of a former river mouth located by the Ciénaga Grande de Santa Marta (hereafter CGSM) to its present location (Romero-Otero et al., 2015) (Figure 4). Adding to the natural displacement of the delta, human-made structures associated with a harbor built in the 1920s near the mouth of the river have confined its mouth to a single channel, thus further reducing the present influence of the Magdalena River in the study area (von Erffa, 1973). Moreover, a highway built next to the coastline in the 1950s to connect the cities of Barranquilla and Santa Marta formed a causeway for the otherwise free interchange of water between ocean and lagoons, producing accelerated degradation and mortality of mangrove forest due to hypersalinization (Elster et al., 1999).

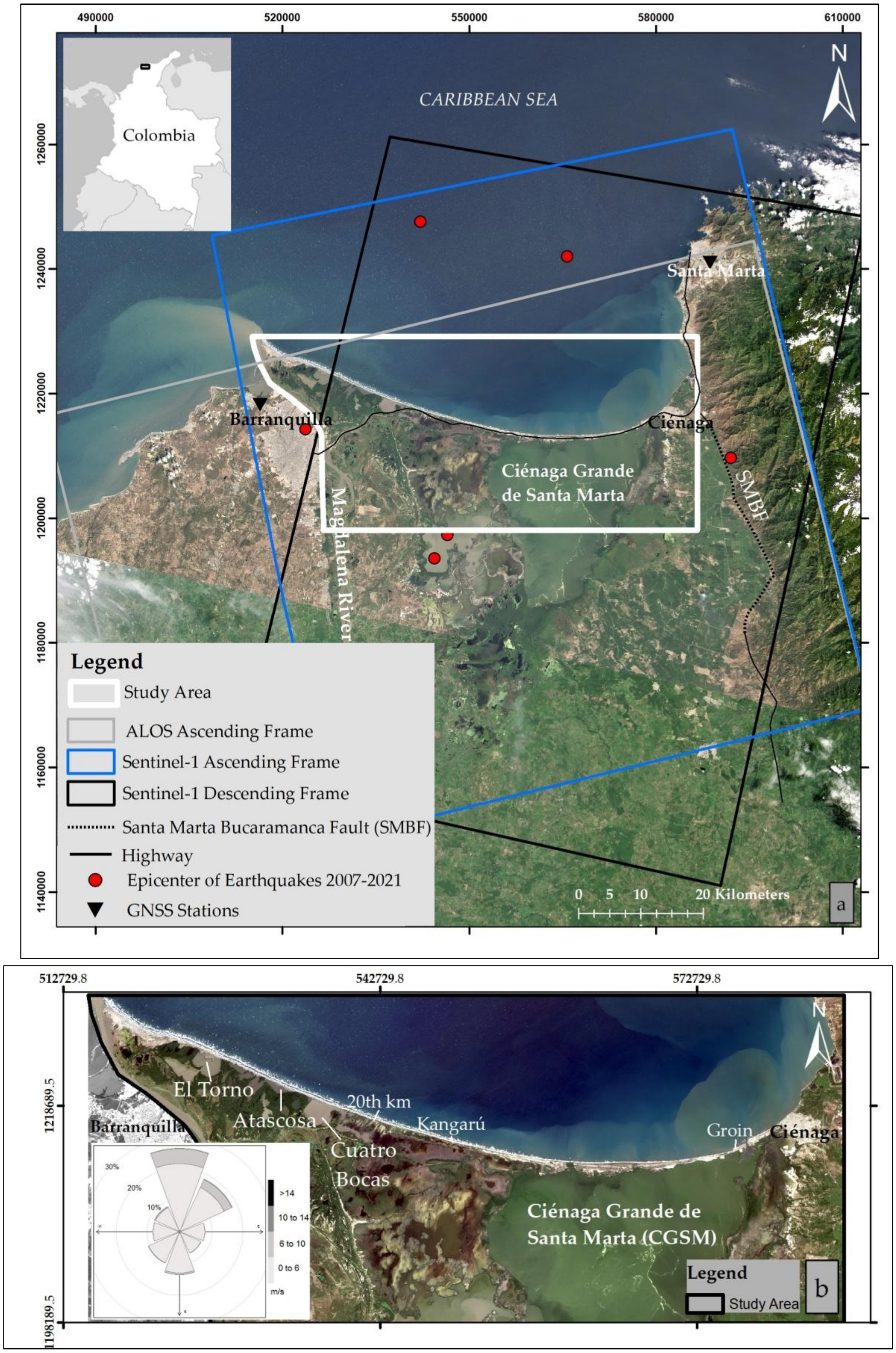

Figure 4. Study area and its surrounding wetlands and lagoons; (a) the epicenters of earthquakes and the coverage of ALOS and the Sentinel-1A/B ascending and descending radar data are included. The study site extends from the River Magdalena

mouth (west) to the town of Ciénaga (east); (b) detail of the study area indicating the locations referred to in the manuscript. The wind rose displays the distribution of wind speed and direction for the study site.

The conditions described above have favored a transition of the landscape from fluvial to littoral-dominated process, portrayed by a palimpsest of fluvial and marine landforms such as channels, lagoons, oxbow lakes, salt plains, beaches, and dunes shaped by the predominant northeasterly trade winds (Gómez et al., 2016) (Figure 4). Following Oertel (1985), the landforms required to make up a barrier island system are present in the study area (i.e., mainland, back-barrier lagoon, barrier island, barrier platform, shoreface, inlets and inlet deltas). The sediments associated with these landforms, originated in marine and fluvio-lacustrine environments (Hernández, 1999), range from poorly consolidated sands along the shorefront to laminated muds within lagoons and in the backshore. These Holocene sediments are bounded on the east side by the Santa Marta Bucaramanga Fault (SMBF), a regional-scale striking left-lateral structure that extends 374 km from the Caribbean coast to the eastern range of Colombia (Figure 4a) (Paris and Machete, 2000; Idárraga-García and Romero, 2010). The fault marks a contrasting relief change between the Sierra Nevada de Santa Marta range east of the structure, and the flat topography of the Magdalena Delta floodplain to the west. According to the records of seismological activity in the area, there is no evidence of significant earthquakes associated with the SMBF with magnitudes (mb) larger than 4.9 since instrumental records are available (i.e., 1984). The few earthquakes registered for the observational period have magnitudes (mb) of less than 4.6 (USGS, 2009) (location of epicenters shown in Figure 4a).

Rapid coastline changes have been identified in the study area since the 1950s, affecting natural and human resources; specifically, coastal erosion rates increase alongshore in the same direction as the littoral drift (east–west) (Gómez et al., 2016). Chronic erosion is threatening the highway that connects the cities of Barranquilla and Santa Marta and, consequently, a rock rip-rap structure was built in 2014 to protect the highway from continuous erosive processes in a point known as the 20th km (the 0 km is located at the outskirts of Barranquilla) (El Heraldo, 2021) (Figure 4). This hard structure has fixed the coastline in that area, but adjacent sectors keep rapidly retreating landward. The causes of coastal retreat have not been fully identified. A regional analysis of the sea-level trends for the Caribbean coast between 1950 and 2001 found a statistically significant sea-level rise trend of approximately 2 mm/yr (Lozada et al., 2013). Moreover, a sea-level rise of 5.3 ± 0.3 mm/yr between 1950 and 2010 was measured at a tide gauge station located in Cartagena, approximately 100 km southeast of the study site (Andrade et al., 2013), which indicates that, in addition to regional sea-level rise, there might be additional drivers contributing to the observed coastal retreat. GPS-derived subsidence trends revealed values ranging between −2.85 ± 0.84 mm/yr and −5.71 ± 2.18 mm/yr in the same city for the period 2016−2020 (Restrepo-Angel et al, 2021). The influence of the rate of RSL change on barrier behavior is not completely understood, but some of the known effects of RSL rise include reworking of sand eroded from barrier fronts into transgressive dunes and shifts in sediment supply due to the modification of slope and course of rivers (van Heteren, 2014).

2.2 Materials and Methods

A two-fold approach was followed: (i) coastline changes were assessed using the USGS Digital Shoreline Analysis System (DSAS) tool (Thieler et al., 2009) for 2010–2020, and (ii) VLM rates were quantified using Synthetic Aperture Radar (SAR) interferometric analysis of images acquired for the periods 2007–2011 and 2017–2021. The results of these approaches were illustrated and contrasted to establish the relationship between coastline changes and VLM.

2.2.1 Coastline Changes

Satellite images taken by GeoEye-1 and SkySat-1 platforms with 5 and 3 m ground pixel resolutions, respectively, were used to trace coastlines between 2010 and 2020. Using this imagery, past coastlines were visually delineated along the limit between wet and dry sediment. This well-established methodological approach (Dolan, 1981; Moore, 2000; Boak and Turner, 2005) provides a proxy for the mean high water line (MHWL). Once a set of coastlines were established, changes were quantified using DSAS (Thieler et al., 2009). From the various statistics that DSAS produces, the average-of-rates (AOR) method, obtained by averaging the values resulting from the distance between each pair of available coastlines divided by the time between surveys, was selected to assess the rates of coastline changes over time. The AOR values were processed for transects spaced at 100 m intervals, perpendicular to a reference baseline traced parallel to the coastline. Accordingly, for two consecutive years, the accuracy of the coastline position depends on the image resolution (5 or 3 m), the georeferencing error (estimated to be 1 m), and a physical component of the error related to the magnitude of the tidal changes and slope of the beach (as intertidal range/tan (slope)) (Del Río, 2012; Anthony et al., 2015). The latter was assessed by using an average beach slope of 9.0° (pers. obs. June/2019), and a maximum intertidal range of 0.4 m. Determining the quadratic sum of each of these components yielded an annual maximum uncertainty for coastline change estimates of ± 5.0 m/yr.

2.2.2 Vertical Land Motion Rates

SAR images from the Advanced Land Observing Satellite (ALOS) L-Band and Sentinel-1A/B C-Band satellites (search.asf.alaska.edu) were gathered for the periods July 2007 to February 2011 and February 2017 to February 2021, respectively (see details in Table 1). The ALOS data were acquired along ascending orbit geometry, whereas ascending and descending orbits acquisitions were used for Sentinel-1. Interferograms for selected pairs of images were created and unwrapped using GAMMA, an InSAR processing software (Werner et al., 2000). The analysis began with co-registering Single Look Complex (SLC) images to a reference image, which includes a standard matching algorithm using a digital elevation model (DEM), precise orbital parameters, and amplitude images (Sansosti et al., 2006). For the Sentinel-1A/B datasets, the step above was followed by an enhanced spectral diversity (ESD) approach (Yague-Martínez et al., 2016; Shirzaei and Bürgmann, 2017). Using this dataset, a set of high-quality interferograms was generated, where only those interferograms with short perpendicular and temporal baselines were processed. A multi-looking operator of 20 and 4 pixels in range and azimuth was applied to obtain a ground resolution cell of approximately 46.0 m × 56.4 m (Table 1). The corresponding figures for ALOS are 6 and 3 pixels in range and azimuth, resulting in a ground resolution of 38.5 m × 23.6 m (Table 1).

Table 1. Parameters used to create interferograms during InSAR processing.

Condition	ALOS	Sentinel-1A/B
Acquisition dates	2007–2011	2017–2021
Path	143/144	77/142
Frame	200	32/555
Baseline distance (m)	1000	500
Temporal distance (days)	600	400
Azimuth looks	3	4
Range Looks	6	20
Images	13	50/53
Pairs selected	7	63
Incidence angle (°)	38.8	34.0
Heading angle (°)	348.8	347.9/192.0

To calculate and remove the effect of topographic phase and flat earth correction (Franceschetti and Lanari, 1999), a 1-arcsecond (~30 m) Shuttle Radar Topography

Mission DEM (Farr et al., 2007) and precise satellite orbital information were used. To identify the elite (i.e., less noisy) pixels, only those pixels with average coherence larger than 0.65 were considered in the analysis, a value that has been used in coastal landscapes with conditions similar to the study area (Di Paola et al., 2018; Amato et al., 2020). To retrieve the absolute (unwrapped) phase values, a minimum cost flow (MCF) algorithm adapted for sparsely distributed elite pixels was applied (see unwrapping in Figure 5). Although the precise orbits are used, a few interferograms were still affected by a ramp-like signal, which was removed by fitting a second-order polynomial to their unwrapped phase (Shirzaei and Walter, 2011). Several wavelet-based filters were further applied to correct for effects of spatially uncorrelated topography error and topography correlated atmospheric delay (Shirzaei and Bürgmann, 2018) (see atmospheric and orbit correction in Figure 5). Subsequently, a re-weighted least square approach was iteratively applied to invert the corrected measurement of the unwrapped phase at each elite pixel and solve the surface deformation time series. The effect of residual atmospheric errors was further reduced by applying a high pass filter based on continuous wavelet transform to the time series of surface deformation at each elite pixel. Finally, an estimate of the long-term line-of-sight (LOS) deformation rate was obtained as the best-fitting linear slope (hereafter velocity) to the time series of surface deformation at each elite pixel. Together with the LOS velocities, an estimation of the residuals for each elite pixel is provided by plotting the standard deviation of the LOS velocities.

For the Sentinel-1A/B dataset, by combining the ascending and descending LOS velocities in Equation 1, the vertical velocities were retrieved in Cartesian coordinates over those areas where scatterers of both tracks overlap or are in close proximity (Vilardo et al., 2009).

$$dz \approx (DlosAsc+DlosDesc)/2\cos\theta \qquad (1)$$

where DlosAsc and DlosDesc are the LOS velocities along the ascending and descending orbits, θ is the incidence angle, and dz is the projection of the displacement along the vertical Cartesian axis.

Only the Sentinel-1A/B dataset, therefore, yielded true estimates of VLM. In the case of ALOS data, a qualitative comparison was carried out between its LOS velocities and those obtained after processing the Sentinel-1A/B dataset. It should be noted that in using LOS velocities, the horizontal and vertical velocities are not separated for the observed period. The qualitative comparison between the velocities was made after performing an inverse distance weighted (IDW) interpolation model for transforming the discrete points representing VLM and LOS velocities of individual scatterers into a continuous surface. IDW has been used to interpolate InSAR scattered data points where a relationship or influence over neighboring data is not proven (Vilardo et al., 2009). After running the IDW using a 120 m neighborhood search radius weighted with a cubic exponential power, a 100 m resolution, continuous velocity surface was obtained. A Moran's I test was used to support the choice of distances above for the IDW interpolation. The steps and parameters to obtain the VLM are summarized in Table 1 and Figure 5. Lastly, aggregations of both the VLM and coastline change transects at 1.5 and 5 km resolutions were performed to examine the effect of scale on our observations (Appendix 1).

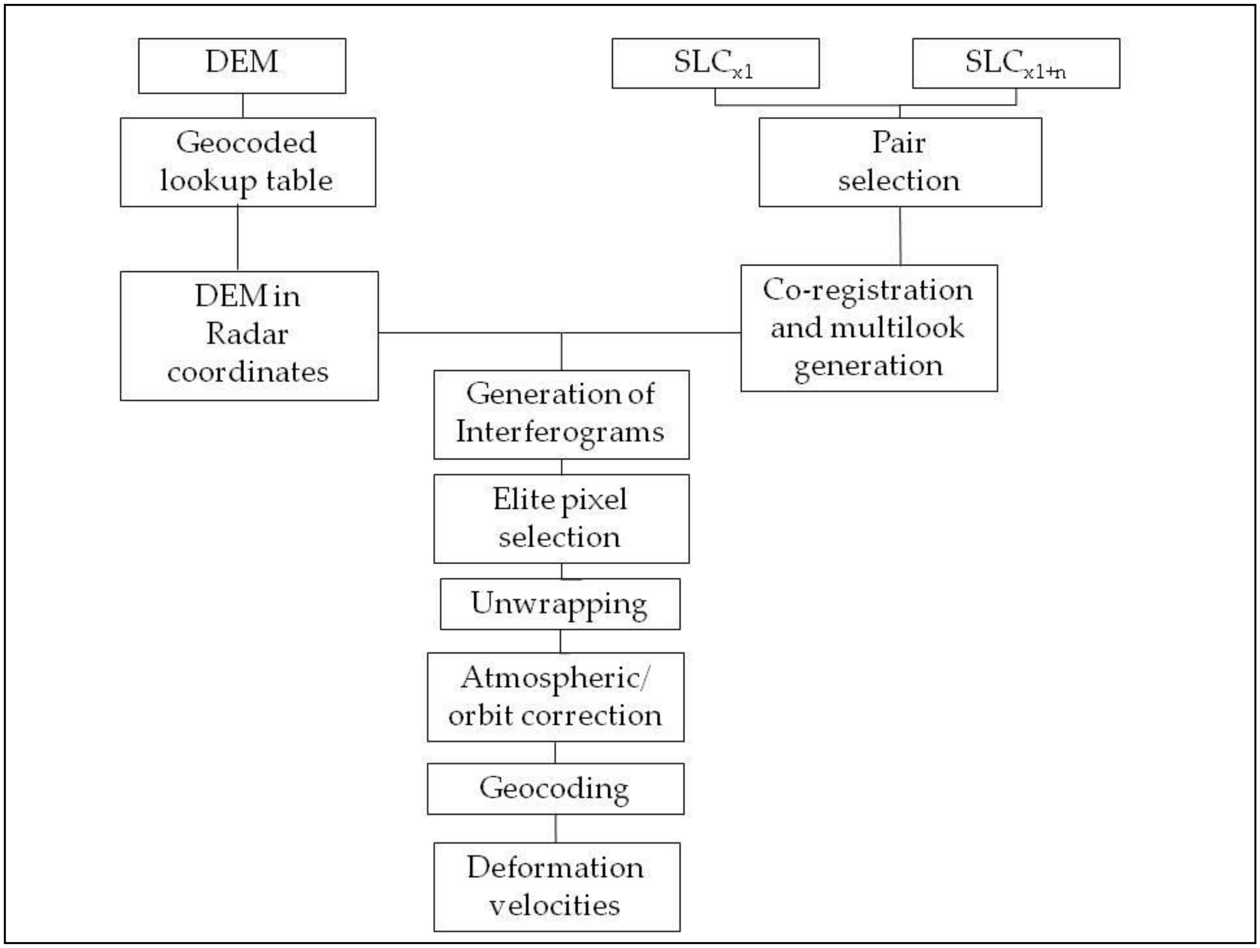

Figure 5. Flow diagram of interferometric processing of InSAR data (modified from Li et al., 2018).

Uncertainties in VLM rate estimates arise from the backscatter signal being affected by soil structure and moisture (Morrison et al., 2011; Morrison et al., 2012), resulting in apparent ground deformation values that may reach 0.5 radians (Molan and Lu, 2020). Considering this value as the maximum uncertainty level, an annual uncertainty of ±0.2 cm/yr and ±0.7 cm/yr is expected for Sentinel-1A/B and ALOS, respectively. Adding to soil variability, the amount of radar wave penetration in areas with vegetation coverage depends on the structure and density of the canopy and the radar wavelengths; accordingly, wavelengths less than 10 cm (C-band, e.g., Sentinel-1A/B) mostly sense the upper portions of vegetation whilst wavelengths longer than 20 cm (L-band, e.g., ALOS) penetrate deeper into the canopy and can interact with the ground (Hensley et al., 2001), yielding higher coherence values than C-band data (Shirzaei et al., 2021). Consequently, ALOS has proven to be more effective in reaching scatters below sparse vegetation (Luo et al., 2014; Tosi et al., 2016).

Last, the deformation values obtained using SAR data were compared and validated with the velocity values from two permanent GNNS stations located in Barranquilla (11.0197°/–74.8496°) and Santa Marta (11.2253°/–74.1870°). Despite these stations being situated outside the study area, the satellite frames covered their locations, rendering them helpful to establish whether the trends found using these two approaches were alike (see Figure 4 for the location of GNSS stations).

2.3 Results

2.3.1 Coastline Changes

The average annual horizontal coastline change rates for 2010–2020 ranged from over −25 to +15 m/yr (Figure 6). Erosion rates increased alongshore in the same direction as the littoral drift (east–west). The only exceptions to the predominant erosive regime occurred on the westernmost segment of the study area where accretion rates larger than +10 m/yr were identified. Localized accretion was also observed on the east side of the mouth of the CGSM and next to two groins built west of the coastal town of Ciénaga in the early 2010s (see white and green colors in Figure 6).

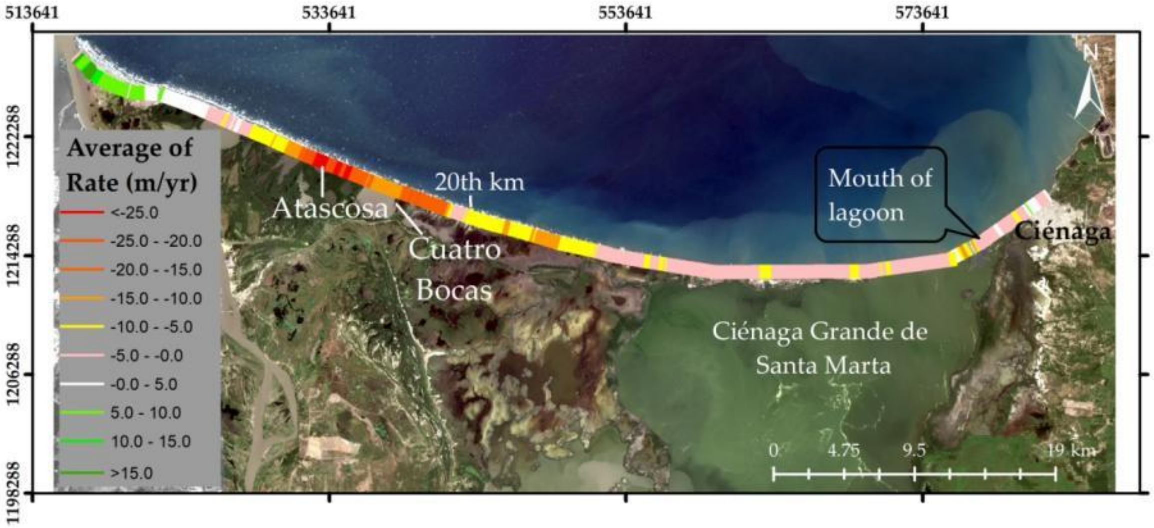

Figure 6. Coastline changes (m/yr) as derived from DSAS for the period 2010–2020.

From the mouth of the CGSM to the 20th km, erosion ranged between −1 and −10 m/yr (see pink and yellow transects in Figure 6). This erosion peaked along the stretch between the 20th km and La Atascosa lagoon (orange and red transects in Figure 6) and reached local average values up to −25 m/yr. Erosion rates progressively decreased westward from this lagoon and changed to accretion west of the El Torno lagoon (see green colors in Figure 6), where a levee, built at the mouth of the Magdalena River, hampers the westerly movement of sediment. The most significant erosion rate values for 2010–2020 occurred seaward of La Atascosa lagoon. Upon inspection of the imagery, it was observed that this largest average erosion rate was produced from the migration of an inlet after a breach of the lagoon in 2016.

2.3.2 Vertical Land Motion (VLM) and Line of Sight (LOS) Velocities

For both ALOS and Sentinel-1A/B data, vegetation coverage and the high dynamics of the coastline resulted in areas below the coherence threshold of 0.65 established in this work. Thus, there is a lack of information westward of Cuatro Bocas lagoon, where wetlands and vegetation are widespread (Figures 6 and 7). However, bare and sparsely vegetated terrain along the barrier island, particularly in the eastern and central areas where salt plains, stabilized dunes, and paleo-beaches are typical, provides a continuous strip of sufficient return signal, achieving the coherence threshold.

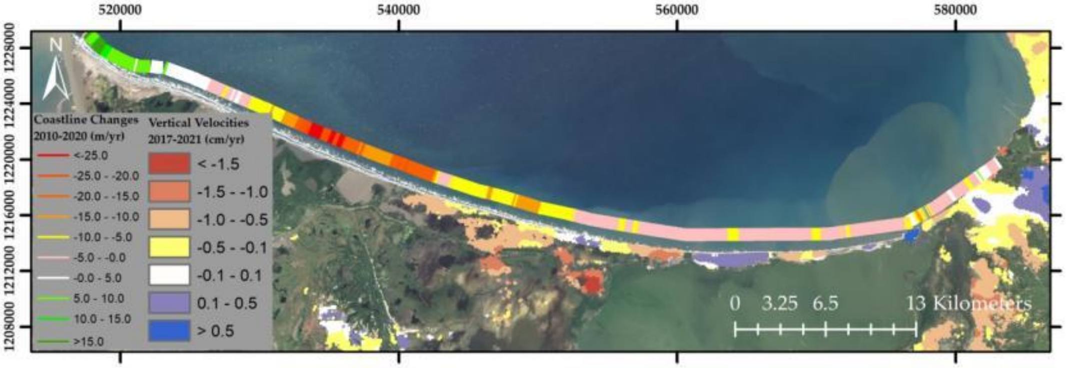

Figure 7. VLM rates for 2017–2021 as derived from Sentinel 1A/B data and coastline

changes for 2010–2020 displayed with an arbitrary offset from the actual coastline for presentation purposes. Positive velocities (white and cold colors) represent stable areas and displacements toward the satellite, while negative velocities (warm colors) indicate displacement away from the satellite.

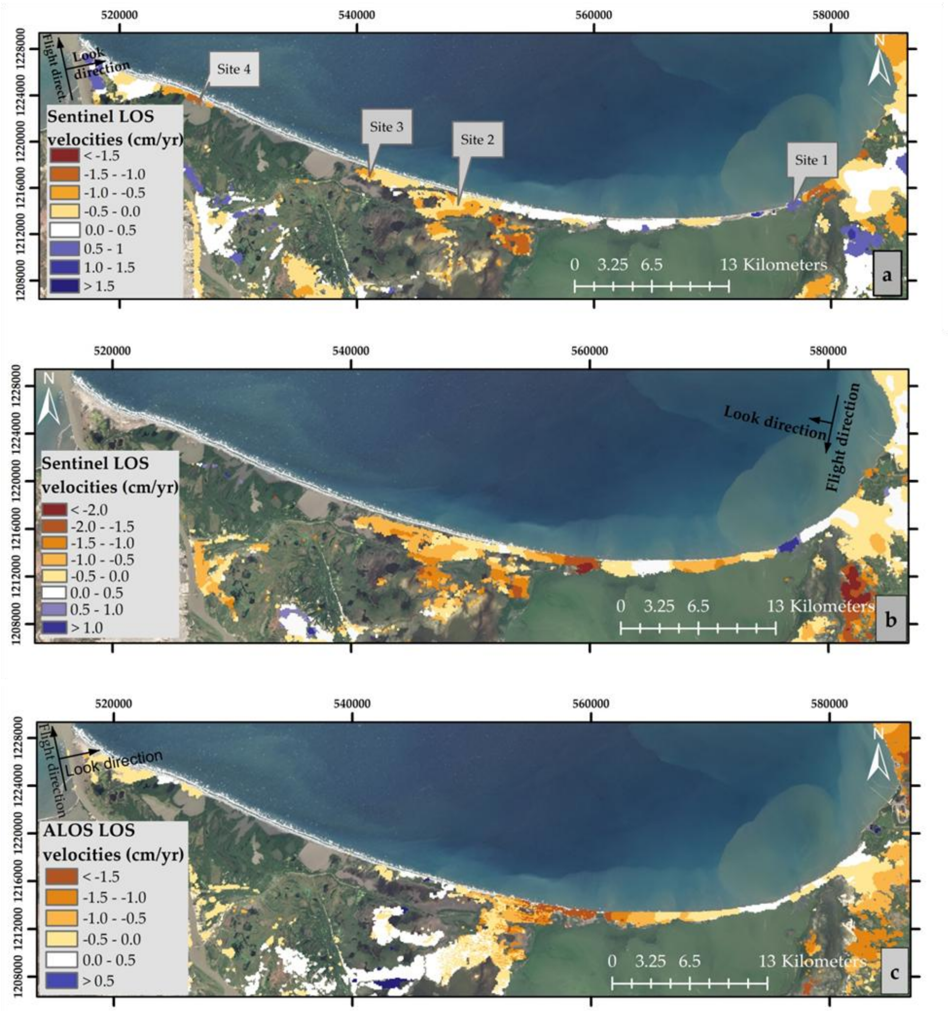

Figure 8. LOS velocities for (a) Sentinel-1A ascending track for 2017–2021; (b) Sentinel-1B descending track for 2017–2021, and (c) ALOS ascending track for 2007–2011. Positive velocities (white and cold colors) represent stable areas and displacements toward the satellite, while negative velocities (warm colors) indicate displacements away from the satellite. The location of the four time series described below is shown in (a).

VLM velocities, calculated by combining the LOS velocity vectors of Sentinel-1A (i.e., ascending track) and Sentinel-1B (i.e., descending track) are shown in Figure 7.

Appendix 1 shows the same results of Figure 7 after aggregating the data in 1.5 and 5 km sections. In the coastal town of Ciénaga and northeast from this location, it is observed that VLM velocities are larger than −0.5 cm/yr, and decrease (i.e., become more negative) around the CGSM. West of Ciénaga and seaward from the CGSM, the signal is patchy. Subsidence rates are the largest westward from the location known as Kangarú (see Figure 4b for location), reaching values of up to −1.0 cm/yr along the stretch of coast between Kangarú and Cuatro Bocas lagoon, a sector characterized by erosion rates larger than 5 m/yr (see yellow and orange transects in Figure 7). In contrast, velocities larger than +0.5 cm/yr were observed west of the CGSM mouth (see dark blue in Figure 7).

LOS velocities from Sentinel-1A and B show the same trend as the overall VLM (Figure 7) along the deltaic barrier island, suggesting that the vertical component of land displacement dominates over the horizontal component at this incident angle (Figure 8a,b). LOS velocities related to scatterers in the coastal town of Ciénaga were around zero for all three tracks illustrated in Figure 8, and became smaller (i.e., subsidence increased), southward from the town, towards the eastern margin of the CGSM. Westward from the town Ciénaga, specifically in the stretch of coast between the mouth of the CGSM to Kangarú (see Figure 4b for locations), LOS velocities of Sentinel-1A showed a zone ranging from 0 to +0.5 cm/yr (white colors in Figure 8a), whereas both ALOS and Sentinel-1B indicated LOS velocities ranging between −0.5 and

−1.5 cm/yr (see orange and brown colors in Figure 7b,c). Westward of Kangarú (close to site 2 in Figure 8a), the LOS velocities of ALOS, Sentinel-1A, and Sentinel-1B revealed negative values along the coastline and around the wetlands.

The standard deviation (S.D.) of the LOS velocities, illustrated in Figure 9, indicates that the smallest spread of the LOS velocities, given by the standard deviation values closer to zero, is found for the Sentinel-1B data (Figure 9b). For all tracks, the smallest standard deviation values occur in the town of Ciénaga (Figure 9), reflecting higher coherence values in urban settings. In the undeveloped areas, the largest S.D. values occur on the CGSM shores (see red colors in Figure 9), where the most negative LOS velocities within the study site occur (Figures 7 and 8). In general, it is observed that extreme LOS velocities, either positive or negative, coincide with high S.D. values (red colors in Figure 9).

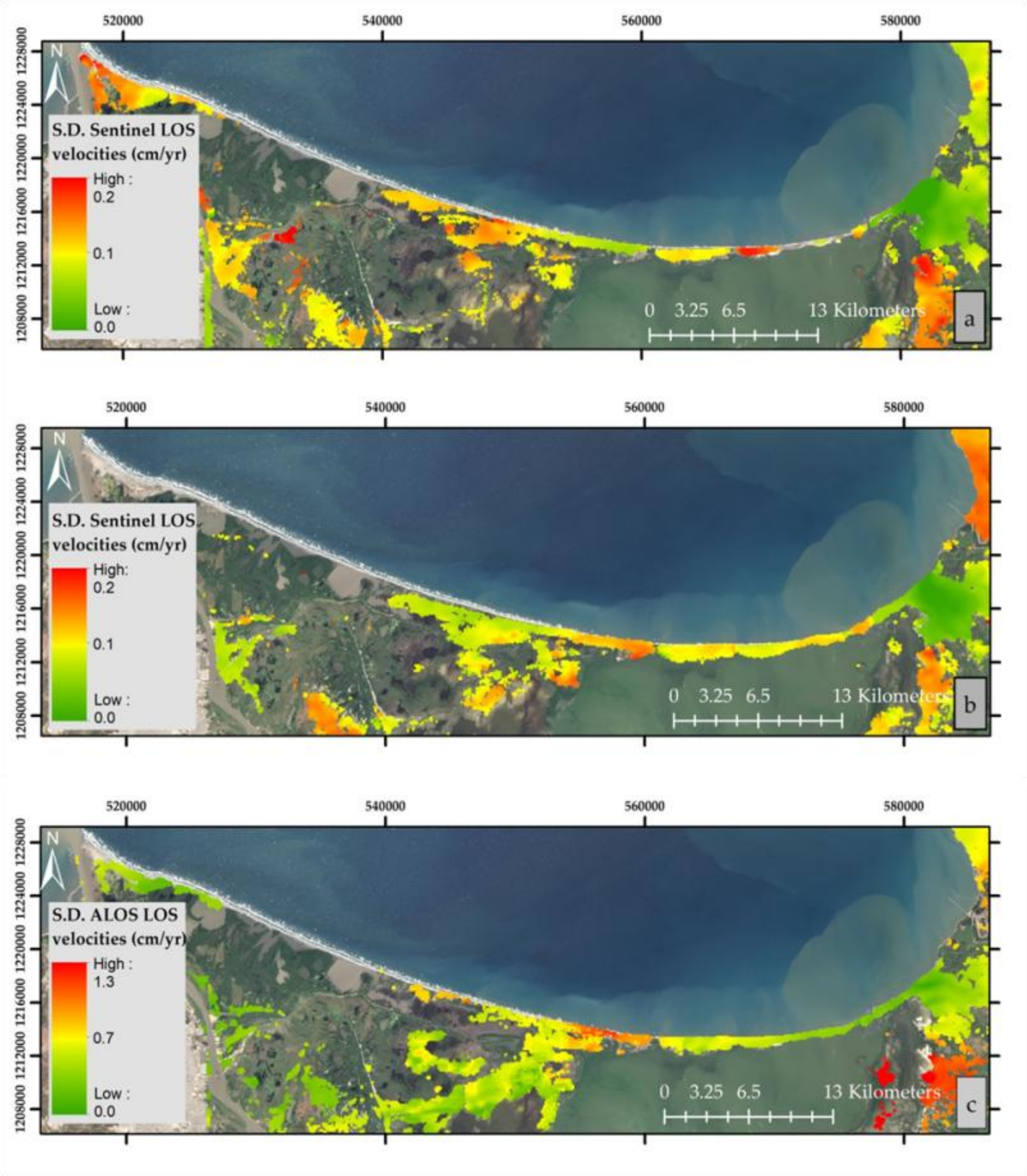

Figure 9. Standard deviation (S.D.) for each pixel of the estimated LOS velocities for (a) Sentinel-1A ascending track for 2017–2021; (b) Sentinel-1B descending track for 2017–2021, and (c) ALOS ascending track for 2007–2011. Red/green colors indicate high/low variability in the LOS velocities over time.

2.3.3 LOS Displacement Time Series

To inspect the trends of the land displacement over time, the LOS displacement time series of four sites are depicted in Figures 10–13, whose locations are shown in Figure 8a. Figure 10 shows the LOS displacements for site 1 and exemplifies the anthropogenic impact on VLM (Figures 8a and 10). In this sector, to face coastal erosion on the western side of the mouth of the CGSM, two groins were built in 2012. These coastal structures produced a gain of sediment on the updrift side of the groins, reflected by a slope value of 0.9 cm/yr for the best fitting line to the associated time series.

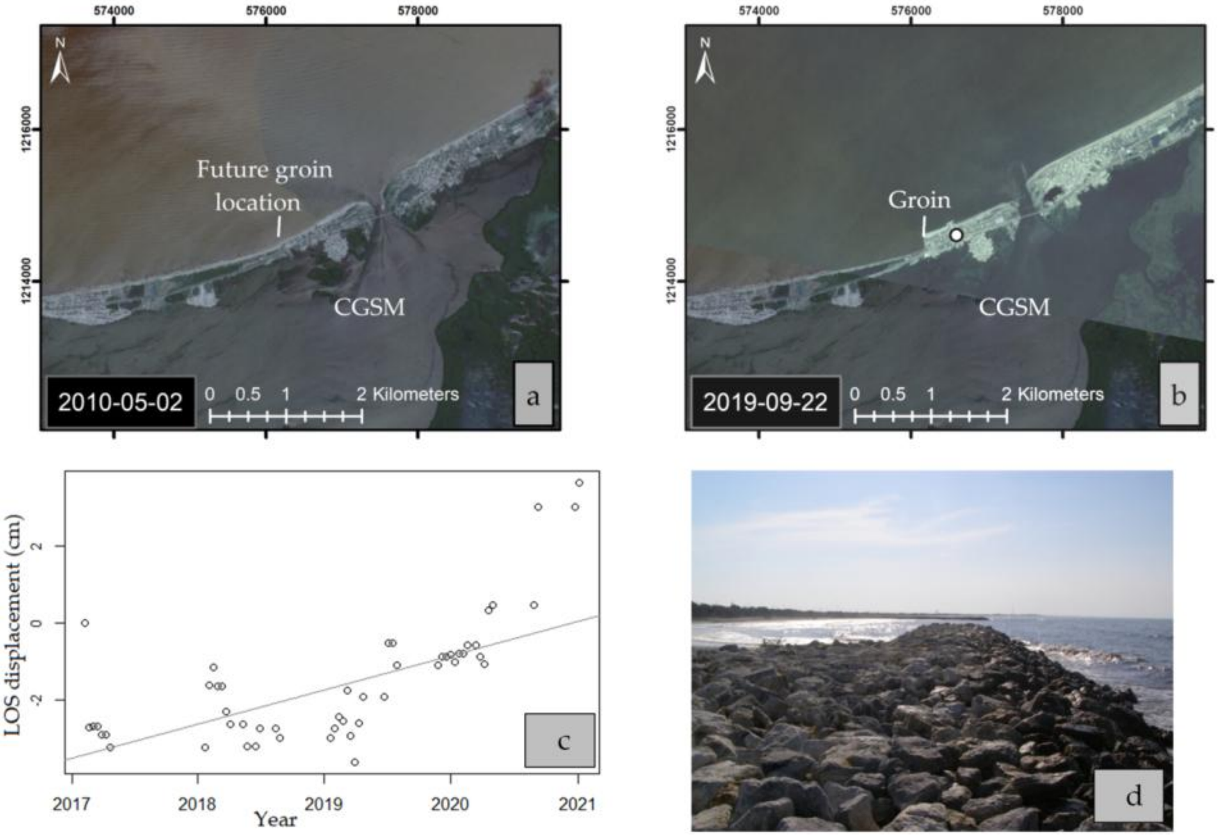

Figure 10. Satellite images before (a) and after (b) the groins were installed. Location of time series is indicated by white dot; (**c**) LOS displacement time series from Sentinel-1A for 2017–2021 (line represents the best fitting line with a slope of 0.9 cm/yr), and (d) photograph of the groins taken in 2014. Source of imagery: GeoEye images provided by Planet Labs Inc.

Figures 11 and 12 illustrate the time series of an area that was densely vegetated with mangroves until the 1980s (site 2 and 3, Figure 8a). This sector became the location of frequent overwashes that left behind sandy deposits, buried vegetation, and vegetated dunes scarped by erosive processes (Gómez et al., 2016) (Figure 11c). Typical time series show gradual downward displacement with slopes of approximately −0.5 cm/yr (Figures 11b and 12b).

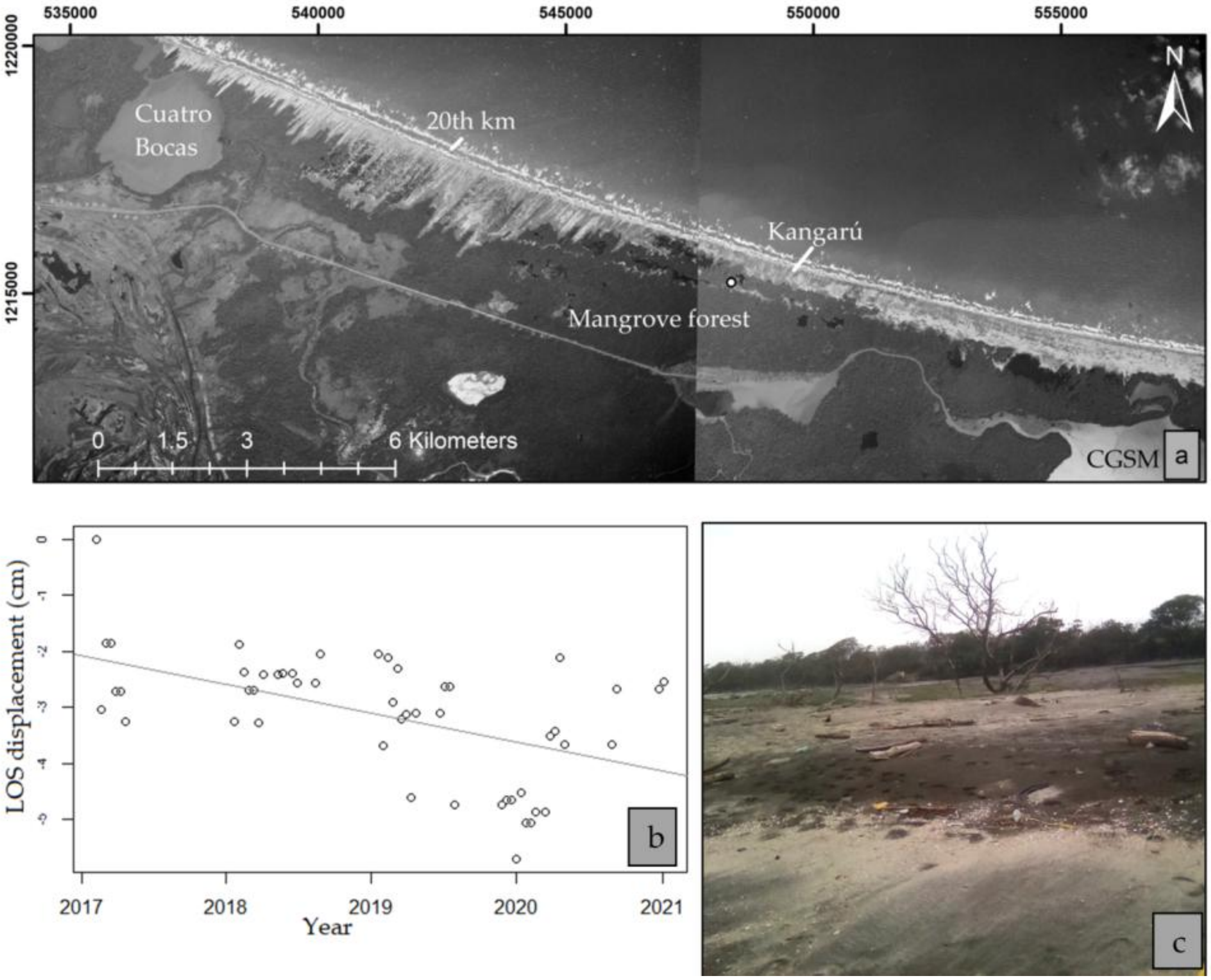

Figure 11. (a) Aerial photograph taken in 1953 showing the former mangrove forest before the highway was built. Parabolic dunes are seen in the backshore. Location of time series is indicated by white dot; (b) LOS displacement time series from Sentinel-1A for 2017–2021 (line represents the best fitting line with a slope of −0.52 cm/yr), and (c) shows standing dead trees on a former wetland.

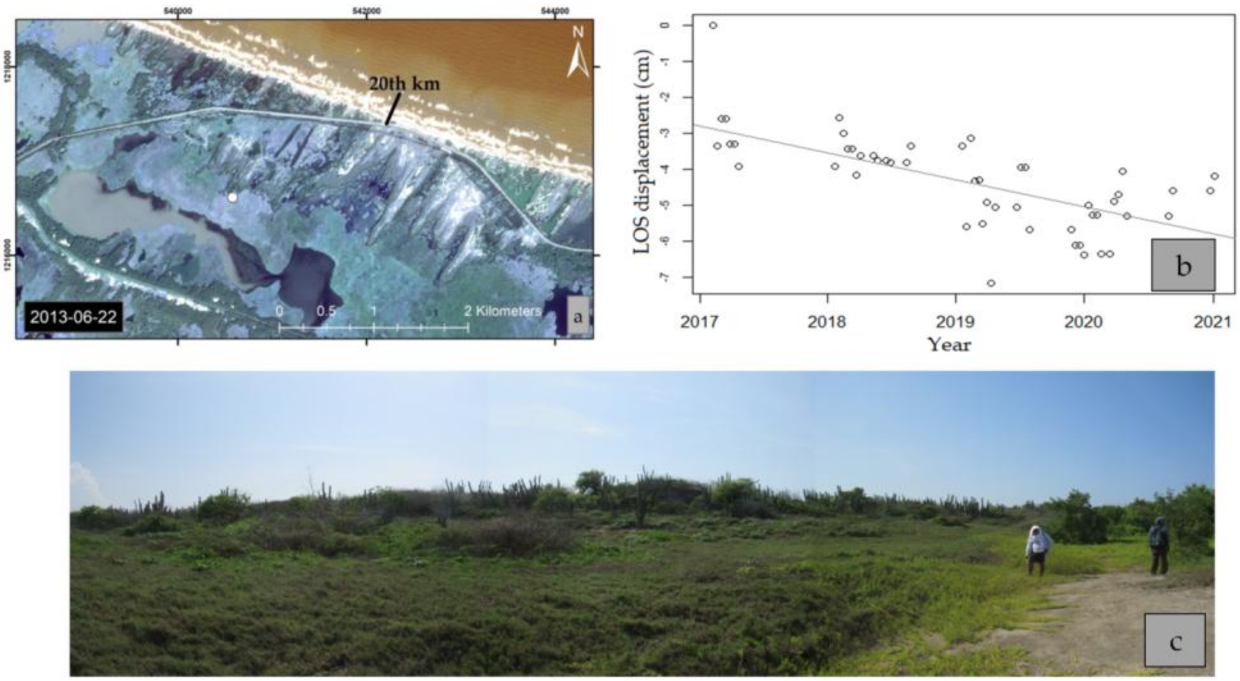

Figure 12. (a) Area affected by coastal erosion seaward of the highway as observed in 2013. Location of time series is indicated by white dot; (b) LOS displacement time series from Sentinel-1A for 2017–2021 (line represents the best fitting line with a slope of −0.71cm/yr), and (c) photograph of the dunes landward from the 20th km. Source of imagery: Digital Globe provided GeoEye image.

The westernmost time-series transect was located seaward from El Torno lagoon (site 4, Figure 8a). Although the shorefront in this area is erosive, no breachings have been observed in this lagoon during the last decade, and limited overwash deposits appear on satellite imagery. The area between the lagoon and the coastline consists of beach sands and embryo dunes sparsely covered with pioneer vegetation. LOS velocities for this site revealed a negative slope of −1.2 cm/yr for the linear fitting regression (Figure 13).

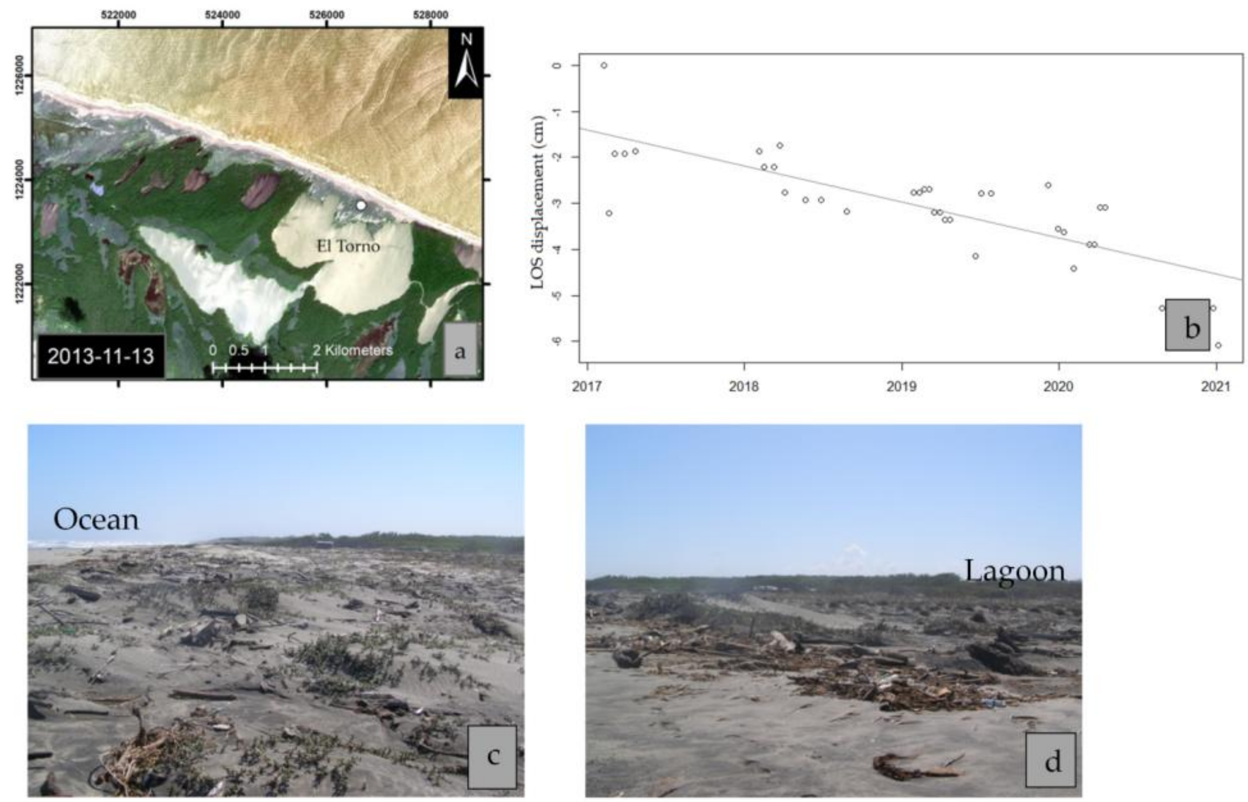

Figure 13. (a) El Torno lagoon showing stabilized washover in 2013. Location of time series is indicated by white dot; (b) LOS displacement time series from Sentinel-1A for 2017–2021 (line represents the best fitting line with a slope of −1.2 cm/yr); (c) photograph of the beach seaward, and (d) next to the north shore of the lagoon. Source of imagery: Digital Globe provided GeoEye image.

2.3.4 Comparison of VLM and LOS Velocities and GNSS Data

The trends in vertical land movement measured at the GNSS stations located in Santa Marta and Barranquilla were contrasted with VLM and LOS velocity values from InSAR pixels located nearby these stations. Every four years, daily readings for each station were processed by the Deutsches Geodätisches Forschungsinstitut (DGFI) to provide long-term displacements for a network of permanent stations in South America. Roughly matching the time span for ALOS data, a solution for 2006–2011 compiled for the GNSS station in Santa Marta (Figure 4a), indicated a vertical displacement of −0.52 cm/yr for that period (Sánchez and Seitz, 2011). For the same area, LOS velocities of −0.12 cm/yr were found for ALOS data. For the GNSS station in Barranquilla (Figure 4a), vertical displacements of −0.14 cm/yr were reported for 2007–2009 (Sánchez and Seitz, 2011), whereas a value of −0.31 cm/yr was obtained for the ALOS LOS velocities for 2007–2011. Sentinel data are not available for these years. For the period 2017–2021, VLM estimates using Sentinel-1A/B data near the Santa Marta station are −1.31 cm/yr. An updated processed solution for the GNSS stations to contrast the above values is not available yet.

2.4 Discussion

2.4.1 Subsidence in Deltas

Dating of modern deltas reveals that many major deltas worldwide were formed during the Holocene between 8,500 and 6,500 years before the present. The Fraser (Canada), Mississippi (United States), and Nile (Egypt) River deltas, to cite a few, were all formed within that period (Stanley and Warne, 1994). Accordingly, it has been suggested that following the initial rapid SLR during deglaciation, Holocene deltaic sequences began to accumulate as the rate of fluvial sediment input exceeded the declining rate of SLR in continental margins (Stanley and Warne, 1994). Compaction of the strata deposited during the Holocene has been described as a major driver of natural land subsidence in these dynamic environments (Törnqvist et al., 2008; Teatini et al., 2011). In the case of the Magdalena River, we argue that downward trends in vertical land motion (VLM) reflect ongoing subsidence associated with modern fluvio-lacustrine sediments (Hernández and Maldonado, 1999; Colmenares et al., 2007) that overlie relict sediments from a former delta that migrated westward after the mid-Holocene (Romero-Otero et al., 2015). Low magnitude seismological activity associated with the SMBF indicates that VLM estimates reported in this work (Figure 7), at least during the period of observation (2007–2021), are not earthquake-driven, which suggests that one of the primary drivers of this process is sediment compaction of organic and mud deposits.

VLM in the study site is closely related to the Holocene history of the Magdalena delta and the supply of sediment from the drainage basin. Natural drainage displacements and levee constructions since the 1920s (von Erffa, 1973) have progressively diminished the amount of sediment delivered by the Magdalena River to the study area (von Erffa, 1973), disrupting the balance between sedimentation and natural compaction of sediments. More recently, the construction of the highway between Barranquilla and Santa Marta in the 1950s hampered the interchange of water between lagoons and ocean (Elster et al, 1999), indirectly causing subsidence by disturbing the mangrove forest.

Compared to previous assessments of RSL change for the region, which indicate current rising sea levels of approximately 0.5 cm/yr (Andrade et al., 2013), local subsidence values of up to −1.5 cm/yr highlight the relevance of incorporating subsidence in the prediction of SLR and coastline positions. Earlier work aiming to correlate coastline erosion to sea-level rise, as measured from historical tide gauges, revealed that the average coastline change is two orders of magnitude greater than the rate of the sea-level rise (Leatherman et al., 2000). Thus, by increasing the rate of local RSL, subsidence might increase future flooding risk associated with storms (Luo et al., 2014; Mazzotti et al., 2009), resulting in the possible drowning of the deltaic barrier island.

2.4.2 Linking VLM and Coastal Erosion

The coastline changes and VLM findings are contrasting. Whereas erosion processes underlie most of the study area, the signal of VLM is highly variable along the study area. In other words, not all areas with annual shoreline erosion rates larger than the uncertainty threshold (i.e., ±5.0 m/yr) were associated with local subsidence. This indicates that subsidence is a factor that can exacerbate the impact of ongoing erosive processes. We explored the influence of scale by examining aggregations of the data at 1.5- and 5-km scales (Appendix 1). At all scales considered, the sector with high coastline erosion rates of around −10 m/yr coincided spatially with subsidence rates of up to −1.0 cm/yr (i.e., stretch between Kangarú and Cuatro Bocas in Figure 7). Regions that exhibited coastal erosion within the range of uncertainty (± 5m/yr, e.g., seaward from the CGSM) showed a variable VLM signal at all scales. A similar interplay is described for a stretch of coast comprised of marshes and mud in the Mekong Delta in Vietnam, where secular coastal erosion values larger than −50 m/yr are paired with subsidence rates exceeding −1.5 cm/yr (Anthony et al., 2015). Similarly, high coastal erosion trends in an abandoned lobe of the Yellow River delta in China were associated with average subsidence rates of −0.7 cm/yr and up to −2.1 cm/yr for the period 1992–2000 (Polcari et al., 2018). These observations highlight the regional variability and complexity of drivers behind the coastal change that demand weighing the different drivers of change even within one deltaic system.

In addition to the natural compaction caused by sediment overloading, the site-specific subsidence rates observed along the stretch of coast between Kangarú and Cuatro Bocas might be triggered by the effect of localized dehydration and mortality of mangrove forest (Figure 3), following the highway construction in the early 1950s (Elster et al., 1999). In this sector, as the mangrove decayed after the highway construction, soil salinity has hampered the establishment of vegetation (Elster et al., 1999), giving place to barren or sparsely vegetated swales (see Figure 11c). Yuill et al. (2009) report that a large component of subsidence in organic-rich soils (e.g., peats associated with mangroves) is due to the exposure of soils to atmospheric oxygen, which reduces soil volumes by converting organic carbon into carbon dioxide gas (Figure 3). In coastal Louisiana, at least 60% of subsidence takes place within the uppermost 5–10 m, where wood peat is widespread (Törnqvist et al., 2008). Subsidence in the former mangrove forest within the study area (Figures 11 and 12) may therefore be higher with this additional factor at play and is at its root caused by the anthropogenic alteration of the wetland. Other factors causing site-specific variability in subsidence rates are related to the uneven distribution of compressible sediments, hydraulic properties in aquifer systems, and groundwater extractions from aquifer systems (Lu et al., 2014; Tosi et al., 2016). In the Mississippi delta, the variability of the underlying Holocene lithology modulates compaction rates and their spatial variability (Törnqvist et al., 2008). Such factors may explain the variability in VLM and LOS velocity observations east of Kangarú (Figure 7). A lack of detailed knowledge of the Holocene stratigraphic sequence at this site hinders establishing any current relationship between subsidence rates and underlying substrates, but surficial geological cartography, developed by the Colombian Geological Survey (Hernández and Maldonado, 1999), indicates that subsidence takes place in alluvial and fluvial-lacustrine sediments that make up a floodplain landform (Gómez et al., 2016).

A rise in relative sea level as a product of either subsidence or an increase of GMSL creates more space for sediments to accumulate (i.e., accommodation space) (Catuneanu, 2006), which is an underlying condition for transgression to occur. In other words, for any given interval of time, accommodation space is created by a rise in sea level and/or subsidence. Thus, where rates of accommodation space are larger than sediment deposition, there is a landward shift in sedimentary environments, an expansion of the subtidal zone (Catuneanu, 2006), and a landward displacement of the barrier (van Heteren, 2014). Although stratigraphic evidence of a transgressive succession was not gathered in this work, previous mapping of chronic erosion in conjunction with frequent overwashes between Kangarú and Cuatro Bocas (Gómez et al., 2016) indicate that transgression might occur along this stretch of coast. Transgression was identified by two processes acting in tandem on the landscape: (i) storm overwash deposition resulting in temporal accretion of sediments landward of the contemporaneous shoreline, followed by (ii) a period of more gradual erosion interrupted by a new overwash cycle. Thus, we suggest that subsidence velocities of up to −1 cm/yr in the observed stretch of coast are a factor that underpins transgression of the coastline and the occurrence of overwashes, resulting in a landscape composed of scarped dunes and eroding beaches overlain by washover fans and surrounded by overwash channels. The spatial variability of VLM and LOS velocities east of Kangarú (see Figure 7) refrain us from extending the hypothesis of a transgressive shift of the coastline to the stretch of coast seaward from the CGSM.

2.4.3 Utility and Limitations of InSAR for Interpretations of Coastal Landscape Change.

Within the study area, the analyses of four specific sites show the potential of InSAR as a tool to help explain local changes to the landscape. Although somewhat expected, coastline accretion and the upward movement of the terrain on the updrift side of a pair of groins built in 2012 (Figure 10 and site 1 in Figure 8a) stresses the reliability of the technique and its effectiveness in detecting VLM. It also illustrates that VLM estimates may include upward VLM related to crustal motion and the effect of sediment deposition and surface accretion. In a similar manner, in addition to subsidence, the finding of LOS velocities smaller than −1.0 cm/yr seaward of El Torno lagoon and near the coastline (Figure 13 and site 4 in Figure 8a), might be influenced by the erosive regime of the coastline. Indeed, Shirzaei et al. (2021) indicate that, in dynamic landscapes, VLM estimates do include changes in surface elevation due to erosion or deposition and must be separated from other types of VLM. Thus, in addition to the locations mentioned above, areas next to sand beaches, such as the coastal town of Ciénaga and the westernmost extreme of the study site, the VLM velocities might be influenced by the removal or deposition of sand associated with erosion or accretion.

In contrast to the aforementioned locations, the locations of the time series for sites 2 and 3 are over 1 km landward from the coastline (see Figures 8a, 11 and 12), in sectors that were populated by abundant mangrove forest until the 1980s. Therefore, this area is prone to gas emission related to the oxidation of organic-rich soils. VLM along these locations ranges between −0.5 and −1 cm/yr (Figures 7, 11b and 12b). As the sites selected for the time-series profiles are not in close vicinity to the coastline, their velocity values are not influenced by the erosive regime of the coastline and can be considered to reflect subsidence only. Deltaic areas with similar subsidence rates to the values reported above have been described elsewhere (Di Paola et al., 2018; Polcari et al., 2018; Zhang et al., 2015).

Caveats of the InSAR methodology in this study also arise in vegetated areas when the surface backscattering properties due to growing vegetation change through time (Pepe and Calò, 2017). This factor is especially the case for wavelengths of less than 10 cm (e.g., Sentinel-1 A/B C-band) that interact with leaves and soft-stemmed vegetation. The constantly changing vegetation conditions result in temporal decorrelation and a reduction of the coherence level (Oliver-Cabrera and Wdowinski, 2016; Pepe and Calò, 2017). This issue was addressed by contrasting the outcomes of Sentinel-1A/B with ALOS, a satellite with a longer wavelength (L-band), which penetrates deeper in the canopy or ground surface (Hensley et al., 2001). When comparing LOS velocities for Sentinel-1A/B and ALOS ascending orbit, we found that, even though the latter provided absolute larger subsidence values, the trends for both platforms were aligned for most of the study area (Figure 8).

Given the caveats mentioned above, the absolute values of VLM should be interpreted with caution in the context of an application demanding high accuracy levels. However, despite the lack of temporal overlap between the Sentinel-1A/B and ALOS datasets, the outcomes of ALOS and Sentinel-1A/B were consistent in revealing areas prone to upward and downward movements with respect to a reference point in Ciénaga.

2.5 Conclusions

This study combined satellite images and InSAR data to examine the interplay of vertical land motion (VLM) (2007–2021) and coastline changes (2010–2020) along a deltaic barrier in the Colombian Caribbean. The findings are as follows:

- Annual coastal erosion rates increase in the same direction as the littoral drift (i.e., East-West direction), reaching a peak of −25 m/yr next to a lagoon known as Cuatro Bocas. In contrast, VLM patterns are highly variable along the study site, precluding linking coastal erosion rates to negative VLM values in general.
- VLM in the study area is linked to the Holocene History of the Magdalena River delta and the supply of sediment from the drainage basin. Anthropogenic alterations are known to have caused alteration in sediment supply, which is not sufficient to counterbalance sediment compaction.
- Although subsidence alone does not explain the high rates of coastal erosion along the study area, it is a factor that enhances erosive processes and is linked to the occurrence of overwashes and breaching of lagoons. The zones with the highest subsidence (up to −1.5 cm/yr) are areas surrounding the Ciénaga Grande de Santa Marta composed of marshes and mud. These local subsidence values are at least two times larger than gauge-measured rates of SLR.

- Local subsidence rates of up to −1 cm/yr were found in an area where mangrove forest was abundant before a highway was built in the 1950s. The likely primary drivers of subsidence in this sector are sediment compaction of the Holocene alluvium and gas emission followed by oxidation from organic-rich soils.
- Using InSAR close to the coastline is complex due to the ever-changing condition of the littoral, particularly in vegetated and highly dynamic coastlines. In those areas of the study site next (within ~100 m) to the coastline, the velocities obtained by combining Sentinel-1A/B interferograms might reflect the added effect of VLM of land surface change due to sediment accretion/erosion.

There is a lack of research that jointly discusses coastal dynamics and VLM at a local scale to date. Thus, this work provides a baseline to be used as a blueprint to track coastal dynamics and future ground motions once longer records of radar data become available. In addition to contributing to the explanation of the chronic erosion of the study area, the outcomes of this project are relevant for engineers of a proposed expansion to the current highway.

Chapter 3. Examining the hydro-climatic drivers of lagoon breaching and healing in a deltaic barrier

Chapter published on April, 15 2023 as:

Gómez, J.F., Kwoll, E., Walker, I.J., Orejarena, A.F., 2023. Examining the Hydro-Climatic Drivers of Lagoon Breaching and Healing in a Deltaic Barrier. Geosciences 13, 118. https://doi.org/10.3390/geosciences13040118

Abstract

As sea-level rise (SLR) and human-made interventions affect coastal currents and sediment transport, coastal barriers have become more vulnerable to the effect of storms, hurricanes, and climate variability. The response of each barrier is unique and depends on wave regime, coastline orientation, weather conditions, bathymetry, and type of human-made interventions, among other factors. In the Magdalena River deltaic barrier, located on the Colombian Caribbean coast, coastal erosion has caused the loss of hundreds of square kilometers of critical ecosystems, such as wetlands and lagoons, since the 1960s. This work aims to analyze the short-term drivers behind the observed loss of lagoons, particularly the drivers of lagoon breaching events and subsequent healing along the deltaic barrier. Lagoon breaching events and healings were detected using satellite imagery, and the timing of these events was related to prior local atmospheric, oceanographic, and fluvial conditions. The findings reveal that the dynamics of the lagoons are driven by extreme river discharges and energetic wave conditions associated with storms or hurricanes. Healing is driven by the sediment supplied by littoral currents and average waves punctuated by energetic events. The cumulative effect of breaching and healing has resulted in a deltaic barrier that has rolled over the lagoons, reducing their size over time. These findings provide a better understanding of the forces of coastal retreat and will help inform future management decisions of the coastal zone.

Keywords: inlets; washouts; overwash; storms; cold fronts; lagoon; breaching events; Magdalena River; Colombian Caribbean; erosion; deltaic barrier.

3.1 Introduction

Coastal barriers and their associated beach and dune systems are dynamic, unconsolidated sedimentary systems that respond to multiple forcers over various temporal scales, from episodic short-term events (e.g., wave energy and water level changes during storms) to longer-term processes (e.g., sea-level changes, storm pattern changes) (Cooper et al., 2018). These shore parallel landforms offer mainland protection against extreme events, and lagoons and wetlands, components of the back-barrier, are often highly productive ecologically (Davidson-Arnott, 2010; Sherwood et al., 2023). Understanding the response of coastal barriers to drivers of change is key to explaining past behavior and forecasting potential paths of barrier evolution and the ecosystems that inhabit it.

Coastal barriers respond to changes in forcing processes by modifying their morphology and/or material composition (Cooper et al., 2018). The response of a coastal barrier to hydroclimatic disturbances is modulated by the frequency and intensity of the driver and the barrier geomorphology (Thieler and Young, 1991; Sallenger, 2000; Houser et al., 2007). Particularly, the presence and relative location of foredunes and secondary dunes play a critical role in the response of a barrier to storms (Durán et al., 2016; Ashton and Lorenzo-Trueba, 2018). In the mid-term (decades to centuries), the fate of barrier islands—a type of coastal barrier—depends on their capacity to build upwards and landward to cope with SLR (Ashton and Lorenzo-Trueba, 2018).

On barrier islands, two of the mechanisms that trigger their migration are overwashes and deposition of sand in flood-tidal deltas as a result of inlet formation (Leatherman, 1979; Cowell et al., 2003; Donnelly et al., 2006). These processes are caused by short-term events (e.g., storms), and their extent is generally less than 1 km^2 (Hudock et al., 2014). Overwashes are wave-driven processes that trigger the flow of water and sediment over the beach berm or dune crest with no direct return to the ocean (Donnelly et al., 2006). Inlet breachings refer to overwash events that, by generating a tidal inlet, open a temporal connection between the ocean and back-barrier landforms, such as lagoons, bays, marshes, and tidal creeks (FitzGerald, 1996; FitzGerlad et al., 2008). Inlet breachings and overwashes that are driven by oceanographic processes are both commonly caused by run-up above the highest cross-shore point of the beach profile due to a combination of tidal water level, barometric pressure variations, and the incoming wave field (Sallenger, 2000; Donnelly, 2006); thus, both processes are considered genetically related (Leatherman, 1979) with overwashes generally taking place at lower storm thresholds than inlet breachings (Zăinescu, et al., 2019). Due to this higher storm threshold and because the inlet remains open for periods of time ranging from months to years, cross-shore sediment transport tends to be larger during inlet breachings than during overwashes (Zăinescu, et al., 2019).

A second mechanism for inlet breaching coined washout, results from floodwaters flowing from the lagoon to the ocean (Sherwood et al., 2023). Washouts occur when raised water levels in the back-barrier lagoon cause a hydraulic gradient and flow over the barrier in a seaward direction. Therefore, various mechanisms, acting either at the landward or seaward side of a coastal barrier to producing high run-up or raised lagoon water levels, might be responsible for breaching events. These mechanisms include onshore-offshore winds (Morton and Sallenger, 2003; Pierce, 1970), storm-related waves (El-Ashry and Wanless, 1965; Aubrey and Speer, 1984; Hapke et al., 2013; Miselis et al., 2016), ocean-to-estuary hydrostatic head differences (Sherwood et al., 2023, Miselis et al., 2016), and fluvial streamflows (Rich and Keller, 2013). While overwash and inlet breaching (regardless of the mechanism) have been recognized as the main drivers of coastal barrier and lagoon morphodynamics elsewhere (Cooper et al., 2018,Sherwood et al., 2023; Leatherman, 1979; Zăinescu et al., 2019), the response of a landscape to these processes is not universal but site-specific (Cooper et al., 2018), and their overall role in the long-term evolution of the barrier is poorly understood. The onshore displacement of sediment transfer resulting from the aforementioned mechanisms is fundamental to maintaining natural barrier resilience to rising sea levels and preventing the barrier from drowning (Aagaard and Kroon, 2019).

Whether a coastal barrier recovers to its previous state following a disturbance or is altered permanently depends on characteristics such as barrier width, dune height, and distance to the mainland (Kombiadou et al, 2019). In the specific case of barrier breachings, recovery (i.e., healing time) varies according to local geomorphology and the interaction of waves, currents, and sediment supply (Cooper et al., 2018). It has been recognized that the height reduction in a barrier due to events such as storms increases vulnerability to new disturbances, which may prolong healing times if the storms are clustered in a short period of time (Ferreira et al., 2022; Houser and Hamilton, 2009). Based on a study case in the Danube Delta (Black Sea), Zăinescu et al. (2019) described a three-stage conceptual model of breach-healing following an oceanographic disturbance. Accordingly, the landward deposit near inlet openings may stabilize due to the establishment of pioneering vegetation and cause the shrinking of the lagoons (Zăinescu, et al., 2019). For river-driven events, outwash deposits may provide a new sediment input to the coastline and a temporal outward building of the barrier.

Here we examine the lagoon breaching and healing processes of a deltaic barrier in the Colombian Caribbean. Using satellite imagery and 50 years of data on hydro-climatic variables, including wave and wind characteristics, river discharge, precipitation, and sea level pressure, we investigate (i) the drivers of lagoon breaching, (ii) conditions for lagoon healing, and (iii) the long term evolution of barrier width and lagoon shape. Determining the drivers of lagoon breaching and healing will provide insight into the process of coastal change and assist decision-making for the proper coastal management of retreating coastlines in the study site and other similar coastal barrier environments.

3.1.1 Regional Setting

The barrier and back-barrier lagoons that are the focus of this work are situated in a National Park on the Colombian Caribbean coast. The lagoons are located behind a narrow (1–800 m wide) sandy barrier surrounded by wetlands. From east to west, they are named Cuatro Bocas, Atascosa, Las Piedras, and El Torno (Figure 14).

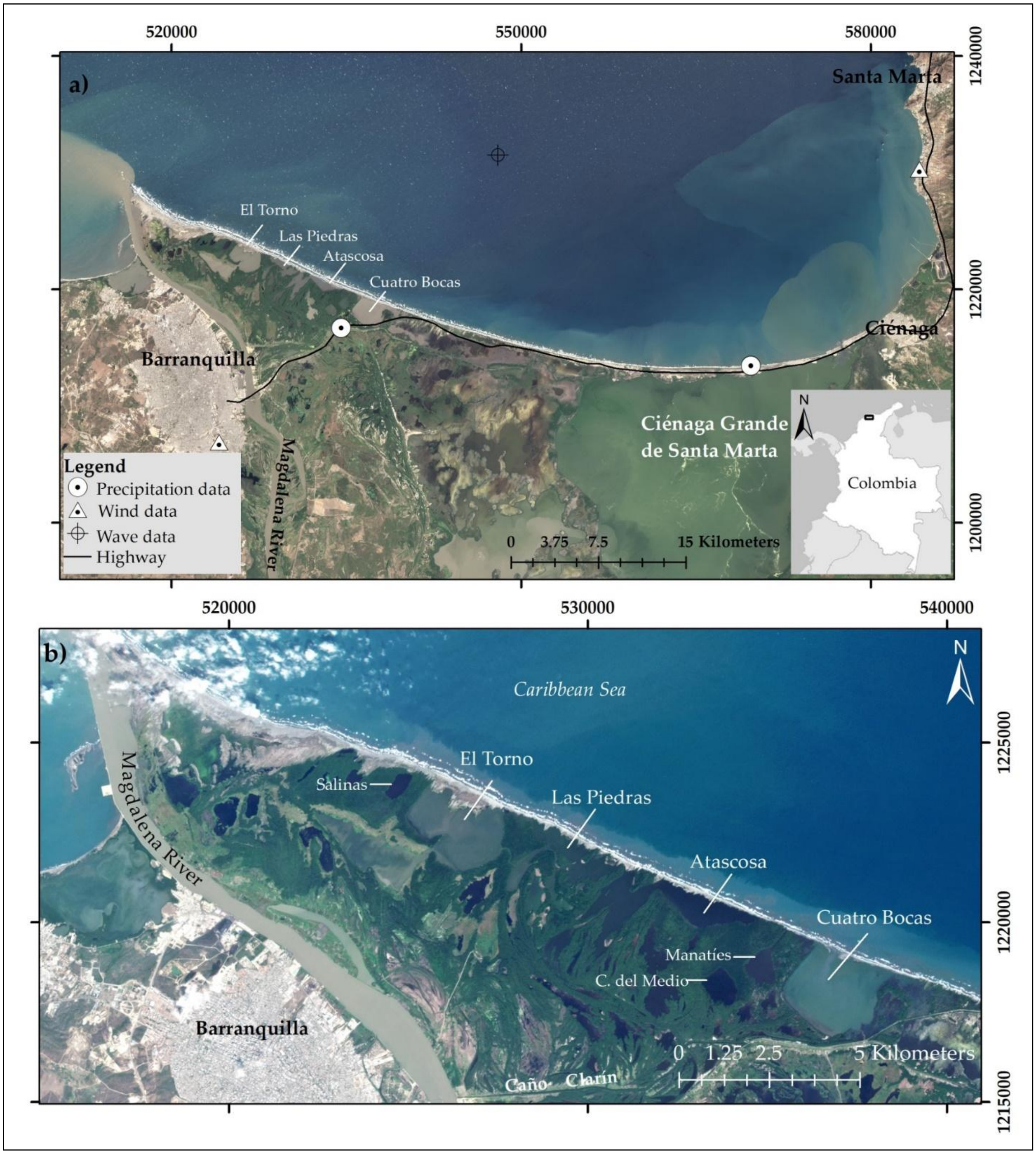

Figure 14. Map of the Magdalena River delta and its marginal lagoons on the northeast coast of Colombia. (a) The coastline between the cities of Santa Marta and Barranquilla and the measuring stations are shown. (b) Zoom of lagoons that are the focus of this work, including from east to west: Cuatro Bocas, Atascosa, Las Piedras, and El Torno lagoons.

The Magdalena River, the largest fluvial system in Colombia, is connected to these lagoons via a network of natural channels. The mouth of the river is situated in a mixed-diurnal microtidal regime characterized by tides ranging between 0.13 and 0.40 m (Ospino et al., 2018). The small tidal ranges in the Caribbean Sea, at times, might be entirely masked by coupled meteorological and wave conditions (Kjerfve, 1981). No engineering structures have been made to control the freshwater flux out of the lagoons, but the flow is occasionally enhanced by dredging activities in one of the channels exiting the Cuatro Bocas lagoon; the most recent dredging operations were done in 2017 and 2020 (L. García, personal communication, March 2022). Prior to the 1900s, this channel (known as Caño Clarín Viejo) was a natural navigational waterway used as a trade route (von Erffa, 1973), but after the 1920s, the ongoing engineering of the river mouth has produced a transition along the barrier from fluvial to marine-dominated conditions (Gómez et al., 2016).

The hydro-climatology of the study area is influenced by the migration of the Intertropical Convergence Zone (ITCZ). The ITCZ defines a region where the trade winds of the Northern and Southern hemispheres converge, generating a low-pressure belt around the Equator that oscillates seasonally (Poveda, 2004). The weather in the Colombian Caribbean is controlled by the shift in the position of the ITCZ, resulting in a bimodal regime with two dry seasons (December–March and June–July) and two wet seasons (April–May, and August–November) (Poveda, 2004). Precipitation and river discharge can have substantial interannual variability (Restrepo et al., 2000) as a result of the influence of the cold (La Niña) or warm (El Niño) phases of the El Niño Southern Oscillation (ENSO). Specifically, there is a positive correlation between La Niña years and larger-than-average discharge values in the Magdalena River (Poveda, 2004) For instance, whereas the average discharge is around 7200 m^3/s (Restrepo et al., 2000, Hastenrath, 1990), an extreme water discharge of 16,463 m^3/s was reported during the La Niña event of 2010 (Ospino et al., 2018). In contrast to the river discharge, the Caribbean trade winds are weakened during the La Niña years (Hastenrath, 1990). Aligned with the Caribbean trade wind system, northeasterly waves are predominant in the Colombian Caribbean, reaching their maximum significant wave heights between December–March and June–July (Appendini et al., 2015). Extreme wave conditions in the Colombian Caribbean are caused by either cold fronts or hurricanes (Ortiz-Royero et al., 2013; Otero et al., 2016; Bernal et al., 2016). Cold fronts are usually accompanied by heavy rains, gusty winds, and thunderstorms (Hsu et al., 1988). By increasing the atmospheric pressure gradient in the Caribbean Sea, cold fronts temporally increase wind speeds and wave heights in low-pressure areas along the front. In the Colombian Caribbean, cold fronts usually occur between December and May and peak in February (Ortiz-Royero et al., 2013). Hurricanes, on the other hand, occur between June and November and follow a northwesterly path that usually hinders landfalls on the Continental Caribbean coast. Nonetheless, although uncommon, those hurricanes whose trajectory is in close proximity to the continental shore create the necessary fetch to produce energetic sea states that influence the morphodynamics of the Colombian Caribbean coast. For example, hurricanes Joan (October 1988), Lenny (November 1999) (Bernal et al., 2016; Cueto et al., 2022), Matthew (September–October 2016) (Ortiz-Royero et al., 2013; Ortiz-Royero et al., 2021), and Iota (November 2020) (Ortiz-Royero et al., 2013) created impactful forces on the Colombian Caribbean coast.

The volumes of long-shore sediment transport have not been quantified in the area, but the accumulation of sediment on the east side of groins built next to the Ciénaga Grande de Santa Marta mouth (Figure 14) indicates a predominant westward sediment transport (Gómez et al., 2016; Gómez et al., 2021). Prior studies have revealed that the shoreline in the study site has been retreating at least since the early 1960s (von Erffa, 1973; Gómez et al., 2016). Peak values of coastal erosion have been reported along the stretch of coastline between the Cuatro Bocas and the La Atascosa lagoons (von Erffa, 1973; Gómez et al., 2021), where most of the former parabolic dunes have been eroded (Figure 15). Local subsidence values of up to 1 cm/yr are considered a mid-term driver of coastal retreat (Gómez et al., 2021). An exception to the erosive trend takes place at the downdrift end of the littoral cell, along the stretch between the Magdalena River mouth and west of the El Torno lagoon (Gómez et al., 2016).

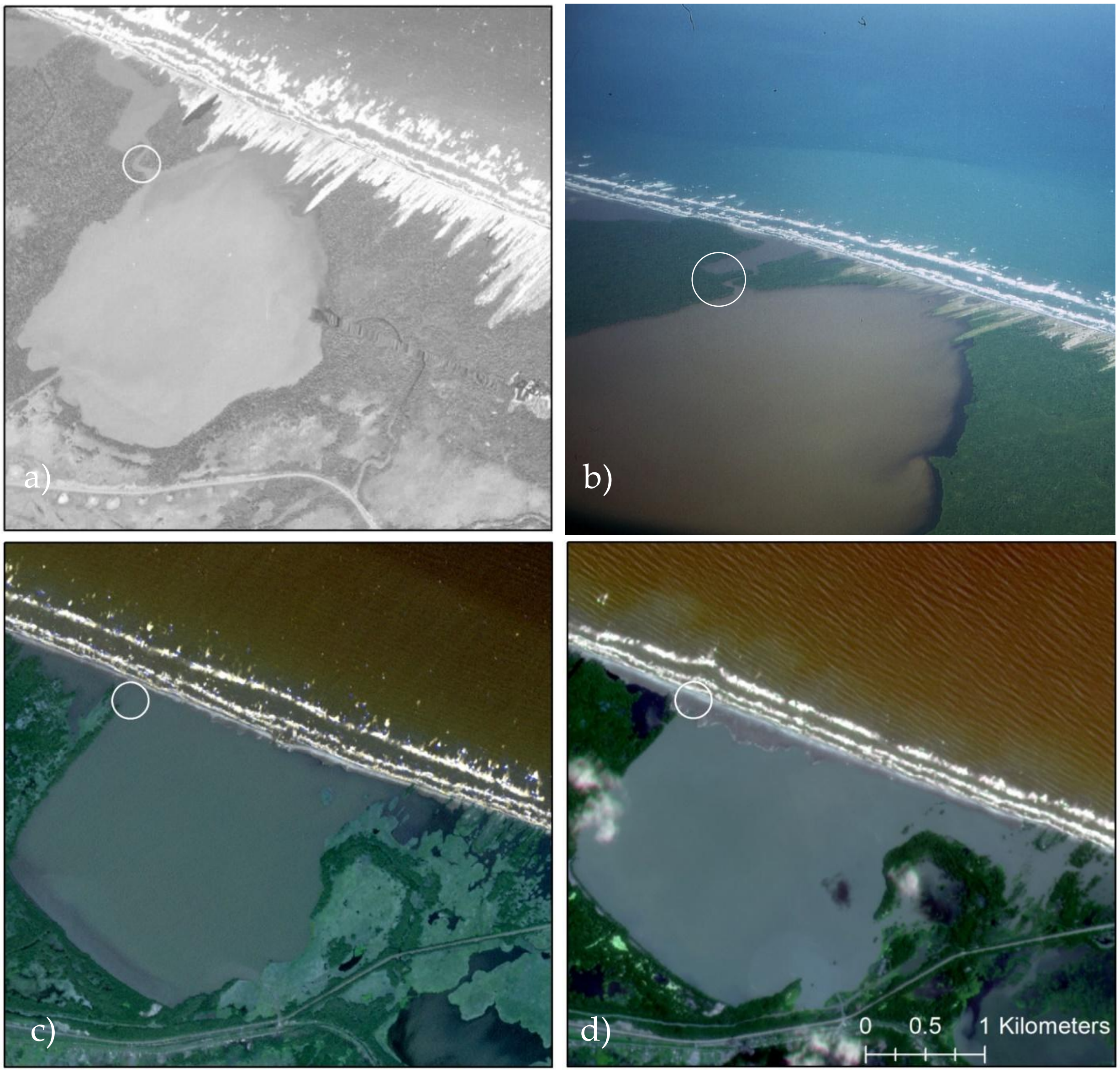

Figure 15. Evolution of Cuatro Bocas lagoon as shown in (a) aerial photograph from 1954, (b) oblique aerial photograph from 1971, (c) Geoeye satellite image taken in 2011, and (d) Geoeye satellite image taken in 2020. The circle indicates the same location on each image. Geoeye imagery courtesy of Planet Labs.

3.2 METHODOLOGY

3.2.1 Hydro-climatic data

Time series of wave conditions, wind velocity and direction, precipitation, and river discharge were compiled in a database for the period 1973–2020 to examine their influence on lagoon breaching and healing. Hourly measurements of wind speed (WS) and direction (WD), precipitation (P), and river discharge (Q) were obtained from meteorological and flow gauging stations managed by the Colombian Institute of Hydrology, Meteorology and Environmental Studies (IDEAM). The location of the wind and precipitation gauges is shown in Figure 13; the river gauge, not shown in Figure 13, is located 109 km upstream of the Magdalena River mouth. No significant tributaries exist between this station and the Magdalena River mouth. Sea-level Pressure (SLP) was examined for the Caribbean Sea using the NCEP/NCAR reanalysis model provided by the National Oceanic and Atmospheric Administration (NOAA; https://psl.noaa.gov, accessed on 16 July 2022).

Modeled, gridded wave conditions for the Caribbean Sea based on wind data (Orejarena-Rendón et al., 2022) obtained from the Japanese 55-year reanalysis (JRA-55) were gathered from an open-source database (https/ttps://digital.csic.es/handle/10261/241150, accessed on 6 October 2022) for the period 1973–2017. The same method used by Orejarena-Rondón et al. (2022) was followed to obtain wave conditions for the period 2018–2020. From the wave-gridded data, time series of maximum daily significant wave height (H_s) and corresponding period (T_m) and wave direction were extracted for a virtual buoy offshore of the study site (location shown in Figure 13). Full details of the wave model simulation are given in Orejarena-Rondón et al. (2022).

In order to account for the combined effect of significant wave height and period, the maximum daily wave energy flux was subsequently retrieved using the equation:

$$WEF = \frac{1}{64\pi}\ \rho g^2 TmHs^2 \qquad (2)$$

Where *WEF* is the wave energy flux per unit of wave-crest length (kW/m) (hereafter wave energy), ϱ is ocean water density (1023.6 kg/m^3), and g is acceleration by gravity.

3.2.2 Coastal and Lagoon Changes, Breaching Events, and Recovery Period

Changes in lagoon size as well as the timing and extent of inlet breachings and duration of healings were tracked using satellite imagery for the period 1973–2020. The high periodicity of Landsat images (every 16 days) resulted in this dataset being the main source of information to track breaching and healing processes. In total, a dataset consisting of >100 Landsat 1, 4, 5, 7, and 8 scenes, spanning the years 1973 to 2020, was examined. When Landsat data were not available (e.g., between 1991–1995), temporal gaps were covered using other satellite platforms such as Ikonos (N = 5), SPOT (N = 4), or aerial photographs provided by the Colombian Survey Institute (IGAC) (N = 12). In addition, Planet Scope (N = 43) and RapidEye (N = 75) imagery, made available through the Planet Explorer platform (https://www.planet.com/explorer, accessed on 26 December 2022), supported the analysis of lagoon dynamics since December 2009. The imagery dataset was built with the aim of reducing the time span between consecutive images. Because of the combination of imagery from different platforms, pixel resolution differs in the dataset from as much as 60 m for the earliest Landsat images to 3 m for the most recent Planet Scope data.

The shape of the lagoons along the land-water limit was digitized manually, and changes in size and shape over time were assessed using STAMP, an ArcGIS-based tool (Robertson et al., 2007) for spatial and temporal analysis of moving polygons. By carrying out a visual inspection of the imagery dataset, the timing of inlet breaches and the duration of healings were noted for the study period. Inlet breaching events were visually identified by the first appearance of a tidal inlet along the barrier. The end of a healing period was visually identified as the first image in which the barrier was connected again. A detailed analysis of inlet breachings was done for events where the availability of imagery enabled narrowing down the timing of the breaching event to within a period of fewer than three weeks. In other words, there is an overlaying assumption that inlet breaching is an episodic event that occurs prior to the detection of the inlet. In contrast, the healing of a lagoon was not considered episodic but rather a continuous process that can last months or even years.

Barrier width and coastline changes were quantified using a script for ArcGIS (Digital Shoreline Analysis System (DSAS)) (Thieler et al., 2003) that allowed measuring the distance between the coastline and the seaward limit of the lagoons in 1973 and

2020. The barrier width for stretches of coast without lagoons was traced following the limit of the wetlands. Coastline changes were quantified using the Average Rate of Change (AOR) parameter of DSAS (Thieler et al., 2003) for Landsat images taken on 2 January 1973, 2 September 1984, 26 June 2000, 20 May 2011, and 16 August 2020. The coastlines were manually traced along the wet-dry sand limit, which given the small tide range in the study area, provides a consistent measure of the Mean High Water Line (MHWL) (Dolan et al., 1980; Moore, 2000; Dean and Dalrymple, 2004).

3.2.3 Driver Analysis

Following Bailey et al. (2021) and Rao and Liu (2017), we contrasted variations between event and non-event (background) hydro-climatic conditions to quantify the influence of the potential parameters on breaching and healing processes. Specifically, the potential role that wind and precipitation (representing local atmospheric conditions), sea-level pressure and wave energy (representing large-scale oceanographic drivers), and river discharge (representing fluvial input to the study area) play in the breaching or healing of any of the lagoons was analyzed by comparing average and event conditions for these variables. This exploratory analysis aimed to establish any causal relationship between episodic meteorological forces and their effect on the landscape.

Monthly non-event (background) conditions were established by calculating the median, 25th, and 75th percentile values of the data for each of the variables mentioned above. Similarly, event conditions were determined by calculating the median, 25th and 75th percentile for each variable prior to an event. Specifically, the percentiles for event conditions were calculated considering a five-day period within the 3 weeks prior to the first appearance of a breach in the imagery: the day with the peak values for each variable and two days before and after this peak value took place.

The difference between event and non-event (background) medians (DBM) was then expressed as a percentage of overall visual spread (OVS), where OVS is the range from the lowest to highest interquartile (25th and 75th quartiles). Assessing DBM as a percentage of OVS renders a quantification of distribution offset between event and non-event conditions for each of the hypothesized forcers (Bailey et al., 2021) of lagoon breaching. Thus, large absolute values resulting from the DBM/OVS ratio (e.g., >20%) are indicative of conditions that are unlike average conditions for a particular month. The DBM/OVS ratios for the event and average conditions are contrasted using boxplots in conjunction with time series subsets of the parameters prior to specific events.

SLP variability for the Caribbean Sea preceding breaching events was analyzed based on daily reanalysis data provided by NOAA. A cross-section indicating the gradient in SLP across the Caribbean Sea supported the examination of this variable in lagoon breachings. Specifically, the rate of change (i.e., slope) of SLP along a profile starting by the Puerto Rico trench (north of Puerto Rico) and extending in a southwesterly direction to the study site was calculated for the day with the steepest gradient before the event. To exemplify this approach, Figure 16 illustrates the section (A-A’) used to quantify the gradient as well as SLP conditions on 26 May 1988.

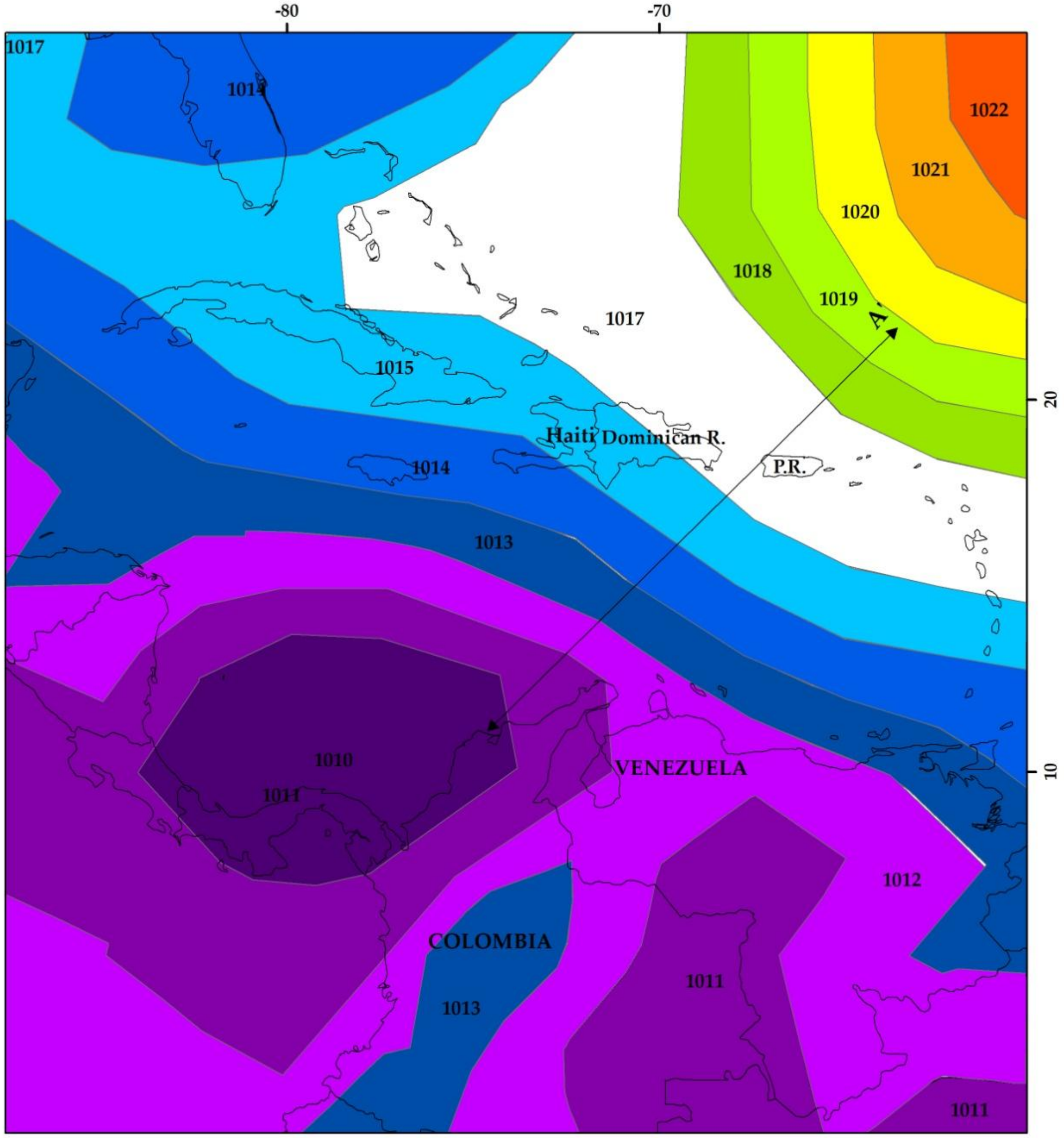

Figure 16. Sea level pressure (mb) composite mean for May 26, 1988. Section A-A’ was traced to capture the gradient in SLP before a breaching event took place. Note that Puerto Rico was abbreviated as P.R. (Source of SLP values on https://psl.noaa.gov, accessed on 16 July 2022).

3.3 Results

3.3.1 Hydro-Climatic Conditions

The non-event (background) hydro-climatic conditions at the study site, as characterized by the median of all data for each month during the period 1970–2020 are shown in Figure 17. Winds predominantly from the north and northeast are highest (>5 m/s) in December–April and reach a minimum in September–November (Figure 17a, b). In tandem with maximum wind velocities, maximum values of SLP and wave energy occur between January and March, and a second peak takes place in June–July (Figure 17c, d). Minimum SLP and wave energy occur in September–November, coinciding with low wind speeds. Precipitation is lowest between December–March (dry season) and peaks (>160 mm/month) during the wet season in September–November (Figure 17e). Discharge values, as measured 109 km upstream of the Magdalena River mouth, are high (>8000 m^3/s) in October–December and low in February–April following the dry season (Figure 17f). Figure 17g illustrates the Southern Oscillation Index (SOI) as retrieved from NOAA (https://www.cpc.ncep.noaa.gov/data/indices/soi, accessed on 24 May 2022). This index shows the timing of the ENSO circulation during the observation period with strong La Niña events (positive index) in 1971, 1975, 1989, 1996, 2000, 2009, 2011, 2018, and 2020.

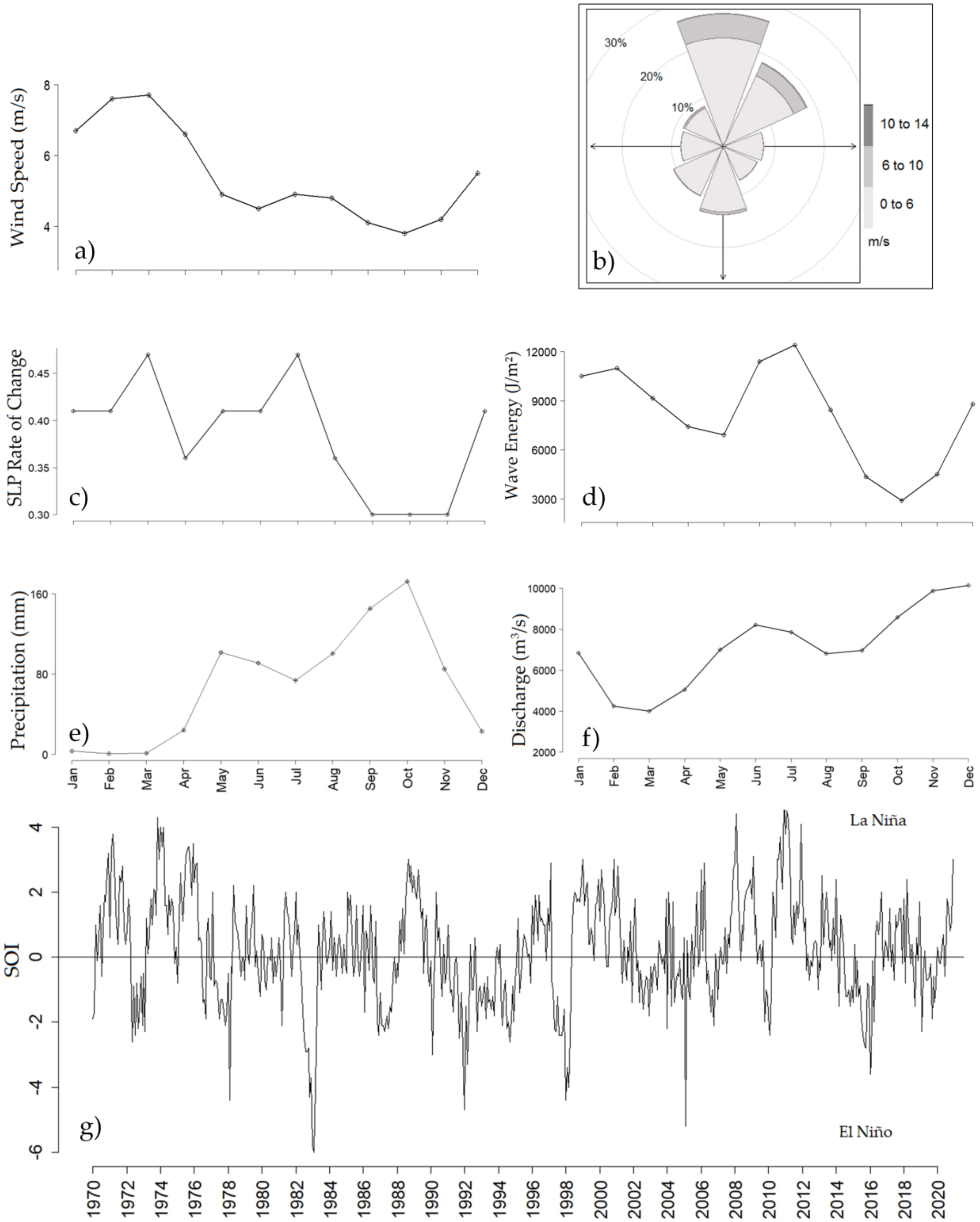

Figure 17. Monthly median, 25th and 75th percentiles of (a) wind speed, (Barranquilla), (b) wind direction (Barranquilla), (c) sea-level pressure, (d) wave energy (virtual buoy), (e) precipitation (Barranquilla), (f) Magdalena River discharge (Calamar) and (g) yearly ENSO oscillations based on the SOI index. Note: Monthly SLP rates of change were assessed for the A-A' profile shown in Figure 16.

3.3.2 Lagoon and Coastal Changes

Aerial extent and shape changes of four lagoons in the study area from 1973 to 2020 are illustrated in Figure 18. Forced by coastal retreat, the seaward limit of the lagoons has moved landward since 1973, resulting in a reduction in the areal extent of the water bodies of up to 2.00 km^2 (51.4%), 0.74 km^2 (30.5%), and 0.20 km^2 (6.0%) for the lagoons La Atascosa, Las Piedras, and El Torno, respectively (Figure 18 and Appendix 2).

Along the Cuatro Bocas lagoon, despite the landward retreat of the coastline, the water body has enlarged its area over time (by 2.3 km^2/49.6% with respect to 1973) through encroaching adjacent wetlands (Figure 18). In contrast, three small lagoons located at a distance away from the coast (i.e., Manatíes, Ciénaga del Medio, and Salinas) remained stable during the study period (Figures 14 and 18). Overall, a general reduction in the barrier width has taken place from 1973–2020. The barrier width between the Cuatro Bocas and the La Atascosa lagoons has remained narrow through time, ranging from 0.05 to 0.250 km (Figure 18d); the largest changes in the width occurred in areas that were occupied by mangrove forest (Figure 18a, b).

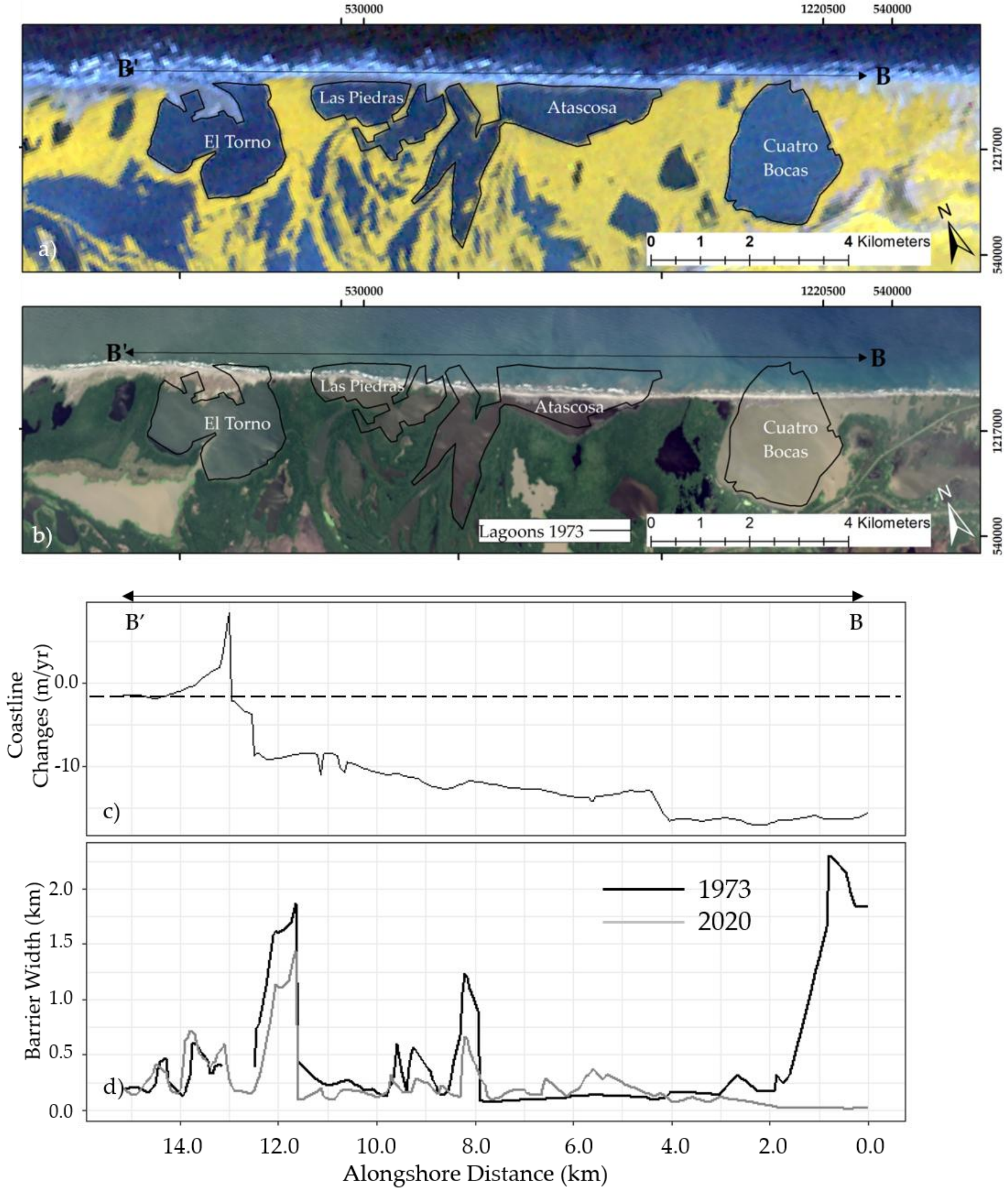

Figure 18. Barrier and lagoon evolution as observed on a) January 2 1973 and b) February 17 2020; c) average rate of coastline changes for 1973, 1984, 2000, 2011 and 2020 and d) barrier width for transect B-B′ in 1973 and 2020.

3.3.3 Lagoon Breaching

A total of 33 breachings were discovered during the study period (13 for Cuatro Bocas, 9 for Atascosa, and 10 for Las Piedras, and none for the El Torno) (Appendix 3). Out of these 33 breachings, 13 events could be narrowed down to a span of at least three weeks since the last time that a lagoon was observed closed (Table 2). Previous work observed that El Torno Lagoon breached in 1967 (von Erffa, 1973), prior to our study period. Since the date of breach can not be restrained, it is not included in the breachings listed here. A comprehensive list of all the breachings and healings detected in this work, including those events which were not possible to bracket within a period of at least three weeks, is provided in Appendix 3.

Table 2. First appearance of lagoon breaching detected for the period 1973–2020. Maximum daily value and DBM/OVS expressed in percent in the three weeks prior to the first appearance for hydro-climatic variables. Note: Bold fonts indicate the variable(s) that likely caused the breaching event.

Event No	Lagoon Breached	Date of Detection	Wave Energy (kW/m)	Wave Height (m)	Wind Speed (m/s)	River Discharge (m^3/s)	Precip. (mm)	Gradient of Atmospheric Pressure (%)
			DBM/OVS (%)	DBM/OVS (%)	DBM/OVS (%)	DBM/OVS (%)	DBM/OVS (%)	% difference with respect to average
1	Atascosa	1988/06/01	25,024	2.8	7.8	6,001	23	0.59
			55.6	**86.5**	**57.9**	-10.2	0	42.2
2	Piedras	2000/06/26	19,625	2.5	6.7	9,646	28	0.53
			12.7	24.0	2.9	**56.2**	0	28.0
3	Cuatro Bocas	2004/05/12	19,794	2.5	7.0	5,847	10	0.53
			58.5	**57.3**	4.2	33.4	0	28.0
4	Cuatro Bocas	2009/10/01	10,440	2.0	3.2	5,985	35	0.41
			67.7	**60.0**	-72.3	-32.7	0	38.5
5	Piedras/ Atascosa	2011/05/20	7,165	1.6	6.6	12,740	25	0.47
			-12.2	-4.3	**53.3**	**83.9**	0	13.5
6	Cuatro Bocas	2015/04/17	16,473	2.3	8.6	4,942	0	0.71
			68.9	**63.7**	5.3	-19.0	0	100.0
7	Cuatro Bocas	2015/07/30	36,051	3.2	6.3	4,957	15	0.57
			30.6	**36.2**	**63.6**	-246.0	0	43.9
8	Cuatro Bocas	2015/11/06	7,638	1.5	5.1	5,580	10	0.27
			58.9	35.6	38.8	-188.8	0	-6.9
9	Atascosa	2016/02/23	20,530	2.5	9.0	2,495	0	0.71
			46.8	22.4	12.5	-54.0	0	71.5
10	Cuatro Bocas	2016/06/11	14,414	2.1	4.5	6,334	10	0.47
			22.9	27.5	-54.2	-54.0	0	14.7
11	Atascosa	2016/10/15	76,185	4.4	6.3	7,362	10	0.53
			15.9	**28.6**	**68.9**	-50.6	20	79.1
12	Atascosa	2018/07/15	31,092	3.0	8.1	9,737	11	0.53
			48.0	**47.1**	**60.9**	**49.5**	0	12.1
13	Piedras	2020/09/10	6,072	1.6	3.2	9,025	15	0.35
			-34.7	-35.6	-67.8	**63.4**	0	18.2

Table 2 indicates the maximum daily values of hydro-climatic variables in the 3 weeks prior to the event together with the percentage of the ratio between DBM and OVS (see

Methods). Positive percentages are indicative of conditions above the background condition, negative values are indicative of conditions below the background condition.

Apart from events 2, 5, and 13, all breachings occur following a period of increased wave energy, seven of which follow an increase larger than 35% (see DBM/OVS ratios for events 1, 3, 4, 6, 8, 9, and 12 in Table 2). Not all high-energy wave events correspond to periods of larger-than-average local wind speeds. For example, events 3 and 6 have values close to average wind speeds (DBM/OVS < 10%; Table 2), and event 4 has a lower-than-average wind speed preceding the breach. Only event 5 was preceded by wind speeds 53% stronger-than-average but lower-than-average wave energy. Five events occurred during periods of higher-than-average discharge, and eight occurred during periods of lower-than-average river discharge. Those lower-than-average discharge events coincided with periods of high-energy wave events. Of the 13 events, only event 11 was preceded by higher-than-average precipitation (DBM/OVS of 20%; Table 2); all other events occurred following periods corresponding with average (background) values. Aside from event 8, all the events were preceded by larger-than-average sea level pressure gradients along the transect A-A′ (Figure 16).

From all the potential triggering mechanism of breachings considered in this work (regional wave energy and SLP, local wind forcing and precipitation, and river discharge), events appear to be either triggered by high regional wave fields or high river discharge, with local wind and precipitation playing no major role. The following subsections detail two events where high energy wave conditions were predominant (May 1988 and October 2016) and one event associated with high river discharge (May 2011).

3.3.4 High Wave Energy Breaching Event in May 1988 (Event 1)

High wave energy and northeasterly wind speeds of up to 12 m/s (55.6% and 42.1% DBM/OVS respectively; Table 1) preceded the breaching of the Atascosa lagoon in May 1988 (Figure 19). Maximum wave energy conditions occurred on May 25th (25,024 kW/m), and were followed by three days of above average wave energy levels. These conditions were associated with steep gradients in SLP between May 22 and 25, 1988, peaking in May 25 at values 42% higher than average values for May (see Figure 17c) Conversely, precipitation and river discharge values were average or below the average during May 1988 (0% and -10.2% DBM/OVS respectively, Table 2). Nevertheless, a couple of showers affected the study area in late May (Figure 20c).

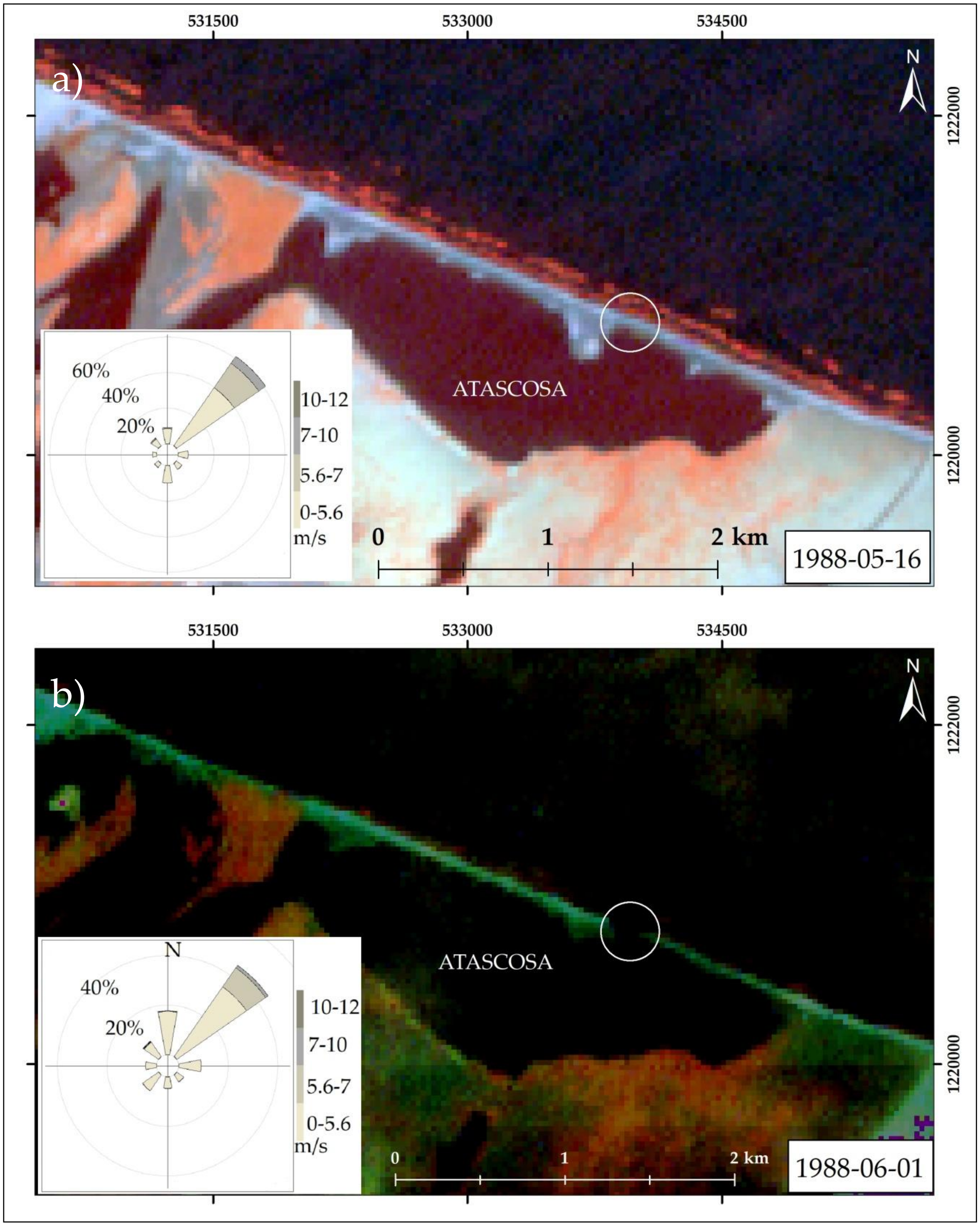

Figure 19. Breaching process for Atascosa lagoon in May–June 1988. a) Last image with no breach taken on May 16, 1988. b) First image with breach taken on June 1, 1988. Wind roses indicate wind conditions two weeks prior to image acquisition. Landsat 4 images courtesy of U.S. Geological Survey. Images displayed combining bands 754.

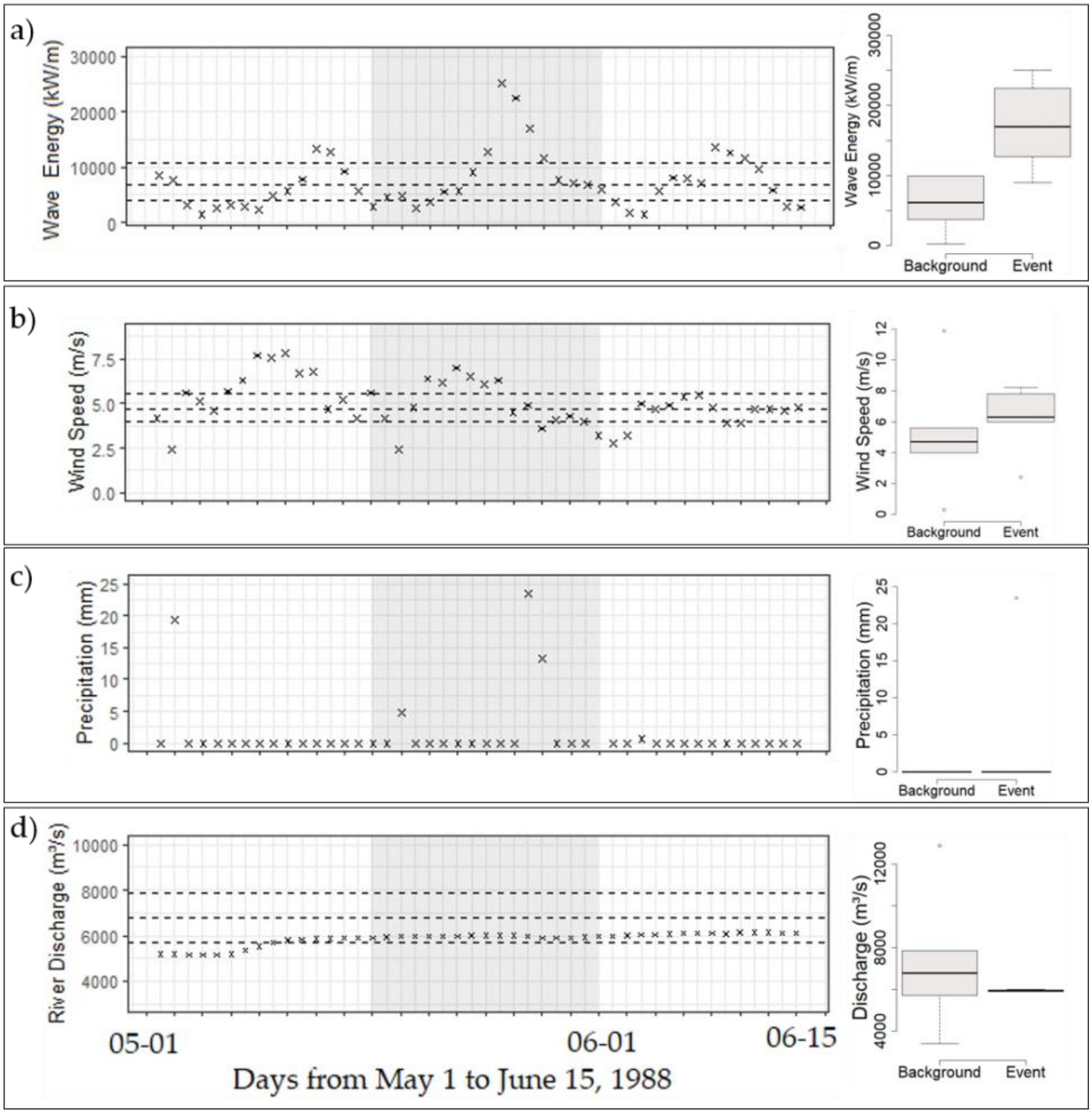

Figure 20. Time series of potential drivers of a lagoon breaching in May 1988. Left panels indicate daily maximums for a) wave energy, b) wind speed, c) precipitation, and d) the Magdalena River discharge. Dashed lines show the 25th, 50th and 75th percentiles for non-event conditions (background) and crosses indicate the conditions before, during (grey shaded area) and after a breaching event. Box plots on the right panels help visualize DBM/OVS ratios reported in Table 2.

3.3.5 High River Discharge Breaching Event in May 2011 (Event 5)

Four of the observed events experienced river discharge higher by >50% with respect to the expected background value (events 2, 5, 12, and 13 in Table 2). One of these events occurred in May 2011 resulting in a breach of the Las Piedras lagoon. The barrier was last observed closed on April 30, 2011 (Figure 21a) and an inlet and a plume of sediment extending from the wetlands adjacent to the lagoon towards the ocean are seen on the May 20, 2011 imagery (Figure 21b). Wave energy and wind speed in the three weeks prior to the detection of the breach fluctuate around average background values with few excursions above the 75th percentile (Figure 22b). The DBM/OVS values indicate overall lower than average wave conditions and above average northerly winds. Precipitation occurs at the end of the month, but overall precipitation is not different from expected values (Figure 22c). Discharge, on the other hand, increased steadily and plateaued around mid May and remained high for the rest of the month (Figure 22d).

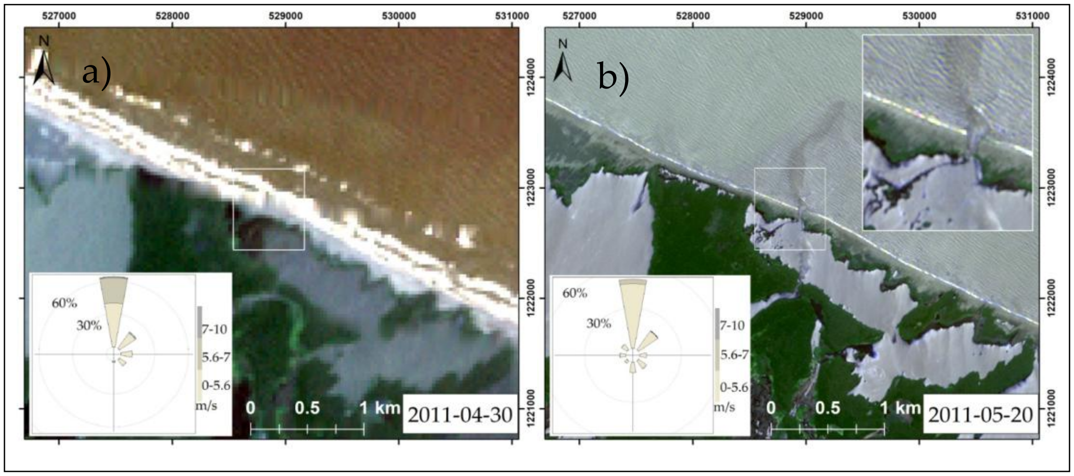

Figure 21. Breaching process for Las Piedras lagoon in May 2011: a) Last image with

no breach taken on April 30, 2011. b) First image with breach and sediment plume taken on May 20, 2011. Wind roses indicate wind conditions two weeks prior to image acquisition. Rapideye imagery courtesy of Planet labs.

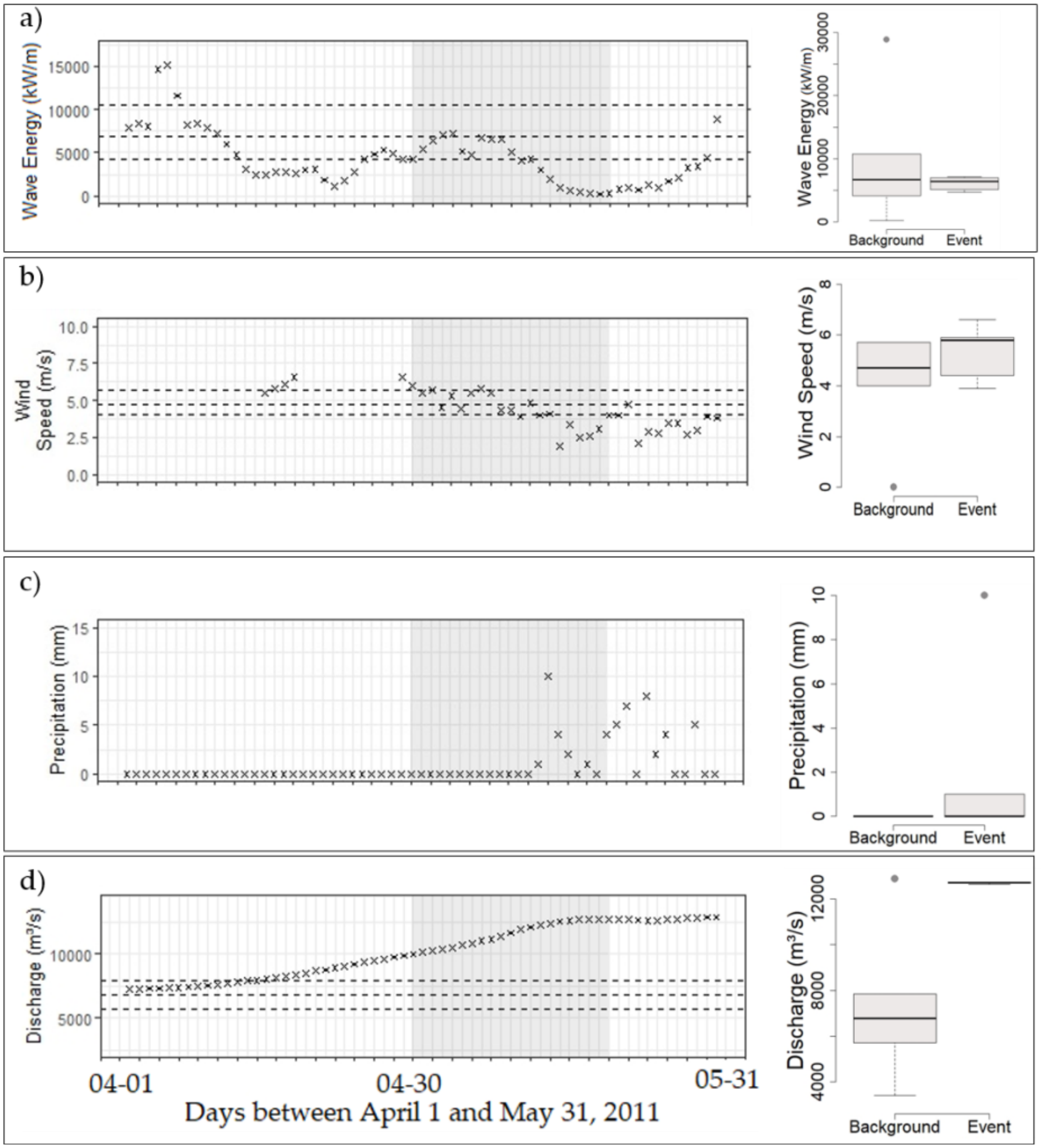

Figure 22. Time series of potential drivers of a lagoon breaching in April-May 2011. Left panels indicate daily maximums for a) wave energy, b) wind speed, c) precipitation, and d) the Magdalena River discharge. Dashed lines show the 25th, 50th and 75th percentiles for non-event conditions (background) and crosses indicate the conditions

before, during (grey shaded area) and after a breaching event. Box plots on the right panels help visualize DBM/OVS ratios reported in Table 2.

3.3.6 High Wave Energy Breaching Event in October 2016 (Event 11)

By the time this event took place, the Cuatro Bocas and Atascosa lagoons had breached in April 2015 and February 2016, respectively (see events 6 and 9 in Table 2 and top panel in Figure 23). Nonetheless, the conditions prevailing during the event of October 2016 produced a second breach on the westernmost sector of the Atascosa lagoon, first seen on imagery from October 31, 2016 (bottom panel in Figure 23). Simultaneously with the appearance of this breach, a reduction in the width of the inlet in Cuatro Bocas from 262 to 161 m is observed (bottom panel in Figure 23). The evolution of this latter breaching is detailed in section 3.5.

Between September and October 2016 the study site experienced the highest maximum wave energy, wind speed and precipitation of all 13 events examined here, resulting in DBM/OVS=97.6% , 76.9% and 20.0%, respectively (Figure 24a-c, Table 2). River discharge measurements, on the other hand, indicated smaller-than-average conditions for October (DBM/OVS=-50.6; Table 2, Figure 24d). During the event, maximum wave energy was more than double that of event 12, which experience the second highest maximum wave energy (Table 2). Specifically, wave energy peaked between November 30 and October 4, 2016 (Figure 24a). A switch from northeasterly to southwesterly wind direction is observed (Figure 23), and SLP gradients were above average by more than 50% (Table 2). This event matches the fading of Hurricane

Matthew, which crossed the Caribbean Sea between September 28 and October 16, 2016 (Mendoza et al., 2013).

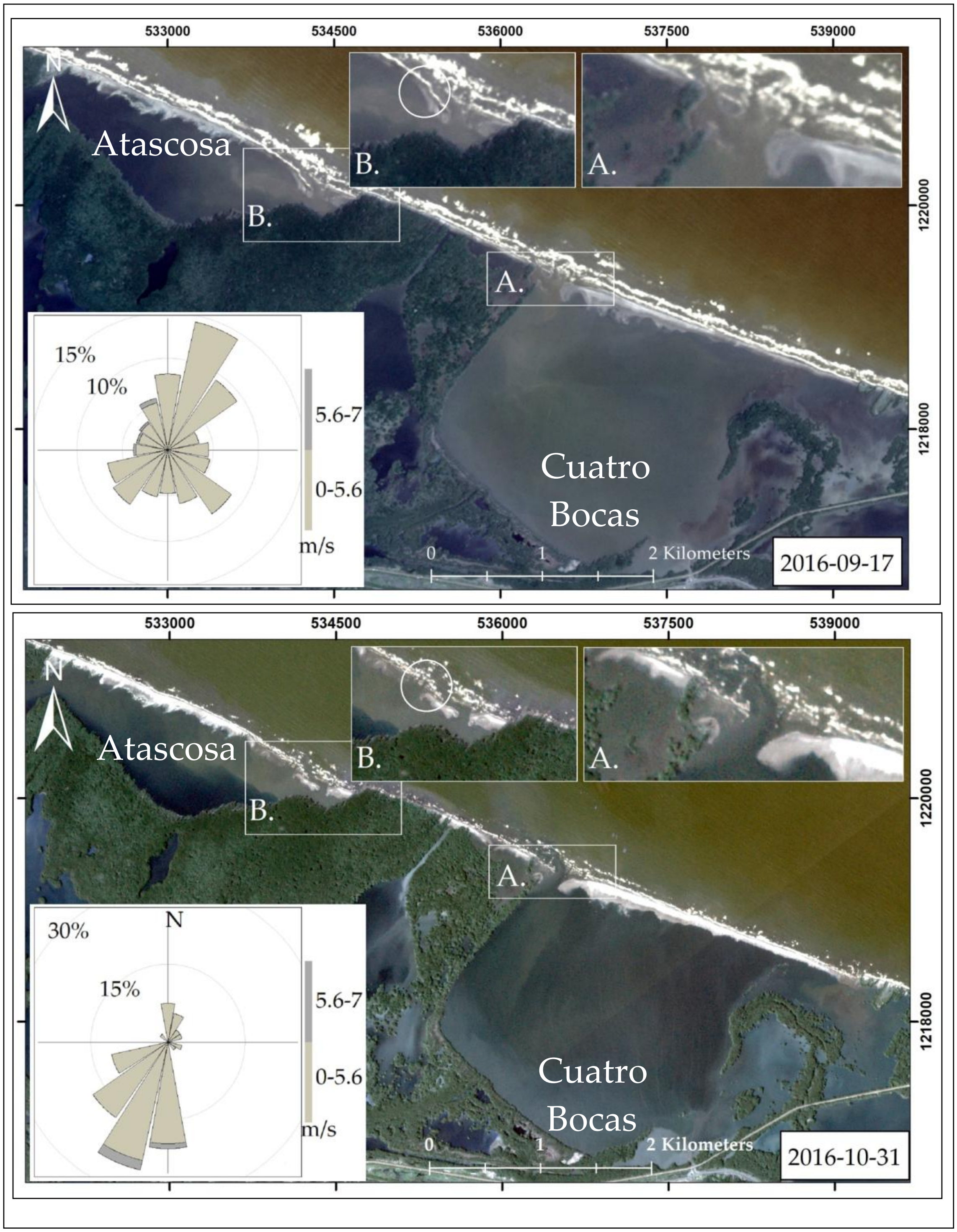

Figure 23. Breaching process for the La Atascosa lagoon in October 2016. Top: image taken on September 17, 2016 showing prior breachings but an intact barrier otherwise.

Bottom: image shows that a second breach was formed (circled area) in the Atascosa lagoon. Wind roses indicate wind conditions two weeks prior to image acquisition. Rapideye imagery courtesy of Planet labs.

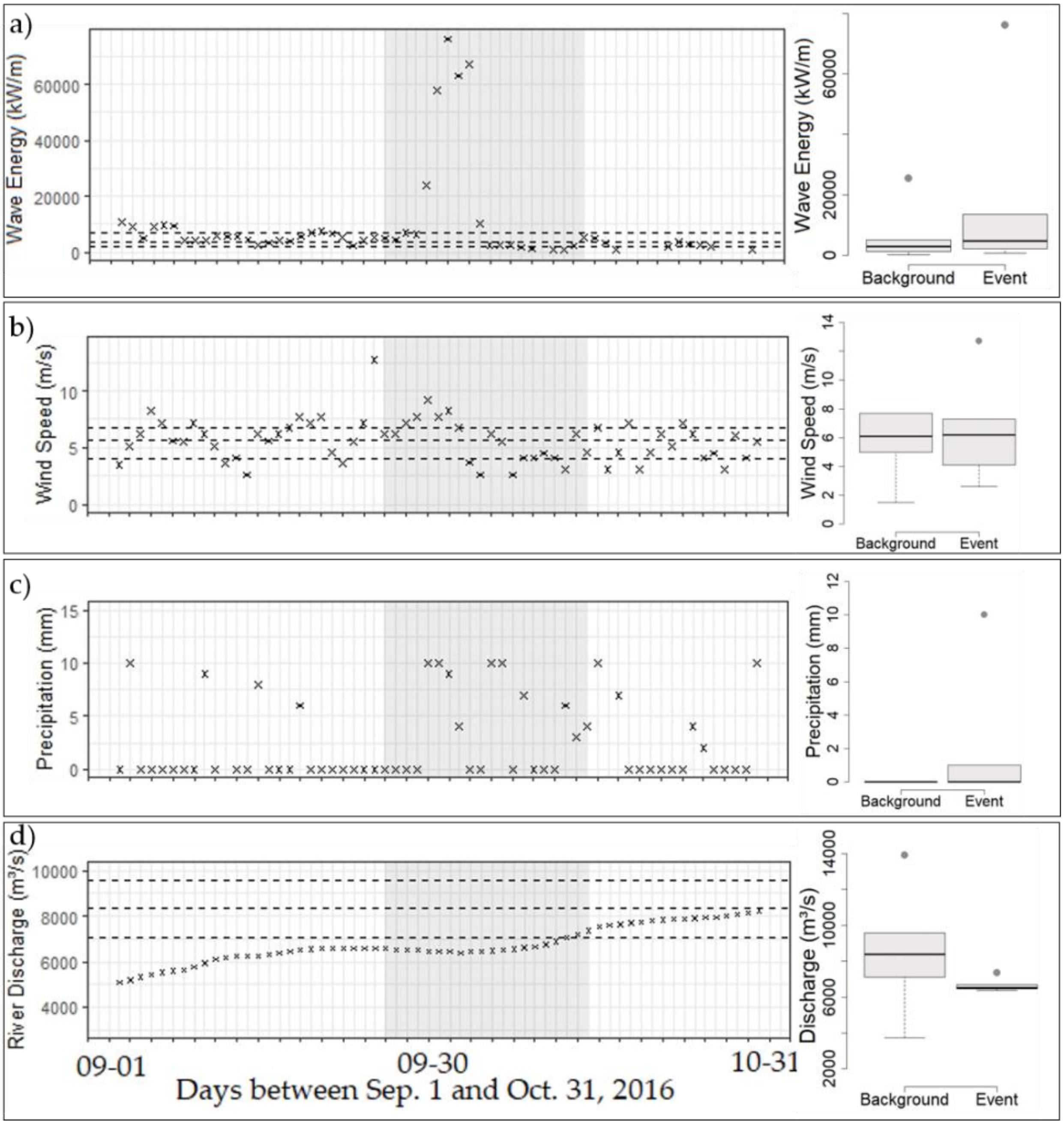

Figure 24. Time series of potential drivers of a lagoon breaching in September-October 2016. Left panels indicate daily maximums for a) wave energy, b) wind speed, c) precipitation, and d) the Magdalena River discharge. Dashed lines show the 25th, 50th and 75th percentiles of average non-event (background) and crosses indicate the

conditions before, during (grey shaded area) and after the event. Box plots on the right panels help visualize DBM/OVS ratios reported in Table 2.

3.3.7 Barrier Healing Processes

A summary of the 13 healing periods examined here is provided in Table 3. Note that the last detected breach (No. 13) was still open at the end of the observation period. Seven out of the thirteen healings were completed between January and May (Table 2). Out of these, some events (namely No. 1, 2, 5, 8, 10, 11, and 12 in Tables 1 and 2) were breached for over 200 days. Breachings that took place after the first quarter of the year healed between April and July, less than 3 months after the lagoon had breached (namely No. 3, 4, 6, and 7 in Table 1 and Table 2). The shortest and longest span that a breach took to heal was in the La Atascosa lagoon, with 32 days (event 9) and 565 days (event 11), respectively. In the following, we will examine four sequential breaching-healing episodes in the Cuatro Bocas lagoon. The sequence started with a breach in the middle of the lagoon in April 2015; after the lagoon healed by July 2015, successive healings and breachings moved westward until April 2017, when the westernmost extreme of this lagoon was healed.

Table 3. Lagoon healing conditions for the period 1973-2020.

Healing No.	Lagoon breached	Date healing detected	Duration of healing (days)[1]	Maximum width detected (m)
1	Atascosa	1989-01-11	224	300
2	Las Piedras	2001-03-01	248	80
3	Cuatro Bocas	2004-07-31	80	130
4	Cuatro Bocas	2009-11-26	56	110
5	Las Piedras & Atascosa	2012-03-12/20 11-09-21	297/124	95/100
6	Cuatro Bocas	2015-07-13	87	80
7	Cuatro Bocas	2015-10-22	84	170
8	Cuatro Bocas	2016-05-25	201	550
9	Atascosa	2016-03-26	32	21
10	Cuatro Bocas	2017-04-06	299	435
11	Atascosa	2018-05-03	565	505
12	Atascosa	2019-02-25	225	91
13	Las Piedras	n/a[2]	>117	186

[1] Estimated time based on image availability.

[2] Las Piedras lagoon was still breached on December 31, 2020.

3.3.8 Healing processes between April 2015 and April 2017

After a first breaching of the Cuatro Bocas lagoon in April 2015 (Event 7 in Table 2), various breachings occurred each westward from the previous event. Imagery of the two year period following the initial event and subsequent breaching and healing times are illustrated in Figure 25.

Healings typically took place during lengthy periods of fair weather that were at times interspersed by extreme wave energy events (Figure 26). For instance, no extreme conditions in wind speed, precipitation, or river discharge were observed during the healings highlighted in Figure 25 and Figure 26, and average wave energy values prevail most of the time during the healing periods (25a). Nonetheless, fair weather wave climate was punctuated by extremely high energy episodes in three of the four healings illustrated in Figure 25 (Figure 25, H1 (May–July 2015), H3 (November 2015–May 2016), and H4 (July 2016–April 2017)). Additionally, these healing processes were associated with northeasterly winds (Figure 25). Particularly, during the healing that occurred between July 2016 and April 2017 (H4), two high-energy wave pulses with values up to 40,000 kW/m and prevailing northeasterly winds underlie the last stages of the healing process (Figure 25 and 25). By the beginning of March 2017, a peak of wave energy and northeasterly winds with speeds above 7.5 m/s occurred prior to a reduction in the inlet from 45 to 36 m (lower panel in Figure 25). Subsequently, another peak of wave energy occurred between 31 March and 6 April before the healing of the inlet (lower panel in Figure 25 and Figure 26a). Aside from some showers in October–November 2016, no increased precipitation was observed before the healings (Figure 26c).

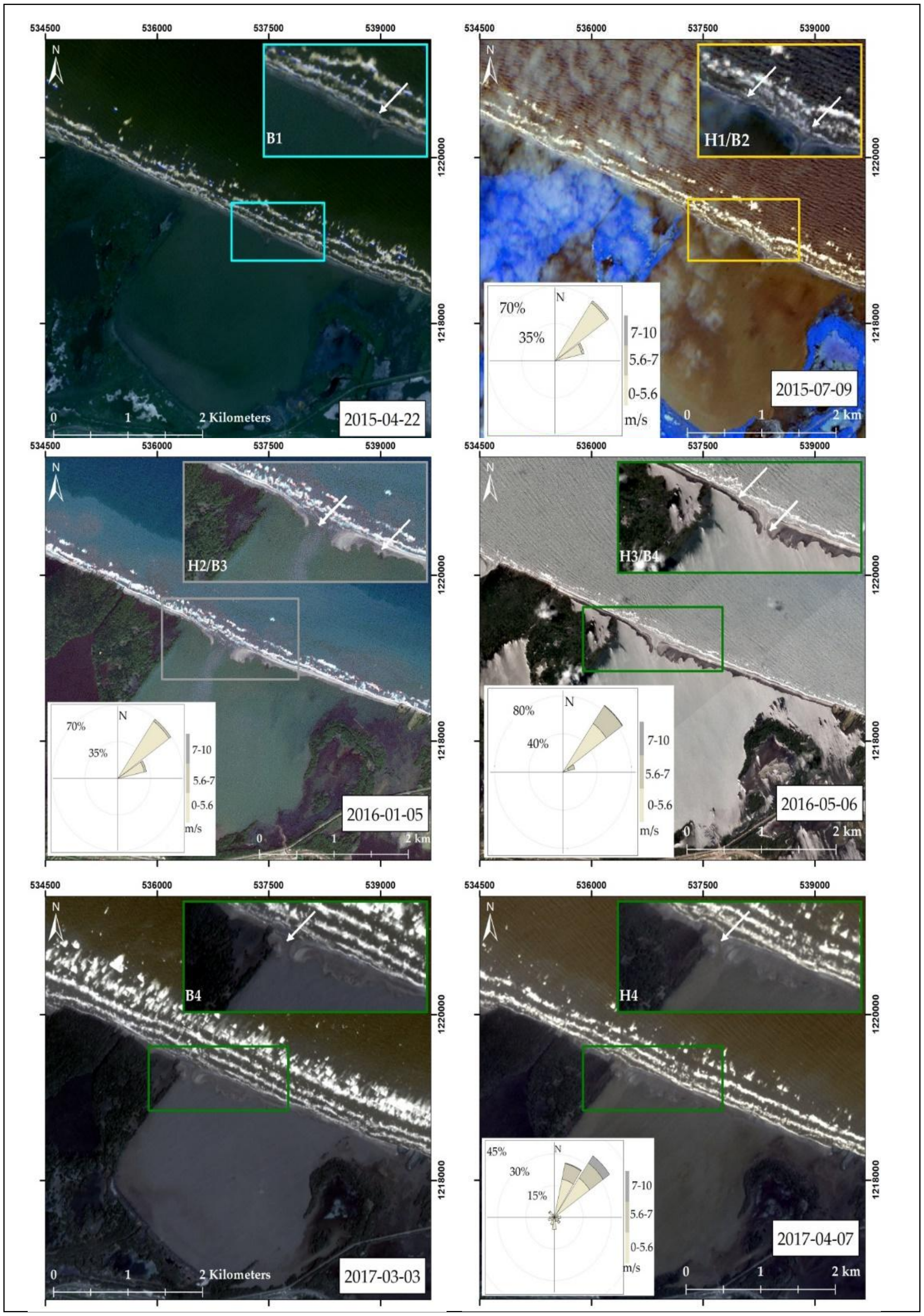

Figure 25. Color-coded sequence of breaching (B)-healing (H) processes for Cuatro Bocas lagoon between April 2015 and April 2017. Wind Rose indicates wind conditions prior to the healing.

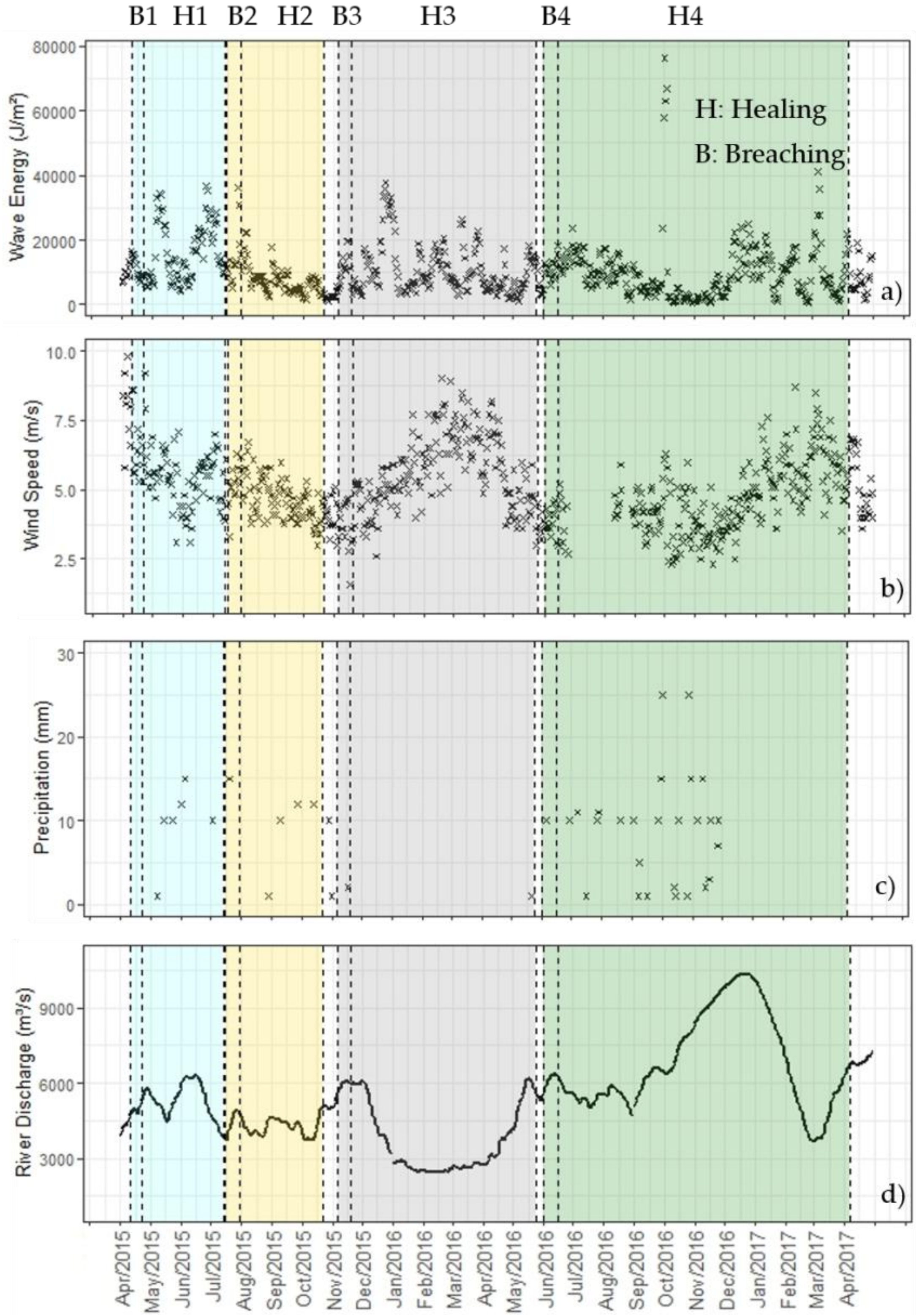

Figure 26. Color-coded daily maximum of potential drivers of lagoon healing and breaching in Cuatro Bocas between April 2015 and April 2017. Panels indicate maximum daily values for (**a**) wave energy, (**b**) wind speed, (**c**) precipitation, and (**d**)

the Magdalena River discharge. Vertical dashed lines indicate the ranges of breachings and healings.

3.3.9 Summary of Coastal Morphodynamics

A summary of the observed trends in coastline retreat, barrier and lagoon morphometry, and breaching and healing characteristics is provided in Figure 27 and Table 4. Accordingly, breaching occurs more often in the most erosive sector of the study area (i.e., along Cuatro Bocas), and on average, breachings along this sector also heal faster. High erosion rates in this sector also coincide with large changes in the area and shape of the Cuatro Bocas and La Atascosa lagoons for 1973–2020 (Figure 27 and Table 4). In contrast, the lower coastal erosion rates westward from La Atascosa are mirrored by smaller areal lagoon changes and a lower frequency of breachings in Las Piedras and El Torno lagoons. The largest inlet length was observed in the El Torno lagoon in January 1973 (Table 4).

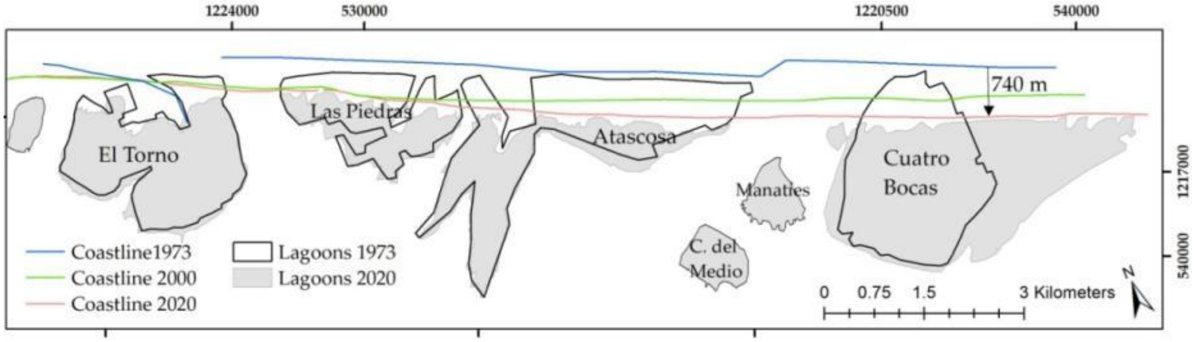

Figure 27. Landward translation of coastlines and lagoons since 1973.

Table 4.Distribution of average morphometry metrics for lagoons in the Magdalena River Deltaic Barrier for 1973-2020.

	El Torno[1]	**Las Piedras**	**Atascosa**	**Cuatro Bocas**
Mean Barrier Width before breaching (m)	NA	56	44	48
Mean Length of Inlet (m)	1158	181	249	258
Number of Breachings	1	8	12	13
Mean duration of healing (days)	>4780	282	292	135
Mean Coastline Changes (m/yr)	-2.3	-12.8	-13.9	-17.0
Area 1973 (km^2)	4.11	2.42	4.97	4.70
Area 2020 (km^2)	3.91	1.68	2.97	7.03

[1] Inlet that remained open from a breaching prior to 1973.

3.4 DISCUSSION

Given the small number of events in this analysis (N=13), we examined the importance of hydro-climatic parameters for lagoon breaching and healing by comparing the difference between event and non-event (background) conditions rather than performing a statistical analysis. Accordingly, extreme conditions of wave energy and/or river discharge coincided with the occurrence of the breachings and healings analyzed in this work (Table 2 and Table 3).

3.4.1 Drivers of lagoon breaching

3.4.1.1 Oceanographic Process Dominant

Most of the breaches analyzed in this work were preceded by increases in wave energy larger than 35% with respect to average conditions, which translated to wave heights larger than 2 m. These energetic sea states were often associated with northerly and northeasterly winds resulting from strong sea-level pressure gradients across the Caribbean Sea. In fact, with the exception of event 8, SLP was above average for all the events (Figure 17c and Table 2). Previous empirical evidence for other Caribbean sites has linked anticyclonic storm events to cold fronts (Ortiz-Royero et al., 2013; Bernal et al., 2016; Mendoza et al., 2013 , Rey et al., 2019). Similarly, our findings indicate that the legacy of such events can be found in the breachings they trigger during high energy sea states that have traveled a distance from their source of generation; these storms are reflected in the local weather by sporadic showers and winds speeds above 6 m/s.

In addition to high wave energy resulting from cold fronts, high energy events associated with the passing of hurricanes in mid-August to late October may trigger the breaching of lagoons (Hapke et al., 2013; Miselis et al., 2016; Sherwood et al., 2023). In the study area, hurricanes Lenny (November 1999) and Matthew (October-November 2016) enabled the breaching of the Atascosa lagoon (Event No. 11 in Table 2). Nonetheless, unlike the annual periodicity of cold fronts, extreme waves due to hurricanes rarely affect the Continental coast of Colombia (Ortiz-Royero et al., 2021).

3.4.1.2 River Process Dominant

Our analysis reveals that the Las Piedras and Atascosa lagoons are prone to washout coupled with river discharge values larger than 10,000 m^3/yr. Such extreme discharges in the Magdalena River are common during La Niña years (Hastenrath, 1990; Poveda , 2004). In fact, the four events with river discharge DBM/OVS percentages larger than 50% occurred during La Niña years (Figure 15g) between the months of May and September (i.e., 2000, 2011, 2018, 2020). As these increases are detected three weeks prior to the first detection of an event, it appears that there is a quick coupling between an increase in discharge at the upstream gauge station and a breach of the barrier (see the grey area in Figure 22d). Elsewhere, some examples of breachings associated with washouts have been reported on the Outer Banks of North Carolina (Miselis et al., 2016; Sherwood et al., 2023), on the Ria Formosa Barrier Island in south Portugal (Matias et al., 2008), and on the Muni-Pomzadze lagoon in Ghana (Davies-Vollum et al., 2019).

3.4.2 Lagoon healing

Ten out of the 13 healing processes analyzed occurred during a period of increased wave energy, either during January–April or June–July (see Table 3). We detected that most of the breaches close within the next high-energy wave season and that only one breaching (No. 11 in Table 3) lasted over more than one wave season. High wave energy, therefore, might cause the lagoons to breach, but extreme energy events are also a driver of lagoon healing. Video-monitoring observations of shorelines and associated sandbars have shown that, depending on the absolute position of the sandbars and shoreline, the same level of high wave energy events can cause either erosion or accretion in different instances along a coastline (van de Lageweg et al., 2013). Hurricane Matthew (September–October 2016) exemplified the mixed effect of an episode that breached the Atascosa lagoon while simultaneously reducing the size of an existing inlet in Cuatro Bocas (Figure 25). Previous reports of accretion due to elevated water levels associated with washovers have been described in the Skallingen Barrier, Denmark (Aagaard, 2019).

A spatial and temporal comparison of the distribution of historical and active inlets in the mid-Atlantic Bight on the U.S. East Coast found that, after being opened by storms, inlets along wave-dominated barrier islands migrate along the direction of longshore currents (McBride, 1999). Similarly, our results show that once an inlet is formed, by trapping the sediment that otherwise would have traveled westward, a deficit of sediment is created downdrift. Thus, those areas located downdrift (i.e., westward) of an inlet are more prone to breach, and when there exist two simultaneous breachings, the easternmost (updrift) breach heals first (e.g., Event 5 in Table 3).

We postulate that the healing of breachings associated with oceanographic events has resulted in the landward displacement of the coastline observed and the shrinking of the lagoons (or encroachments onto the surrounding wetlands in the case of Cuatro Bocas). Similarly, the conceptual model developed by Zăinescu et al. (2019) for the Danube Delta (Figure 28) shows aggradation and stabilization of the landward deposit following an oceanographic-driven breaching, resulting in a landward translation of the barrier. We extend this model to capture the coastline evolution following healings associated with washout (river driven) events (Figure 28d–f). Previous work points out that washouts provide a temporal setback to coastline transgression due to sediment depositing seaward from the barrier and contributing to short-term stabilization (Sherwood et al., 2023).

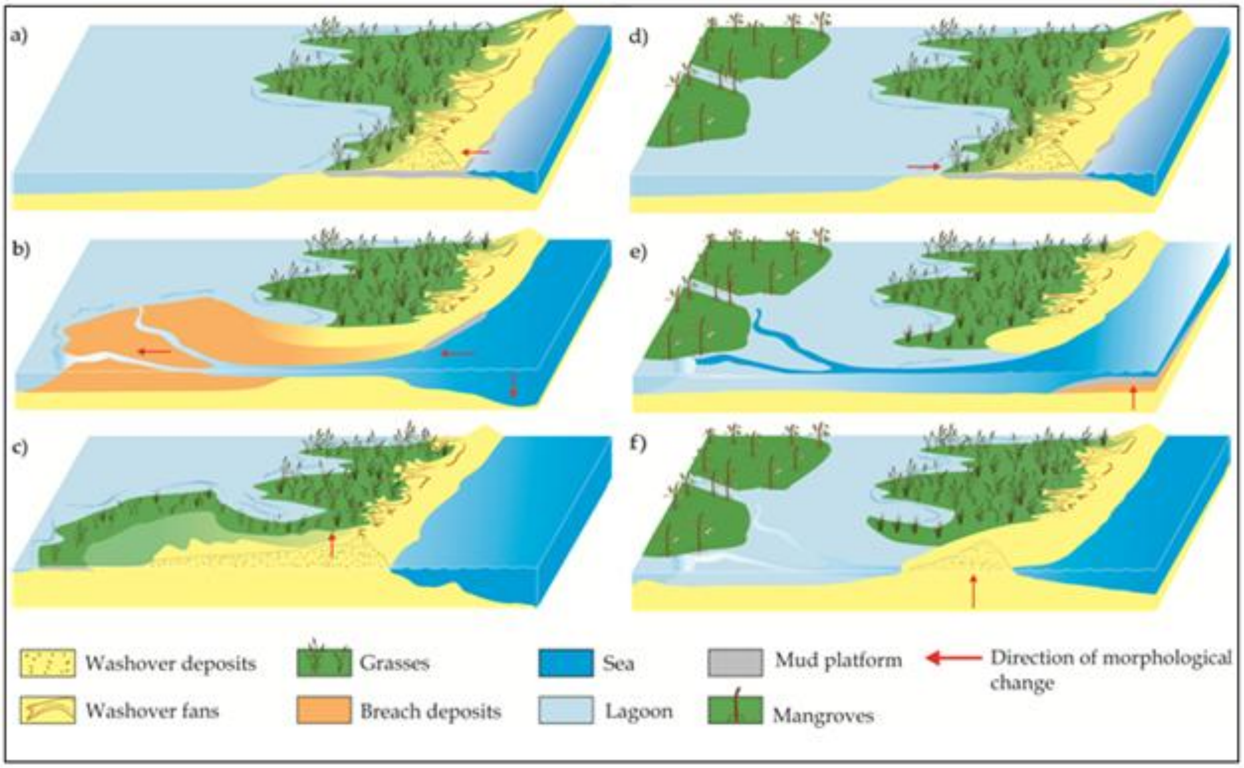

Figure 28. Three-phase conceptual model of barrier evolution driven by an oceanographic breaching (left) and high discharge of river (right). Left side: (a) shoreline retreat and negative sediment balance prevail before the breaching; (b) depositional lobe results from the landward mobilization of sediment during the breaching, and (c) healing is followed by barrier aggradation and stabilization of the lagoon deposit, favored by colonizing vegetation species. Right side: (d) increased river discharge causes high lagoon water levels landward of the unbreached barrier; (e) breaching from the landward side causes subaqueous deposit seaward and aggradation of the shoreface, (f) followed by healing process and reduction in the lagoon size. Red arrows indicate the direction of significant morphological change (Modified from Zăinescu et al. (2019). (a–c) are reproduced from Zăinescu et al. (2019), (Figure 13).

In our study site, frequent breachings, particularly in the eastern portion, both triggered by oceanographic and river-driven events, complicates this conceptual model, where washout sediment may contribute to the aggradation of the shoreface, or sediment deposited landward may be disrupted from stabilizing by another breach. The long-lasting breach of the El Torno lagoon, which occurred prior to our study period and remained open for decades before healing, does point towards stabilization of the landward deposit; since the healing of this lagoon was completed in the mid–1980s (Gómez, 2015), colonizing species (e.g., *Sporobolus virginicus, Cyperus ligularis,* and *Sesuvium portulacastrum*) have established over the barrier and developing embryo dunes (Gómez, 2015).

3.4.3 Differential Evolution of the Deltaic Barrier

From the four lagoons analyzed in this study, the Cuatro Bocas and El Torno lagoons can be considered two end members with respect to the littoral transport and overall coastal dynamics (updrift/erosive regime and downdrift/accretive regime, respectively) (Gómez et al., 2016; Gómez et al., 2021). Accordingly, the width of the barrier seaward of Cuatro Bocas and El Torno in 2020 was approximately 50 m and 700 m, respectively (Figure 17, Figure 27, and Table 4). Interestingly, Cuatro Bocas increased in areal extent through encroaching adjacent wetlands, while the other lagoons decreased in size, with the largest shrinking occurring in the lagoons located just downdrift of Cuatro Bocas, where erosive regimes are predominant (Figure 18 and Figure 27). The variation in the barrier width is mirrored by the number of breaching events in each of these lagoons since 1973—13 and 0 for the Cuatro Bocas and El Torno lagoons, respectively—(Appendix 2 and Table 4). Aagaard (2019) point out that, in relatively wide barriers (>400 m), overwash deposits and aeolian sediment is retained subaerially, whereas in narrow barriers, a significant volume of the overwash sediment is transported to back-barrier lagoons. As a result, narrow barriers will more often tend to migrate landward (i.e., through rollover), while wide barriers may recover through aggradation.

Even though alongshore sediment transport does not directly contribute to back-barrier evolution, it influences the evolution of a barrier by modulating its width and, consequently, the contribution of overwashes in the offshore-onshore transport of sediment (Jiménez and Sánchez-Arcila, 2004). The contribution of longshore sediment transport to the coastline morphodynamics was observed in the study area, where frequent breaching and healing have led to a landward displacement of the coastline, foredune erosion (Figure 15) and change in the shape of the lagoons (Figure 18) in updrift locations, whereas in the downdrift area, the coastline is accreting and no breachings were detected in the El Torno lagoon during the study period. Our findings of landward migration of the coastline through the landward displacement of sediment via breachings align with computer models that have identified that the landward migration of barrier islands (i.e., rollover) is supported by sediment delivered to the back-barrier through overwash (Leatherman, 1979; Lorenzo-Trueba and Ashton, 2014) and breachings. As there is a critical barrier island width and height that needs to be met before waves overtop the dune/beach ridge and overwash reaches the back-barrier (Lorenzo-Trueba and Ashton, 2014), a differential barrier response is expected based on the morphology. We observed average barrier widths equal to or less than 50 m before the breachings took place, but more systematic monitoring, using, for example, unmanned aerial vehicles, must be carried out to narrow down the critical width and elevation for the site-specific environmental conditions. Previous works have reported critical barrier widths of 122 m for overwashes to be effective in producing barrier island migration on the back-barrier shore of Assateague Island in Maryland (Leatherman, 1979), whereas a big breach on the Scalin Spit in the Danube Delta was preceded by a barrier width ranging between 50 and 150 m (Zăinescu et al., 2019).

The general trend of barrier width reduction along the deltaic barrier (Figure 18) suggests that a further reduction in sediment supply resulting from, for example, building coastal defense structures updrift could trigger a breakdown of the longshore drift system and, as a result, drowning of the most vulnerable stretches of the barrier. To date, coastline retreat has taken place at the expense of the areal reduction in the lagoons, the Cuatro Bocas lagoon encroaching adjacent wetlands, as well as the erosion of foredunes (Figure 15) with possible implications for the sensitive wetland ecosystems. Recent government efforts to dredge and clean vegetation from some of the channels connecting the Magdalena River and the lagoons may help to strengthen the frequency of washouts. Although these interventions are aimed at restoring some of the former influence of the Magdalena River in the study area, they will likely not be able to account for the loss of sediment delivery to the study area since the early 1900s.

3.5 Conclusions

This work examines the hydro-climatic drivers behind lagoon breaching and healing and morphodynamic evolution along a deltaic barrier in the Colombian Caribbean. Our findings suggest that short-term drivers play a key role in the evolution of the deltaic barrier and may cause different effects along one stretch of coastline due to variations in morphology, sediment supply, and the driver behind the breaching event.

The lagoons analyzed in this work are along the Magdalena River deltaic barrier, though the river’s influence in the study area has been lessened due to engineering since the 1920s. The main triggers of the breaching of the barrier lagoons are storms, Magdalena River discharge oscillations, and, less frequently, hurricanes. Breachings are more prone to occur in narrow sectors of the barrier located updrift of the longshore sediment supply. Healing occurs following stormy conditions but may take several stormy seasons, particularly when the breached inlet is wide. Consequently, healing processes are driven by the interplay between peak wave energy events, fair weather conditions, and longshore sediment transport. Overall, the cumulative response of the lagoons to breachings and healings has resulted in the landward displacement of the coastline during at least the last 50 years—a reduction in barrier width and changes to the areal extent of the lagoons.

Chapter 4. First detection of a meteotsunami in the Colombian Caribbean and its role as a driver of coastal morphodynamics.

Juan Felipe Gómez, Eva Kwoll, David Atkinson, and Ian Walker

In Preparation

Abstract

Meteotsunamis, a tsunami-like long wave caused by a meteorological disturbance that can result in coastal flooding, have not been reported in the Caribbean Sea. By using oceanographic, meteorological, and satellite observations, this work identifies and examines perhaps the first detected meteotsunami in the Colombian Caribbean, and challenges prior interpretations of a submarine landslide generated event. Wavelet analysis applied to water-level readings at tide gauges dating to 2013 revealed the occurrence of discrete tsunami-like waves as indicated by high frequency sea-level fluctuations on 19 July 2017 in Santa Marta, Colombia. An examination of atmospheric pressure, wind, relative humidity, temperature and radar data before and during the event indicated that a cold front system extended from the interior of Colombia to the Pacific Ocean, then translated northward to the Caribbean Sea where it met dry and hot air during the day of the event. These conditions were conducive to instability in the lower troposphere that was mirrored by the sea-level, which resulted in temporary water level increases of up to 0.60 m after 8:00 a.m. (13:00 UTC time) along the coastline surrounding Santa Marta. Values of wave run-up as well as total water levels (TWL) for the meteotsunami are similar to those found during moderate storms and, depending

on the tide height at the time of the event, both phenomena could result in the breaching of lagoons and coastal flooding. Thus, it is advisable that areas next to the coastline along the Colombian Caribbean consider meteotsunamis as a natural hazard that can trigger coastal flooding, erosion, and affect coastal settlements.

Keywords: meteotsunami; run-up; wavelet; observed water level; total water level; convection; atmospheric instability; flooding.

4.1 INTRODUCTION

Meteorological tsunamis, most commonly known as meteotsunamis, are atmospherically induced sea-level oscillations that are enhanced by resonance effects on the open ocean, shelf, and/or within a bay (Rabinovich and Monserrat, 1988; 1996; Monserrat et al., 2006). These oscillations have wave periods similar to tsunami waves (i.e., few minutes to 2–3 hours), but they are triggered by meteorological disturbances rather than by seismic events (Rabinovich and Monserrat, 1988; 1996), submarine landslides, volcanic eruptions or meteorite impacts (Monserrat et al., 2006).

Even though all meteotsunamis are related to a moving atmospheric pressure disturbance that results in an abrupt change in sea-level atmospheric pressure and/or wind speed, a variety of potential atmospheric forcing mechanisms have been documented (Pattiaratchi and Wijeratne, 2015), including: tropical and extra-tropical storms (Carvajal et al., 2017; Dusek et al., 2019), squall lines (Sallenger et al., 1995; Pattiaratchi and Wijeratne, 2014; Kim et al., 2021), frontal passages (Pattiaratchi and

Wijeratne, 2014), atmospheric gravity waves (AGW) (Dragani et al., 2009; Vilibić et al., 2014; Perez and Dragani, 2021), or tumultuous atmosphere conditions (i.e., small-scale atmospheric disturbances) (Šepić et al., 2015). The changes in atmospheric pressure associated with the aforementioned mechanisms may evolve into a meteotsunami when ocean waves are amplified through external resonance processes (e.g., Proudman, Greenspan or shelf resonance) and/or internal resonance processes (natural frequency of bays or harbours) (Monserrat et al., 2006).

Proudman (1929) described a type of resonance that occurs when the atmospheric disturbance translational speed (U) is the same as the speed of long period offshore waves (phase speed, $c=(gh)^{1/2}$, where h is water depth and g is acceleration due to gravity). Thus, the strength of Proudman resonance depends on the matching of the atmospheric disturbance and the speed of long ocean wave (Vilibić, 2008). Greenspan resonance takes place when the alongshore speed of the atmospheric pressure disturbance is close to one of the modes of the edge wave propagation speed (Monserrat et al., 2006). As a result of the Greenspan resonance, the height of the edge waves is increased (Pattiaratchi and Wijeratne, 2015). Another resonance effect, coined shelf resonance, occurs when the natural oscillating period of a continental shelf is equal to the period of atmospherically generated ocean waves. Internal wave amplification and resonance are controlled by local topographic conditions, including water depth, bed slope, and length and width of bays (Monserrat et al., 2006); for instance, funnel-shaped basins or bays contribute to amplify the effect of atmospheric disturbances (Vilibić, 2008) (Figure 29).

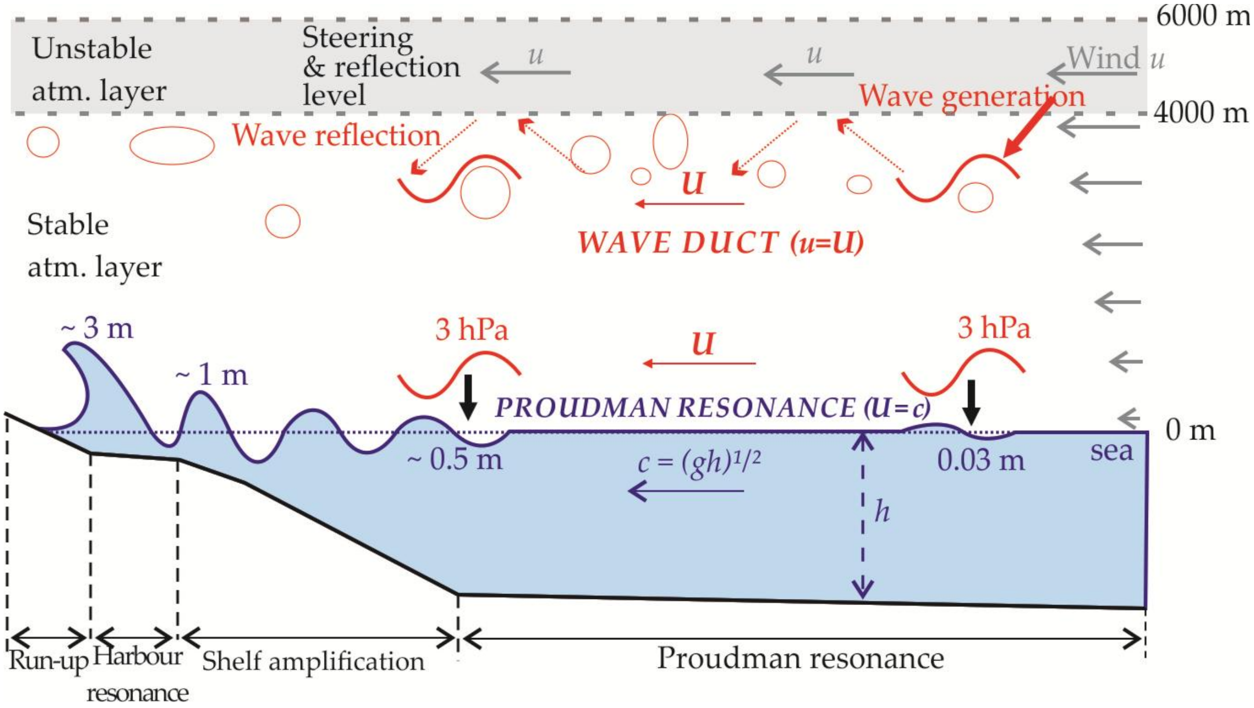

Figure 29. Atmospheric gravity waves (red bubbles) and locale of several resonance processes (e.g., Proudman, shelf and internal wave amplification) that may contribute to generate long-ocean waves during meteotsunamis. Atmospheric gravity waves are generated at the interface of stable and instable atmospheric layers (Modified from Šepić et al., 2015).

Coastal infrastructure situated where microtidal regimes dominate are generally not designed to accommodate large sea level changes (Monserrat et al., 2006), which make these coastlines particularly vulnerable to flooding during meteotsunamis. For example, the island of Korčula (Croatia) in the Adriatic Sea was flooded on June 21, 1978 by a meteotsunami associated with wave heights up to 6 m enhanced by a funneling effect in the Vela Luka Bay (Vučetić et al., 2009). Another damaging meteotsunami with similar wave heights flooded Daytona Beach, Florida, on July 3, 1992. The event in Daytona Beach was attributed to an arc-shaped squall line[1] moving from Georgia at a speed of 14 m/s (Churchill et al., 1995; Sallenger et al., 1995).

One of the most catastrophic meteotsunami events in terms of damage to property and fatalities took place in the city of Dayyer, Iran on March 19, 2017 (Salaree et al., 2018; Heidarzadeh et al., 2020). Field surveys undertaken after the event quantified values of run-up and landward inundations of 3 and 600 m, respectively (Salaree et al., 2018). All of the aforementioned events occurred in locations with intertidal ranges smaller than 1.5 m.

Despite the global distribution of meteotsunamis (Pattiaratchi and Wijeratne, 2015; Vilibić et al., 2021), very few have been documented in the South Atlantic Ocean and none in the Caribbean Sea. In South America, Perez (2018) and Perez and Dragani (2021) have modelled the conditions that favoured past events in the province of Buenos Aires, Argentina. They observed that the characteristics of the simulated meteotsunamis are controlled by the amplitude, dominant period, and direction of propagation of atmospheric gravity waves.

As both storm surges and meteotsunamis are related to meteorological forcing, specifically to changes in atmospheric pressure, there is some contention in attributing

---

[1] Squall lines typically occur when a marine tropical air mass meets a continental tropical air mass at the dry line and are composed of individual thunderstorm cells oriented as lines or wavy lines (Rohli and Li, 2021).

causality to high frequency oscillations of sea level on a coastline.

For instance, Rabinovich et al. (2023) used empirical observations and climate reanalysis datasets to establish that the tail of Typhoon Songda in October 2016 contributed to the formation of a meteotsunami near Vancouver Island in British Columbia, Canada. In contrast, Domps et al. (2022), using high frequency radar operating at 13.5 MHz, argued that observed high sea-levels were exclusively the result of the inverse barometer effect, or storm surge, without the amplification effect due to resonance (e.g., Proudman resonance). Usually, the difference between the two forcing mechanisms is distinguished based on event duration and scale; storm surges are typically associated with storms that last several days and have a regional impact, whilst meteotsunamis are short-lived events on the order of minutes to hours with local impact (Monserrat et al., 2006; Rabinovich, 2020).

As above, the impact of flooding due to meteotsunamis has been previously reported for specific events (e.g., Salaree et al., 2018); however, the impact of meteotsunamis as an external forcing mechanism on coastal landscape dynamics has not been analyzed explicitly in previous works.

The purpose of this research is to investigate the potential occurrence of meteotsunamis in the Colombian Caribbean, the triggers of this phenomenon in the region, and address existing gaps in the literature describing the impact of meteotsunamis on the shoreline dynamics. Particular emphasis was placed in analysing the conditions that caused a sudden variability in sea level reported in the city of Santa Marta, Colombia, on July 19, 2017, and explore related coastal responses in the region. Tide-gauge records were used to detect sea-level oscillations with periods of less than 2 hours. For each period of detected oscillations, local and regional atmospheric data were then used to explain its origin, and a spectral analysis was carried out to identify the period and energy of the oscillation.

4.1.1 Study Area

The study area comprises the coastline between the Colombian cities of Barranquilla and Santa Marta (Figure 30) and was selected due to reports of a sudden sea-level oscillation and potential tsunami in July 2017. A deltaic barrier extends approximately 60 km eastward from the River Magdalena mouth (next to station 18, Figure 30), where average coastal erosion rates of up to -17 m/yr for 1973-2020 are causing loss of beach-dune systems, shrinkage of back-barrier lagoons, impacts to infrastructure, and loss of valuable ecosystems (Gómez et al., 2016; Gómez et al., 2023). Tides in the region are mixed-diurnal with an intertidal range of approximately 0.30 m (Ospino et al., 2018).

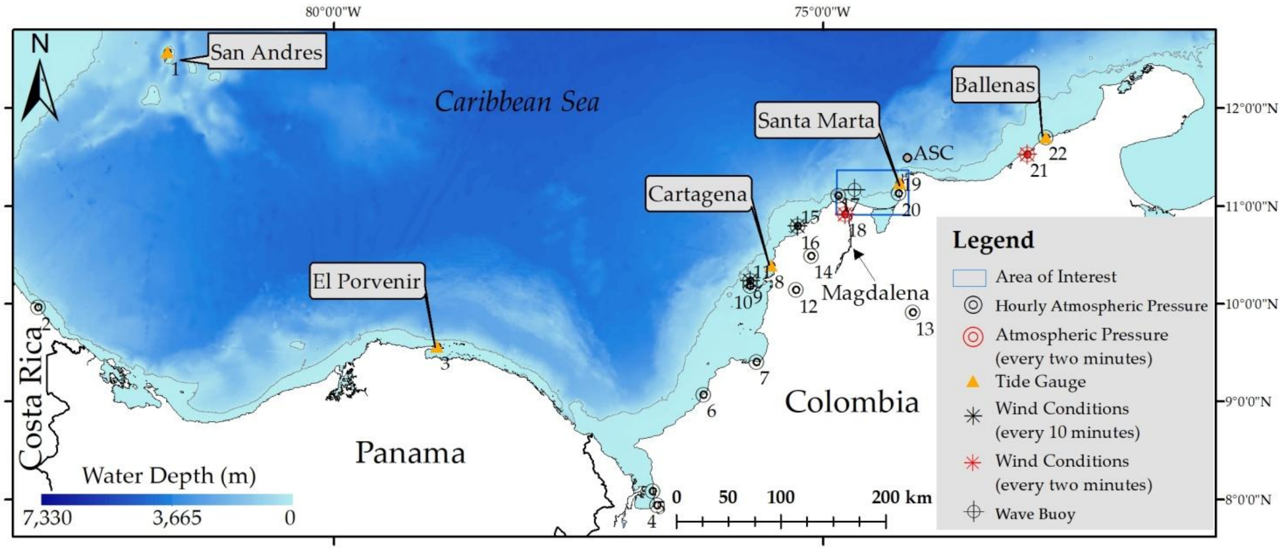

Figure 30. Study area and stations used for data analysis. The approximate seaward edge of the continental shelf (200 m in depth) is shown as a gray line. Locations of tide gauges are labeled. The area affected by the July 2017 event is highlighted with a blue rectangle. Note that Aguja submarine canyon was abbreviated as ASC (grey dot shows approximate location). Bathymetry model was adapted from the General Bathymetry Chart of the Oceans. https://www.gebco.net/ data_and_products/ gridded_bathymetry_data.

During the morning of July 19, 2017, flooding along the area highlighted in Figure 30 began at around 8:15 a.m. local time (13:15 UTC time) due to a sudden rise in sea level that affected coastal settlements, especially the city of Santa Marta. The event was reported by local newspapers (www.elpais.com.co/colombia/inundaciones-en-magdalena-serian-por-una-pequena-onda-de-tsunami.html), blogs (https://blogs.agu. org /landslideblog/2017/08/01/santa -marta -1) and eye-witnesses. Videos recorded by inhabitants of the area show that the high water levels were preceded by a withdrawal of the ocean along the coast (www.youtube.com/watch?v=v-6SDXl7M6s). Allegedly, a submarine cable was broken offshore of the study area due to the event, which resulted in the suggestion that the short-lived sea-level disturbance was caused by a submarine landslide (https://www.elheraldo.co/barranquilla/causas-de-la-onda-de-tsunami-se-estableceran-esta-semana-cioh-385763). Bathymetric surveys developed offshore of the area of interest, specifically in the Aguja submarine canyon (ASC in Figure 30) and offshore of the current mouth of the Magdalena River, reported evidence of previous submarine landslides along the border of the continental shelf (Vargas and Idárraga-García, 2014; Idárraga-García and Vargas, 2014)

A couple days after the event, a Colombian navy ship, the ARC Providencia, surveyed the area offshore of Barranquilla and Santa Marta using a multibeam echosounder, but no clear evidence of a recent submarine landslide was found (Cap. Julio Monroy, personal communication, July 2023). Our study challenges prior interpretations that this event was caused by a submarine landslide and investigates the hypothesis that it was an atmospherically-induced meteotsunami.

4.2 METHODS

Examination of the July 2017 event and the search for other similar events was based on tide gauge records, atmospheric pressure, temperature, wind data, and synoptic weather information for the Caribbean basin. Data gathered from onshore and offshore stations were checked for quality control and local time was converted to Universal Time Coordinated (UTC) time.

4.2.1 Analysis of tide gauge readings in the Southwestern Caribbean Sea (Wavelet analysis)

One-minute readings from two tide-gauge stations in Colombia (Santa Marta/id 1929 and San Andrés Island/id 1930) and from a station located in Panama (El Limón/ id 1901) (orange triangles in Figure 30) were downloaded from the UNESCO sea level station monitoring facility page (http://www.ioc-sealevelmonitoring.org) for the period 2013–2022, the longest record available for any of the stations. The time-series contained lengthy gaps which were replaced by NaN (Not a Number) characters before analysis.

Data from two additional tide gauges located in the Colombian Caribbean, namely Cartagena (id 15A06DCC) and Ballenas (no id provided for this station), located 206 km southwest and 170 km northeast from Santa Marta, respectively (numbers 8 and 11 in Figure 30), were obtained through a formal request to the Maritime Directorate of the Colombian Navy (hereafter, DIMAR). After the request, only one-minute tidal readings for the month of July 2017 were provided. The tidal gauge data were analysed in Matlab, using code provided by NOAA scientist Gregory Dusek; this code has been successfully tested to detect meteotsunamis along the U.S. East Coast (Dusek et al., 2019).

Following Monserrat et al. (2006) and Dusek et al. (2019), two main criteria were used to identify tsunami-like sea-level oscillations for individual years (i.e., one-year segments): i) if the wavelet energy of the non-tidal signal is larger than four-standard deviations (±4σ) of the mean for the selected frequency (1–120 minutes) and, concurrently, ii) if the trough-to-crest wave heights (H) are larger than 0.20 m. Wavelet analysis has been used elsewhere to assess whether a significant amount of energy takes place within the tsunami-frequency band (e.g., Dragani et al. (2009); Kim et al. (2016), Carvajal et al. (2017), Dusek et al. (2019)). Specifically, the Morlet wavelet family helped to identify any time-varying peak of wavelet energy in a frequency band between 1 and 120 minutes. The Morlet wavelet was chosen because it is suited for the detection of fluctuations that come in sudden bursts (de Jong and Battjes, 2004), such as those expected during meteotsunamis.

For the second criterion (H>0.20 m), the tidal component of the signal was removed from the time series by subtracting the observed water level reading from the tide predicted from harmonic analysis. Once the tidal signal was removed, a low-pass filter was applied to the data which provides signals related to either long or short period sea-level oscillations. High-pass-filtered water-level time series were obtained by subtracting the result of the low-pass filter from the original data and was used to capture peak-to-trough wave height values larger than the specific threshold of 0.20 m (Dusek et al., 2019). This threshold was chosen for our analysis because it has been empirically determined that is the smallest wave height value to reliably capture events and avoid false positives (Dusek et al., 2019).

4.2.2 Potential Sources of Water-level Variability

To analyse whether anomalous wave heights were triggered by an earthquake or atmospheric forcing, data from seismological and meteorological stations situated nearby the study area were analyzed. Specifically, seismic events prior to and on July 19, 2017 were tracked using catalogs provided by the Colombian Geological Survey, the United States Geological Survey (USGS), the International Seismological Center (ISC), and the International Data Centre (IDC).

To determine the role of potential atmospheric forcing in any high frequency sea-level variability captured by the tidal gauges, a web of weather stations was examined along the Caribbean coasts of Colombia, Panama, and Costa Rica. The stations at the airports of Barranquilla and Riohacha, Colombia, which are located 20 and 2 km from the shoreline, respectively, provide atmospheric pressure and wind conditions every two minutes, whereas all of the other 13 stations in the region provide hourly readings (see Figure 30). A similar analysis was done for wind conditions based on data gathered at the aforementioned airports (2-min. readings) and at El Tesoro Island and Galerazamba stations (10-min. readings) (see stations numbered 11 and 15 in Figure 30).

A regional analysis of prevailing synoptic conditions was developed using data obtained from the European Centre for Middle-Range Weather Forecast (ECMWF) ERA-5 reanalysis for the Southern Caribbean Sea prior to and during the event.

ECMWF was used over other reanalysis models because its fine temporal (1 hour) and spatial resolution (0.25°).

4.2.3 Assessment of Short-lived Water Level Variability on the Coastline

Run-up levels were estimated from an empirical model for reflective and dissipative beaches proposed by Stockdon et al. (2006):

$$R = 1.1\ (0.35\beta\left(\frac{Ho}{Lo}\right))^{0.5} + \frac{(HoLo(0.563\beta^2 + 0.004))^{0.5}}{2} \tag{3}$$

In equation 3, R is the run-up elevation, β is the beach slope, and H_0 and L_0 are the deep-water wave height and wave length, respectively. Hourly wave heights and periods were retrieved from a buoy managed by DIMAR located approximately 14 km offshore from the coastline in 150 m water depth (Figure 30). In the event that wave data were not available due to malfunction of the buoy, modeled wave heights and periods derived from JRA-55 reanalysis by Orejarena et al. (2022) were used instead.

The Iribarren number supported the classification of beaches based on the ratio between slope and deep-water steepness (Battjes, 1974) (Equation 4). Low (ξ<0.3) and high (ξ>0.3) Iribarren numbers are indicative of dissipative and reflective beaches, respectively (Ruggiero et al., 2004; Stockdon et al., 2006; Stockdon et al., 2007). The Iribarren number was calculated using:

$$\xi = \frac{tan\ \beta}{\sqrt{Ho/Lo}} \tag{4}$$

where ξ provides the Iribarren number following the same notation as in Equation 3.

Prior field work in the study site by the author identified alongshore-variable beach-face slopes with foreshore values ranging between 4° to 9°. In addition to these reflective angles and to encompass as much of the range of beach-face slope variability as possible, an assessment of TWL for low gradient beaches was included using a hypothetical foreshore angle of 1°.

During extreme storm events, storm surges, combined with astronomical tides, result in an observed water level (OWL) value that corresponds with tidal gauge observations. Following Heathfield et al. (2013), TWL are estimated by adding run-up to the observed water level values (i.e., TWL= run-up + OWL). Accordingly, this work uses OWL as registered at the tide gauge in Santa Marta to obtain TWL related to storms and potential meteotsunamis (Figure 31).

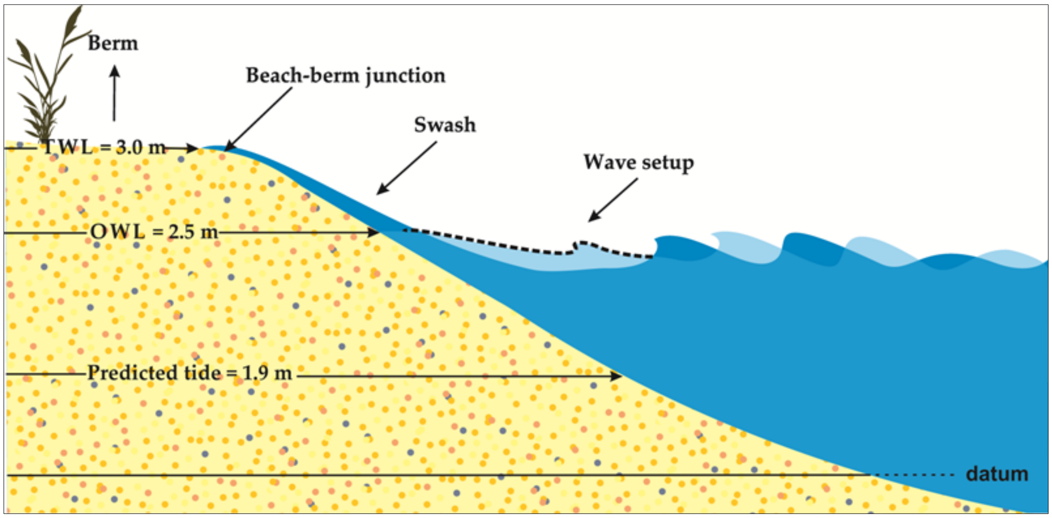

Figure 31. Illustration of swash, wave set-up, OWL and TWL height values during stormy conditions. Not drawn to scale (modified from Heathfield et al., 2013).

4.3 RESULTS

4.3.1 Event Detection from Water Levels

The analysis of time series records from three stations in the Southwestern Caribbean Sea for 2013–2022 indicates only two periods of sea-level oscillations that fulfill both criteria (i.e., H=0.20 m as well as wave heights larger than ±4σ): July 19, 2017 and September 3, 2017. Although time-series of tidal gauges in El Limón and San Andrés Island did not reveal anomalous water level variability during the day of the first event, readings from Cartagena and Ballenas showed that a sea level anomaly was registered around 13:30 (Figure 32b/c) and with highest variability occurring in Ballenas at 18:00. Nonetheless, these events did not fulfill the wave height criterion of 0.2 m.

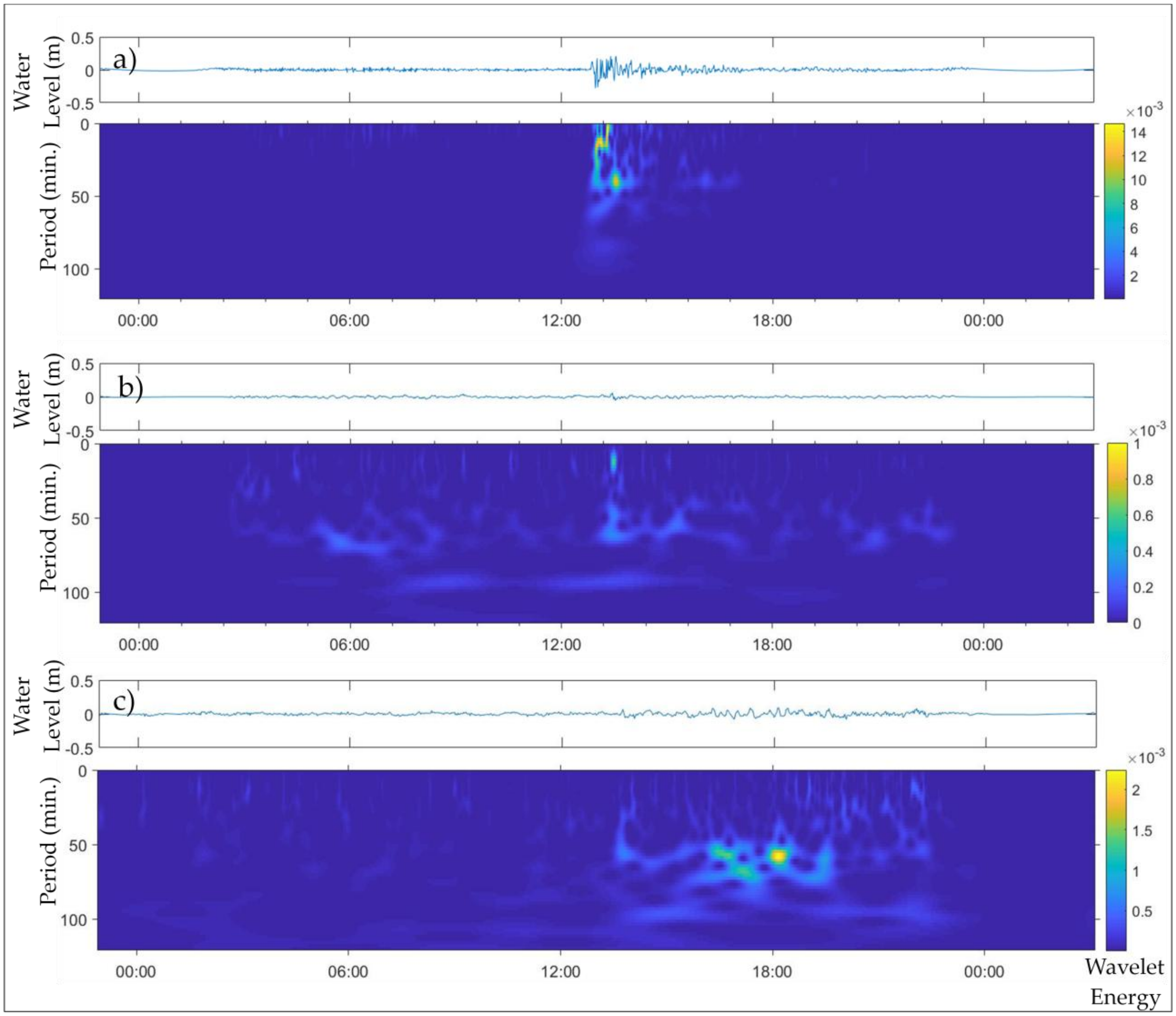

Figure 32. Non-tidal water level (blue line) and wavelet power spectrum on July 19, 2017 for gauges located in a) Santa Marta, b) Cartagena, and c) Ballenas (see Figure 30 for location of the tide gauges).

For the available time series in San Andrés, once the code was run to filter out high frequency sea-level oscillations, numerous spikes in the signal were initially classified as meteotsunamis. After a visual quality control of those instances, it was found that most of these events were artificial errors due to temporal gaps in the tide signal. The second event, detected on September 3, 2017 at 13:43 in San Andrés Island (Figure 33), was not registered by the tides gauges in El Limón or Santa Marta. Data from stations in Cartagena and Ballenas were not available for this period.

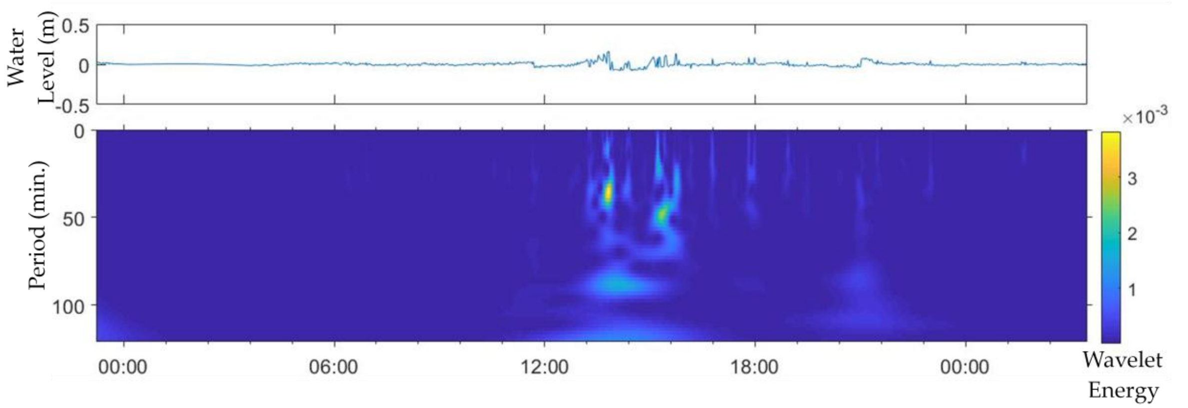

Figure 33. Non-tidal variation of the sea level and wavelet power spectrum at the San Andrés Island tide gauge on September 3, 2017.

4.3.2 Potential Sources of Sea-Level Variability

4.3.2.1 Seismic Sources

Investigation of reports of seismic activity prior to and on July 19, 2017 found no records of earthquakes with magnitudes larger than 2.5 M_L in databases managed by the Colombian Geological Survey or the United States Geological Survey (USGS). The same outcome was confirmed by two additional earthquake catalogs (ISC and IDC) (G. Ekstrom, personal communication, Nov. 2022). Similarly, no earthquakes were reported prior to the sea-level anomaly detected at the tide gauge of San Andrés Island on September 3, 2017.

4.3.2.2 Atmospheric Sources

Regional weather conditions were obtained from satellite radar images facilitated by the Cooperative Institute for Meteorological Satellite Studies of the University of Wisconsin (https://tropic.ssec.wisc.edu/archive), and reanalysis of past atmospheric conditions developed by the ECMWF. The latter source helped to establish average sea-level atmospheric pressure, temperature, and relative humidity between July 10th and July 31st for 1940–2023 (Figure 34); the historical values for 1940–2023 were considered a reference against which atmospheric conditions during July 19, 2017 may be compared. Historically, the lowest values of sea-surface atmospheric pressure (1011.0 hPa) and temperature at 850 hPa (17 °C) are observed nearby the border between Panama and Colombia, whereas maximum temperatures (at 850 hPa) of about 20°C are present in the province of La Guajira, offshore of the northernmost extreme of Colombia. Aligned with the low temperatures offshore of the border between Panama and Colombia, maximum humidity values are observed (Figure 34c).

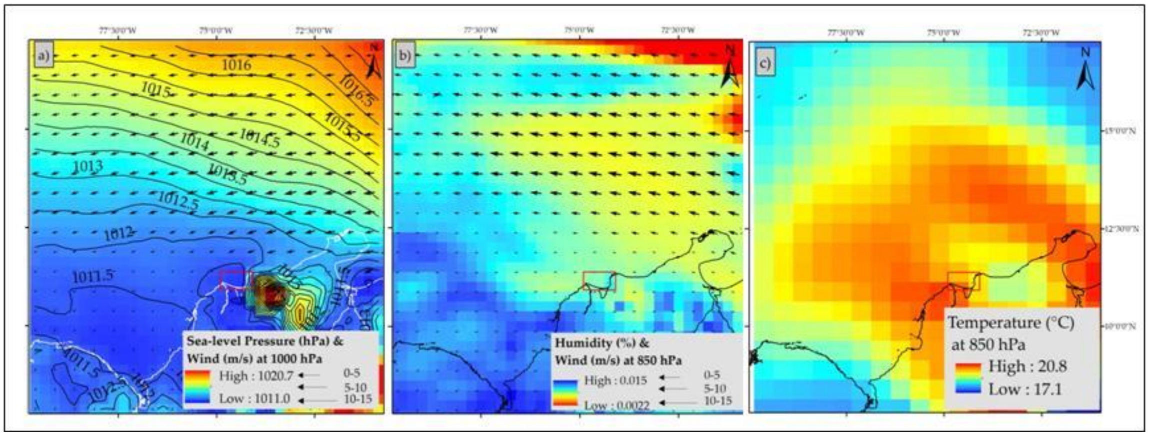

Figure 34. a) Mean sea-level pressure and wind patterns, b) humidity and wind

patterns (850 hPa), and c) temperature (850 hPa) in the Southern Caribbean for July 1940–2023. Hourly data from 1940 to present from Copernicus Climate Change Service (C3S) Climate Data Store (CDS). https://cds.climate.copernicus.eu/cdsapp#!/dataset/reanalysis-era5-pressure-levels?tab=form.

During the event on 19 July 2017, sea-level atmospheric pressure conditions between 9:00 and 14:00 showed that, in conjunction with southeasterly winds ranging from 10 to 15 m/s, a closed low pressure system of 1009.0 hPa developed offshore of the Porvenir station in Panama (Figure 30) between 9:00 and 12:00. Overall, during the day of the event the atmospheric pressure oscillated between 1009.0 and 1013 along the Colombia Coast between 9:00 and 13:00 (Figure 35).

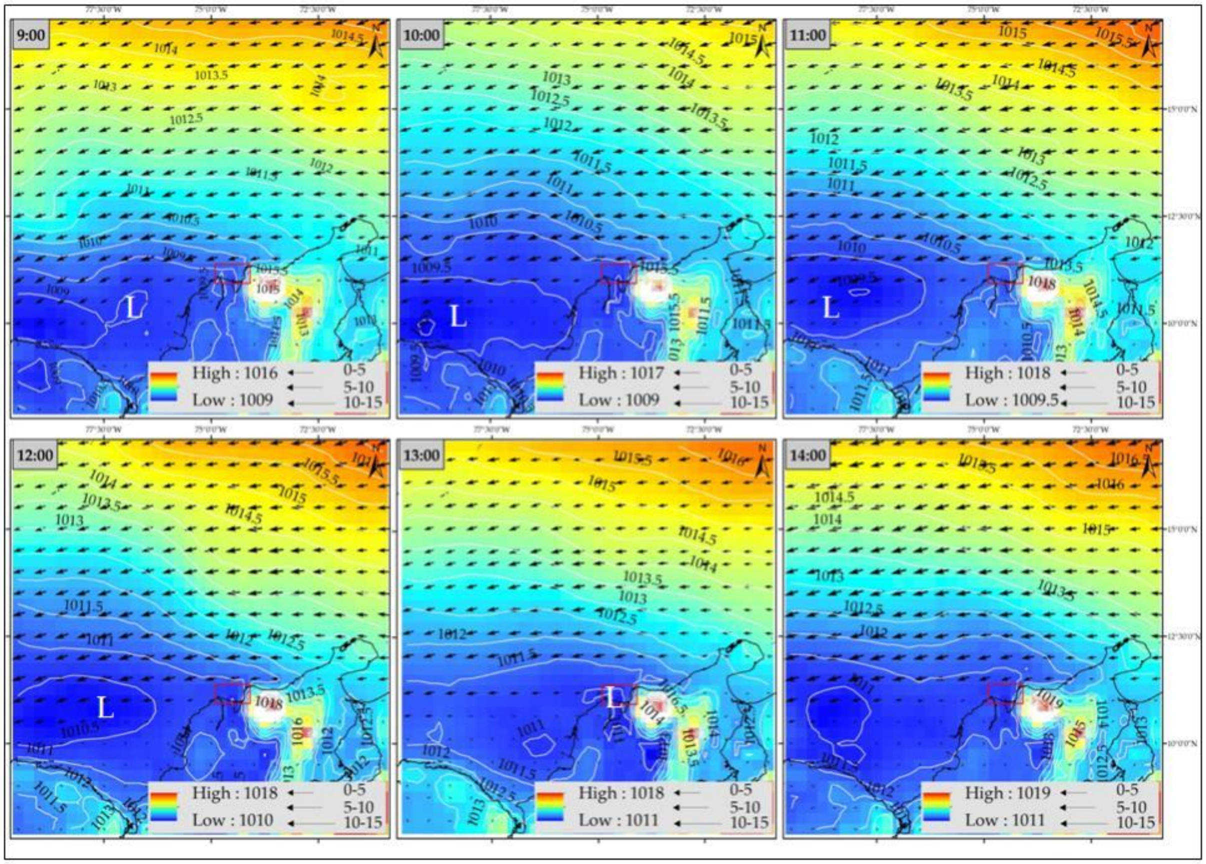

Figure 35. Sea-level atmospheric pressure (hPa) and wind speed and direction between

9:00 and 14:00 on July 19, 2017. Data from the Climate Data Store (CDS) Catalog https//: cds.climate.copernicus.eu/toolbox-editor. Values of minimum pressure (hPa) related to lows are indicated by L. Red rectangle shows the study area.

Similar to average wind conditions at sea level from 1940–2023, easterly winds were predominant at 850 hPa before the event, but speeds decay to a minimum (0–5 m/s) across the Southern Caribbean basin between 12:00 and 13:00 (Figure 36). This decline in the wind speed coincides with a slight increase in humidity and relative humidity from 9:00 to 13:00 (Figure 36 and Appendix 4). Specifically, a northeastward displacement of high levels of humidity was observed from the border between Panama and Colombia towards the Colombian Caribbean coastline. Temperature changes along the day indicated a pattern associated with that of the humidity. Indeed, while specific humidity and relative humidity increased south of the study area, it decreased offshore of the same area (see rectangle in Figure 36 and Appendix 4 for relative humidity values); concurrently, a cooling over the southernmost extreme of the Caribbean Sea occurred between 9:00 and 14:00 (Figure 37).

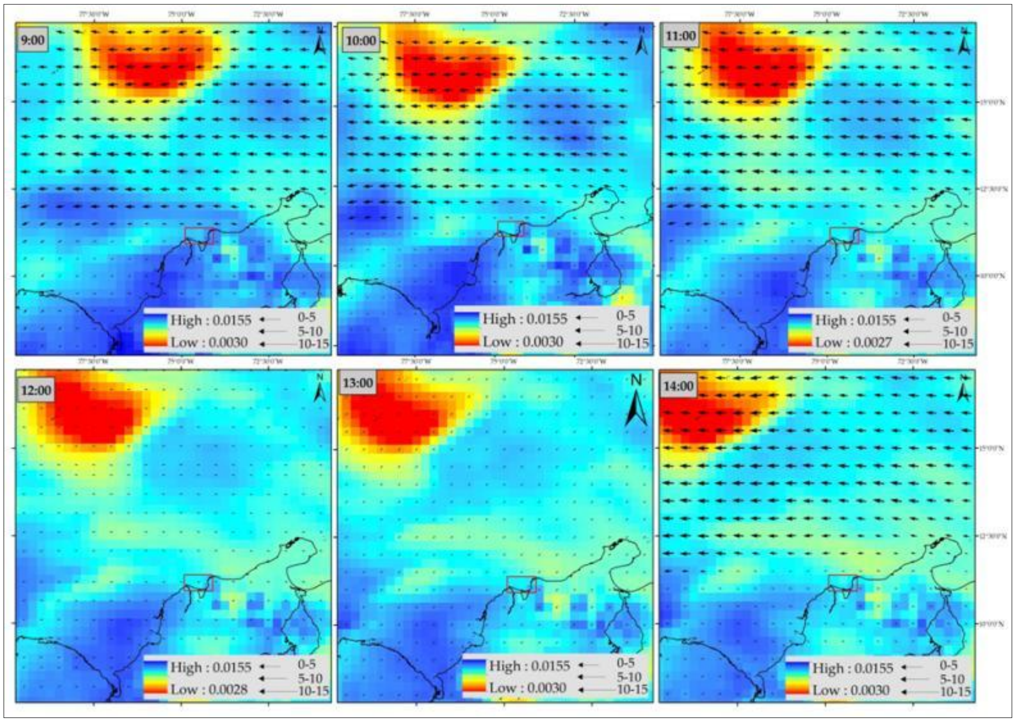

Figure 36. Specific humidity (kg/kg), wind speed (m/s) and direction at 850 hPa from 9:00 to 14:00 on July 19, 2017. Data from the Climate Data Store (CDS) Catalog https//: cds.climate.copernicus.eu/toolbox-editor. Red rectangle shows the study area.

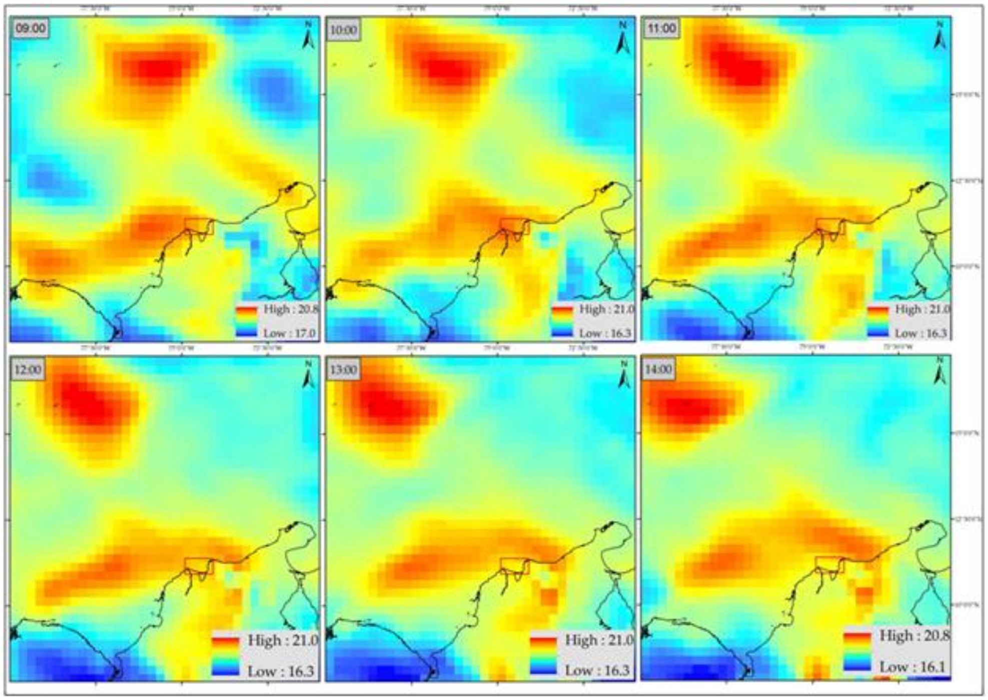

Figure 37. Temperature (°C) at 850 hPa from 9:00 to 14:00 on July 19, 2017.

Data from the Climate Data Store (CDS) Catalog https//: cds.climate.copernicus.eu/toolbox-editor. Red rectangle shows the study area.

Infrared images obtained by the Geostationary Operational Environmental Satellite (GOES-13) satellite reaffirm the findings obtained from the ECMWF reanalysis datasets. The imagery captures a displacement of a cold front mirrored by high concentrations of water vapor (high clouds) and low temperatures. By 13:45, an eastern displacement of the cold front is located westward of the area of interest (red rectangle in Figure 38). A measured of the translation of the leading edge of the front every three hours yields a northward average speed of 9.3 m/s before noon. Subsequently, the speed increased to values of up to 25 m/s before reaching the western border of the study area at approximately 13:00.

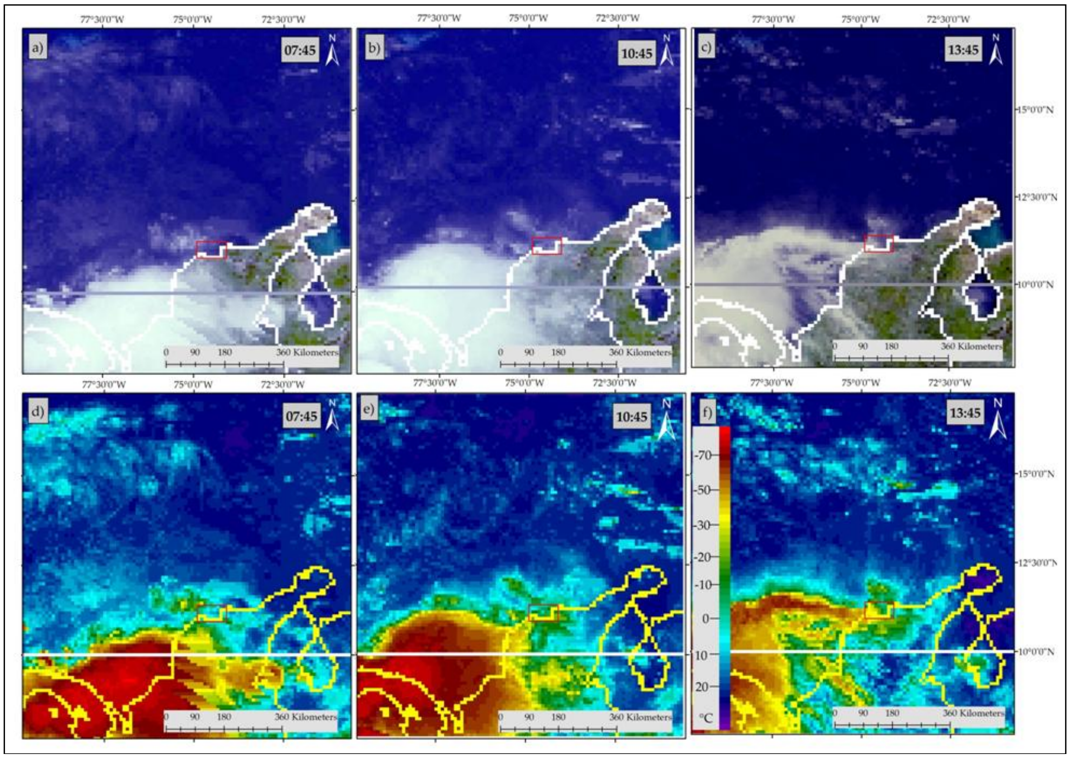

Figure 38. Water vapor and infrared (11μm) image between 7:45 and 13:45 of 19 July,

2017. Thermal emission is used in the lower panel as a proxy of temperature in the upper troposphere. Satellite images from CIMSS/University of Wisconsin in Madison. https://tropic.ssec.wisc.edu/archive. Red rectangle shows the study area (see Appendix 5 for a complete sequence of the displacement of the system during the day of the event).

The movement of the cold front was tracked on a more local scale using onshore meteorological stations. Although it is not possible to detail atmospheric pressure changes using readings taken every hour, the behaviour of stations with changes larger than 1 hPa/hour was highlighted (Appendix 6). Particularly in three of the southernmost stations (El Limón, Turbo, and Puerto Escondido), a jump in the atmospheric pressure was observed between 6:00 and 9:00. For example, in Puerto Escondido (station number 6 in Figure 30), the atmospheric pressure dropped from 1009.8 to 1008.4 hPa between 7:00 and 8:00. Conversely, in Galerazamba (station number 15 in Figure 30), a rise in the atmospheric pressure from 1009.1 to 1011 occurred between 8:00 and 9:00 (Appendix 6).

Measurements at the northernmost stations, consisting of sampling of atmospheric pressure every 2-minutes at the airports in Barranquilla and Riohacha, indicate that when the cold front was approaching the western side of the study site (see snapshots at 10:45 and 13:45 in Figure 38), the atmospheric pressure increased, peaking at 1009.4 hPa (14:38 UTC time) and 1010.2 hPa (13:14 UTC time) in Barranquilla and Riohacha, respectively. This increase in atmospheric pressure was preceded and followed by drops in the pressure values (see blue shades in Figure 39). For instance, maximum rates of change of 1 hPa/hour were observed in Riohacha (15:12 to 16:12), and 0.8 hPa/hour in Barranquilla (Figure 39).

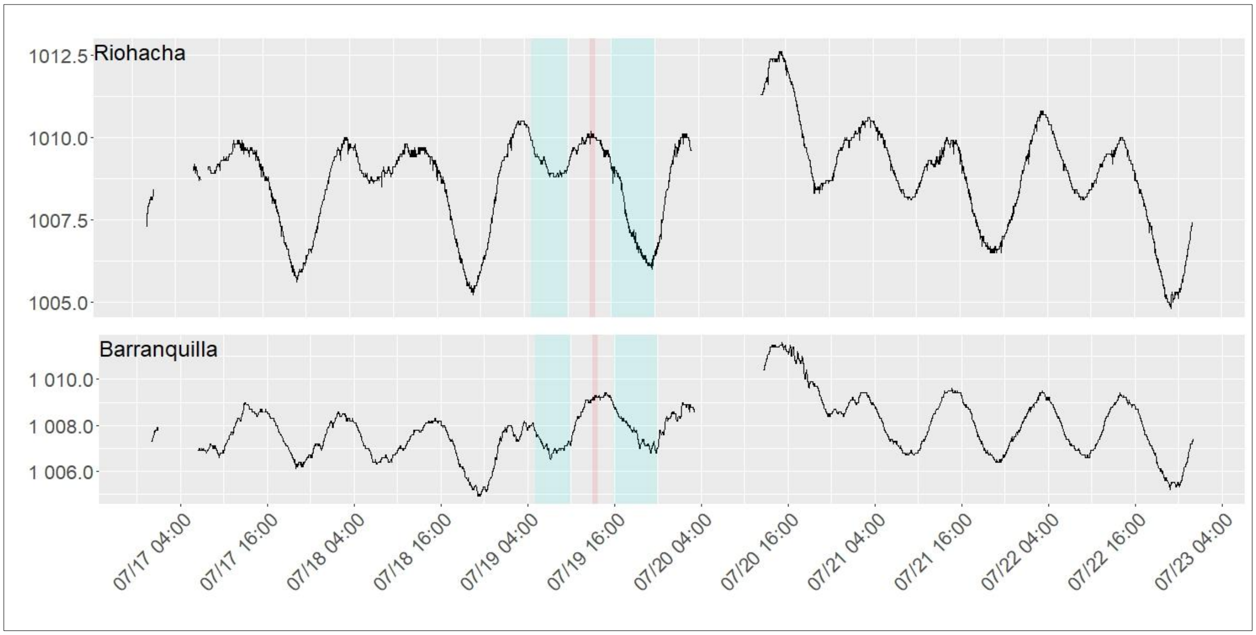

Figure 39. 2-minute atmospheric pressure for July 17–22 in Riohacha (upper panel) and Barranquilla (lower panel). Two atmospheric pressure lows before and after high sea-level variability are highlighted by shaded intervals between 5:00-10:00 and 16:00-22:00. The period of the high sea-level oscillation in Santa Marta (13:00-13:45) is highlighted with a red shade.

In addition to atmospheric pressure fluctuations, winds speeds with gust of up to 11.0 m/s at 17:50 coincide with the drop of atmospheric pressure in Riohacha as well as with a sudden change from easterly to northeasterly wind directions (see Figure 40a/b). Wind direction in Barranquilla has high variability between 10:00 and 16:00 oscillating from southeasterly to southwesterly directions; these frequent changes in wind direction are concurrent with a dropping of the wind speed to less than 3.0 m/s (see area bracketed by blue shade in Figures 40c/d).

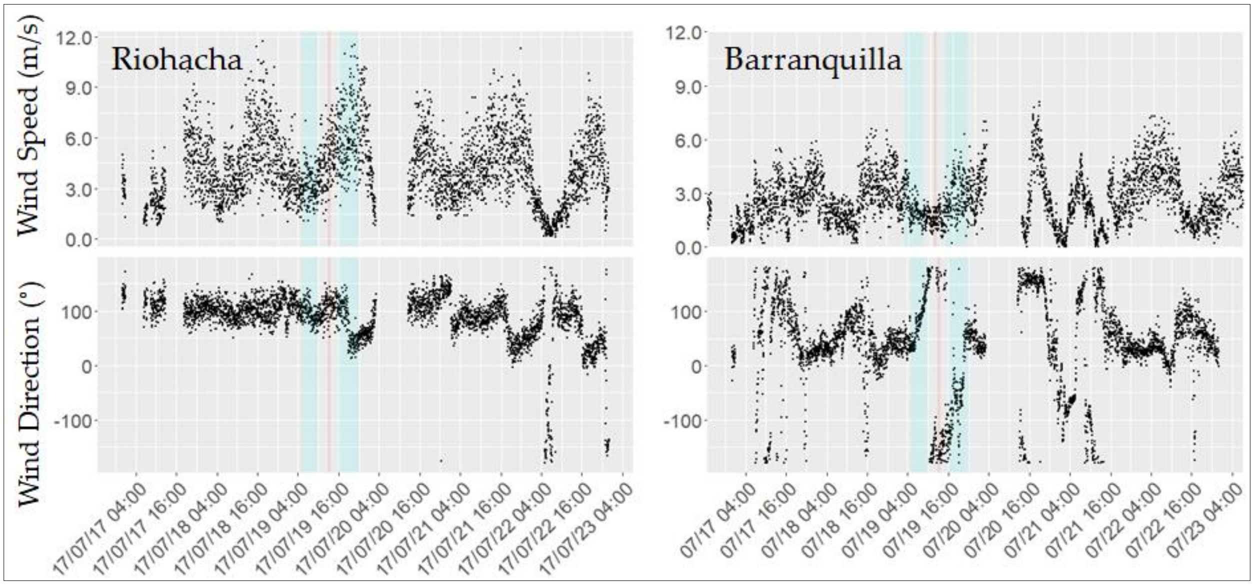

Figure 40. 2-minute wind speed and direction for July 17–23 in Riohacha (left panel) and Barranquilla (right panel). Positive/negative values in wind direction are clockwise/anticlockwise from the North. The period of the high sea-level oscillation in Santa Marta (13:00-13:45) is highlighted with a red shade.

Concomitant with the patterns described above for atmospheric pressure, a decrease in wind speed accompanied by frequent changes in wind direction were observed in Galerazamba between 10:00 and 12:00 (Appendix 7), whereas a similar paucity in wind speed occurred in El Tesoro—85 km southwest from Galerazamba—between 13:00 and 14:10. For this station, wind gusts of up to 6.9 m/s were registered between 14:50 and 15:20 (Appendix 7).

For the second sea-level anomaly detected on the island of San Andrés on 3 September 2017 at 13:50, an analysis of mesoscale atmospheric conditions did not reveal any system prone to create atmospheric instability (Appendix 8). Coupling this potential meteotsunami with data from weather stations on the island was not possible due to lack of station data prior to the event.

4.3.3 Total Water Levels Associated with Storms and Potential Meteotsunami

TWL in Santa Marta for previously described storms (Gómez et al., 2023) and a potential meteotsunami for dissipative and reflective beaches are shown in Table 5. The OWL for a storm that made landfall in the study area during mid-April 2015 as well as the conditions during July 17–21, 2017 are illustrated in Figures 41a/b). In contrast to storms, which usually encompass several tidal cycles, the meteotsunami event only lasted a fraction of an ebb tide (Figure 41b).

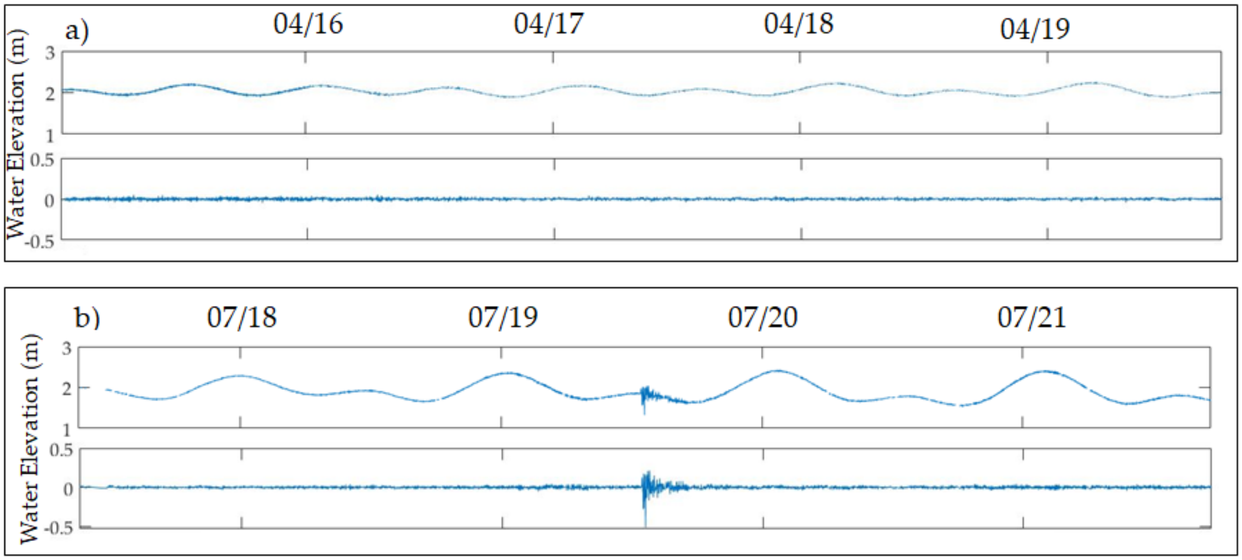

Figure 41. a) Observed water levels (OWL) and non-tidal component of sea level in Santa Marta during storm in mid-April 2015. b) Observed water levels (OWL) and non-tidal component of sea-level in Santa Marta for July 17–21, 2017.

After applying Equation 3 to compare TWL for different beach slopes, it was found that TWL varies between 2.6 m to 5.0 m among the different storms and beach slopes considered (Table 5). Interestingly, the observed water level for the potential meteotsunami falls within that range and is slightly higher than that during the moderate mid-April storm in 2015 (by 0.2 m), though run-up alone is smaller by 0.2 m (Table 5).

Table 5. Observed water level (OWL) and total water level (TWL) for different foreshore angles during selected storms and on July 19, 2017.

	H_0 (m)	**T_0 (sec.)**	**ξ_0**	**Run-up (m)**	**OWL (m)**	**TWL (m)**
Storm mid-April 2015	2.2	6	$0.08^{a}/0.35^{b}/0.80^{c}$	$0.4^{a}/0.8^{b}/1.5^{c}$	2.2	$2.6^{a}/3.0^{b}/3.7^{c}$
Storm end of July 2015	3.2	6	$0.07^{a}/0.29^{b}/0.66^{c}$	$0.9^{a}/1.7^{b}/2.8^{c}$	2.2	$3.1^{a}/3.9^{b}/5.0^{c}$
Storm Feb. 2016	2.4	6	$0.08^{a}/0.33^{b}/0.76^{c}$	$0.8^{a}/1.6^{b}/2.6^{c}$	NA	NA
Meteotsunami July 2017	1.6	6	$0.10^{a}/0.42^{b}/0.94^{c}$	$0.2^{a}/0.4^{b}/1.3^{c}$	2.6	$2.8^{a}/3.0^{b}/3.9^{c}$
Storm mid-July 2018	3.0	5.8	$0.10^{a}/0.42^{b}/0.94^{c}$	$0.8^{a}/1.6^{b}/2.6^{c}$	2.4	$3.2^{a}/4.0^{b}/5.0^{c}$

Values for foreshore slopes of $^{a}1$, $^{b}4°$, and $^{c}9°$.

The role of the event on the coastal morphodynamics is highlighted by imagery taken in the study area on July 18 and 24, 2017. During this time, a new inlet (i.e., lagoon breaching) was formed in the Atascosa lagoon (Figure 42). This inlet was formed westward from an inlet that had previously been breached in April 2016 (Figure 42) (Gómez et al., 2023).

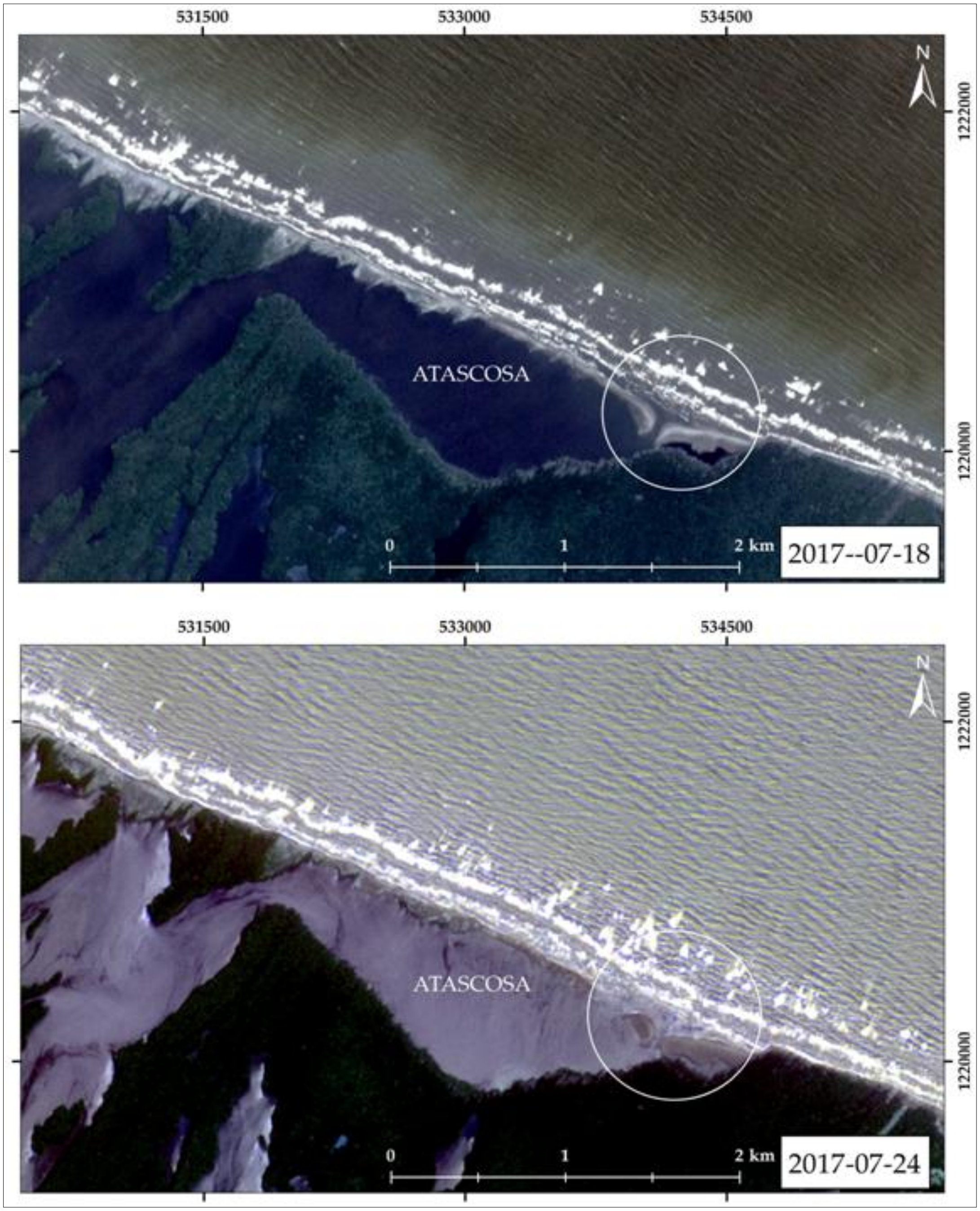

Figure 42. A new inlet is formed in La Atascosa lagoon during July 18–24, 2017 with circle showing the location of the new inlet. Images © 2017 Planet Labs PBC. La Atascosa lagoon is located 18 km east from station number 17 in Figure 30 (see Figure 14 for a regional location of La Atascosa lagoon).

4.4 Discussion

4.4.1 Observational Evidence of a Meteotsunami

Previous reports of cables broken on the sea-bottom due to sediment plumes offshore of the Rio Magdalena mouth (Heezen, 1956) and findings of old landslides offshore of Santa Marta (Vargas and Idárraga-García, 2014) help to understand why a landslide was the first and most widespread assumption to explain the occurrence of the sea-level variability of July 2017. Similarly, Sallenger et al. (1995) described a meteotsunami that had been initially explained as a submarine landslide. Due to the absence of any detection of seismic activity or recent landslide deposits (Cap. Julio Monroy, personal communication, July 2023), coupled with the findings presented in this study, it is most likely that the event of July 2017 was not landslide-induced. Instead, the results provide evidence that the flooding that affected Santa Marta and neighbouring areas was triggered by the influence of an atmospheric disturbance that produced a meteotsunami.

Figure 32 illustrates how the tide gauges captured an increase in observed water level and wave energy around 13:00 (8:00 a.m. local time). In Santa Marta, the largest wave height recorded during the event was 0.6 m. In Cartagena and Ballenas, on the other hand, maximum wave heights by the time of the event were 0.08 and 0.12 m, respectively. These contrasting values point to the large spatial variability of the phenomenon, where small ocean disturbances originating offshore can be strongly intensified in response to specific coastal configurations (e.g., harbours and bays) (Vilibić et al., 2014; Rabinovich, 2020). The results indicate that the sea-level anomaly in Cartagena was synchronous with that of Santa Marta, but without a resonance effect. Similarly, it is likely that the same wave anomaly that affected Santa Marta around 13:00 was registered in the northernmost tide gauge of Ballenas five hours after (Figure 32c).

Monthly averaged values of temperature, wind, atmospheric pressure, and humidity for July (1940–2023) (Figure 34) indicated that the conditions on 19 July 2017 (Figures 35-37) were unlike average values for July. Indeed, despite wind and sea-surface atmospheric pressure values resembling expected conditions during the day of the event (e.g., westward-southwestward winds and a general trend of southwestward decreasing of atmospheric pressure along the Southern Caribbean basin), the northward movement of a system with a high content of water vapour that met dry and warm air over the ocean produced anomalous variability in temperature and humidity during the morning and early afternoon of July 19 (Figures 35–37).

For comparison to other meteotsunamis, similar conditions preceded the Daytona meteotsunami on July 3, 1992, wherein a southward moving mesoscale convective system with extensive cloudiness migrated from South Carolina and Georgia towards Florida (Churchill et al., 1995). Whereas the system moving over the Caribbean in July 2017 reached speeds of up to 25 m/s before 13:00, the reported speeds for the system that affected Daytona in July 1993 were between 13 and 14 m/s (Churchill et al., 1995; Sallenger et al., 1995). In contrast, Arctic cold fronts recognized by generating wave oscillations in the port of Rotterdam need to move at speeds of approximately 17 m/s to produce convection cells capable of triggering resonance in depths of approximately 30 m (de Jong and Battjes, 2004).

Usually, meteotsunamis are initiated by a travelling atmospheric disturbance within the lower troposphere that is detected by abrupt changes in surface air-pressure series (Monserrat et al., 2006; Vilibić et al., 2014). As a case in point, a meteotsunami that affected the island of Hvar (Croatia) in the Adriatic Sea on June 25, 2014 was accompanied by air pressure changes of up to 1.5 hPa during a 5-minute period (Šepić et al., 2015). For the day of the event, despite some closed low-pressure systems observed in the reanalysis data for the Southern Caribbean basin (e.g., see conditions at 13:00 in Figure 35), subtle and short-lived changes of air-pressure that occur within an hour span or in areas smaller than the spatial resolution (approximately 30 km) were not captured by the reanalysis models. On a more local scale, air-pressure sampled every 2 minutes at the meteorological stations of Barranquilla and Riohacha showed an oscillating trend between 05:00 and 22:00 in July 19 (Figure 39), but the short-term (<5 min.) rate of change is not large enough at any point of the day to reflect those expected during meteotsunamis.

Despite hourly readings of sea-level pressure included in this work preclude the assertion of any causal relationship with a potential meteotsunami, the fluctuations observed during the morning of 19 July 2017 are indicative of the influence of an air pressure disturbance in the area (Figure 39 and Appendix 6). In addition, wind readings every 10-minutes in the stations of Galerazamba and El Tesoro indicated a sudden decrease in wind speed punctuated by gusts of up to 7 m/s before noon during the day of the event (Appendix 7). De Jong and Battjes (2004), when investigating the atmospheric origin of low-frequency sea-waves that impact the port of Rotterdam, observed that oscillatory wind speeds are due to convection cells in the lower troposphere formed behind a cold front, where cold air moves over the relatively warm ocean surface resulting in temperature gradients larger than 15 °C/km in the lower troposphere. The availability of a radiosonde that enables to obtain vertical atmospheric profiling at any of the airports on the Colombian Caribbean would have allowed confirming atmospheric instability mirrored by steep gradients in temperature and humidity.

The passage of a cold front over the Colombian Caribbean is portrayed by colour-enhanced infrared images (Figure 38 and Appendix 5) and also reflected by some onshore meteorological stations (Appendixes 3 and 7). As the system moved over the ocean northward from Galerazamba (station 15, Figure 30), the stations located north of this station (i.e., N 10.795°/W 75.257°) did not show the atmospheric pressure oscillations observed in their southernmost pairs. At around noon, the aforementioned system, which originated in the interior of Colombia and the Pacific Ocean (Figure 38 and Appendix 5), met a dry air system located west and offshore from the area of interest (Figures 36–37). It is suggested that contrasting values in temperature and relative humidity between the cold front and the dry mass forced convection in the troposphere, resulting in a squall line that formed in the ocean with its easternmost extreme bordering the area of interest (Figure 38 and Appendix 5). Wave heights of up to 0.6 m registered in Santa Marta after 12:53 were likely amplified by a resonance mechanism over the narrow shelf offshore of Cartagena and Barranquilla; however, understanding the resonance mechanisms that enabled the amplification of the waves requires a local atmospheric dataset that includes not only onshore high-temporal resolution for wind and atmospheric pressure measurements, but also offshore weather stations measuring the same variables.

Accordingly, even though a full understanding of the mechanisms that triggered and amplified the wave anomaly in July 2017 requires a high-resolution local atmospheric dataset that remains unavailable, it is suggested that among the two hypotheses to explain the event, the occurrence of a meteotsunami appears most probable.

4.4.2 Linking atmospheric-induced sea-level oscillations and coastal morphodynamics

Regardless of its origin, the event of 19 July 2017 provides an opportunity to explore how the processes of erosion and flooding impact the study area during high episodic sea levels. Data on OWL from tide gauges is influenced by local station conditions, such as if the gauge is not far enough from the coastline to avoid the effect of wave shoaling. In this instance, tide gauge measurements might include a fraction of the run-up value (Dean et al., 2005). As for the Santa Marta tidal station (65 m offshore and approximately 3.5 m in depth), the OWL could include some overestimation of the true value. Despite this potential for overestimation, comparisons of TWL for storms and meteotsunami at the same location (i.e., using the same gauge) are suitable (see Table 5).

Using the tide gauge in Santa Marta, it was observed that TWL for the meteotsunami and moderate storms are alike (Table 5). Additionally, meteotsunamis and storms share a similar impact as drivers of morphological changes. In fact, although the 10-year time series of tide readings point out that meteotsunamis have a much lower recurrence than storms in the Southern Caribbean Sea (i.e., one meteotsunami event in a record of 10 years), a breaching detected in La Atascosa lagoon between July 18–24, 2017 suggests that both phenomena are capable of leading to a breach and lasting coastal change (Figure 42). Previous research has shown that the overall result of the successive breachings and healings of coastal lagoons in the study area is a net coastline retreat in conjunction with areal change in the lagoons (Gómez et al., 2023).

Unlike storms, which can superimpose their effect on the different phases of the tidal cycle over periods ranging from days to weeks, short-lived meteotsunamis usually only overlap a fraction of a single tidal cycle (Figure 41). Nonetheless, as reported for other locations with microtidal regimes affected by sea-level oscillations due to meteotsunamis (e.g., Vučetić et al., 2009; Vilibić et al., 2021a), even crest-to-trough wave heights of 0.20 m amount to a large proportion of the total tide range.

When strong storms (H ≥ 3.0 m) occur in conjunction with beach-face slopes larger than 9°, run-up accounted for a large proportion of the TWL. Conversely, during the meteotsunami event, OWL accounted for ≥50% of the TWL. In fact, despite the wave height measured in the buoy being smaller than for any of the storms (i.e., H=1.6 m), the OWL was larger than for all of the storms. As reported elsewhere (e.g., Asano et al., 2012), internal resonance associated with the local bathymetry and morphology of the sea bed likely played a key role in the nearshore amplification of the wave height during the 19 July 2017 event. The sea-level oscillation shown in Figure 32a occurred after the peak of a mid-tide, but had it coincided with the peak of the maximum high tide, the flooding of Santa Marta and other nearby settlements would have been exacerbated. Accordingly, values of water levels during storms and meteotsunamis must be included for extreme sea-level predictions, coastal planning, and the design of future policies of coastal management.

4.5 CONCLUSIONS

Analysis of sea-level readings from three tide gauges in the Southern Caribbean for the period 2013–2022 found only one tsunami-like wave oscillation in a station located in Santa Marta, Colombia on 19 July 2017. A detailed analysis of the conditions that triggered this event suggests that it was atmospherically induced. Specifically, a cold front coming from the Pacific Ocean and interior of Colombia translated over the Caribbean Sea where it met and moved over a dry and warm system, resulting in extensive convection in the troposphere. Although the specific mechanisms that amplified the wave height are not established in this project, unstable atmospheric conditions reflected by a paucity in the wind speed as well as sporadic wind bursts before the event, large changes in the atmospheric pressure in some of the onshore stations, and contrasting temperatures between the ocean and continental front, point to the conclusion that the event was atmospherically-induced and as a consequence, within the definition of a meteotsunami. Total water levels related to the meteotsunami are similar to those produced by moderate storms and both phenomena can induce coastal flooding and breachings. Nonetheless, because the frequency of meteotsunamis is overshadowed by that of storms, the role of the latter as forcer of coastal change is greater.

Chapter 5. Conclusions

This dissertation aimed to better understand the role that a range of geomorphic forcers acting at different temporal scales have had in the morphodynamics of a deltaic barrier during the last 50 years. To achieve this overarching goal, I combined wave simulations, reanalysis, radar and satellite data, and information gathered at meteorology stations. Causality on coastal landscape changes was established by coupling the response in the landscape—as captured by periodic satellite images—with the dynamic nature of the forcing of winds, waves, river discharge, precipitation, atmospheric pressure and vertical land motions (VLM). These variables encompass instantaneous, short and medium temporal scales, and their impact over the landscape depend not only on their magnitude and frequency, but also on the morphology of the terrain. Aside from VLM, the aforementioned climate variables are modulated by global climatic oscillations operating at annual (e.g., ITCZ), and interannual scales (e.g., ENSO).

As having a suitable time series of data as well as a baseline to assess and compare the influence of human activities within the study area was not possible, anthropogenic actions were not directly assessed in this research as an explanatory variable. Clearly, the construction of the roadway between Barranquilla and Santa Marta, added to the engineering of the Magdalena River mouth, are the most recently and largest developments affecting the barrier (Gómez et al., 2016).

Four objectives were addressed throughout this dissertation. Below, the findings for each of these objectives are synthesised, followed by some of the methodological challenges of this dissertation, and future directions for research.

Objective 1. Establish the role that vertical land motion (VLM) has played in the evolution of the coastal area and to relate the findings to historic coastal changes.

The assessment of VLM was addressed using interferometric synthetic aperture radar dating back to 2007. The findings revealed that subsidence is not a widespread phenomenon in the study area but is, rather, mainly localized to areas of former mangrove forest, where subsidence rates of up to –1 cm/yr were measured. Accordingly, subsidence is not a necessary condition for coastal erosion to occur.

It is suggested that, after the decaying of the mangrove population as a consequence of the construction of the road between Barranquilla and Santa Marta in the 1950s, subsidence rates were increased by sediment compaction of the Holocene alluvium and gas emission followed by oxidation from organic-rich soils. Thus, high subsidence in areas where mangrove trees were abundant is, at its root, caused by the anthropogenic alteration of the wetland.

Even though the study area was fully covered by the ascending and descending tracks of Sentinel 1A/B data, the coherence of the signal did not always surpass the minimum coherence threshold (0.65), resulting in areas without any VLM data (Figures 7–8). This drawback in the approach is difficult to overcome as it is the result of the changing nature of the vegetation coverage and the absence of features with high coherence levels such as buildings. However, signals obtained in key areas close to the coastline (e.g., between km 20th and Cuatro Bocas lagoon) provided a broad picture of the VLM trends.

By the end of this century, current values of subsidence of approximately 1.0 cm/yr will translate into isostatic SLR values that are the same order of magnitude as conservative projections of global SLR (e.g., projections assessed by Church et al., 2013). Moreover, the longest tide gauge record nearby the study area, located in Cartagena, indicates a sea-level rise of 5.3 mm/yr between 1950 and 2010 (Andrade et al., 2013). The time for a barrier to drown depends on the interplay of multiple variables; nonetheless, for moderate SLR (e.g., 3 mm/yr), Ashton and Lorenzo-Trueba (2018) noted that the time to drowning of modeled barriers is in the order of hundreds of years. Accordingly, considering historic trends and projections of eustatic and isostatic SLR values is relevant for the planning and designing of a proposed expansion to the road that connects Barranquilla and Santa Marta.

Objective 2. Evaluate the forcing mechanisms that favour lagoon breaching and healing in a microtidal environment.

Short-term drivers of coastal morphodynamics were assessed by using four lagoons located along the back-barrier to better understand the interplay between extreme events and the breaching and healing of inlets that are temporarily formed between the lagoons and the ocean. Satellite data in conjunction with hourly readings from reanalysis and weather stations spanning the past 50 years helped to find the conditions that enabled the breaching and healing processes to transpire in the lagoons. The variables included in the analysis of short-term drivers of coastal morphodynamics were river discharge, wind, wave height and period, precipitation, and atmospheric pressure. After the analysis, it was found that breachings of lagoons are mainly induced by storms and less frequently, by extreme flows in the Magdalena River.

To overcome the lack of coastal monitoring programs in the study area, the methodological approach was conceived using a landform (lagoon) that was not only easily detected from satellite images, but that allowed capture of the geomorphic response to extreme events by taking advantage of the inherent spectral differences between the barrier and water. Initial attempts to develop the analysis of the relationship of the independent and response variable (i.e., lagoon breachings) using principal component analysis or general additive models were hindered by the limited number of breachings dateable to a 3 week period (n=13), the large number of gaps in the Landsat dataset—particularly during the 1980s and 1990s—and a large number of images with poor surface reflectance due to cloudy conditions. This work is therefore a small, rather than exhaustive, sample of breachings from 1973 to 2020.

Aligned with the predominantly erosive regime along the study area, the findings indicated that the cumulative effect of the breaching and healing of the lagoons resulted in a deltaic barrier that has rolled over the lagoons. To illustrate the intertwined nature of the meteorological variables mentioned above, the influence of ENSO in fluvial input from the Magdalena River to the study area is highlighted. Particularly, extremely rainy years associated with La Niña events make the lagoons prone to washouts due to high discharge values of the Magdalena River. Precipitation, however, is a variable that the findings revealed is not critical at a local level for the breaching of lagoons.

As morphology and width vary along the barrier, in part as a result of the different rates of coastline accretion and erosion over time (Figure 18b and Figure 27), the geomorphic response to washouts or to any other extreme event is not uniform along the barrier. Similarly, cross-shore variability over time can result in different responses to similar events across a specific spot on the barrier. Barrier width plays an important role in the response to extreme events, with there being a threshold width below which breaching occurs as a response. In the study area, wider barrier segments are associated with downdrift/accretive regimes and thinner barriers with updrift/erosive regimes.

Once a larger dataset of imagery becomes available (for example, using high spatial and temporal resolution imagery provided by Planet), it is worth further exploring statistical approaches that relate the response on the coastal landscape to independent variables. Nonetheless, the results using the DBM method provided unambiguous results of the forcing mechanisms of lagoon breaching and healing.

Objective 3. Investigate the role of meteotsunamis as an external forcing of coastal morphodynamics and provide insights of the conditions that enable meteotsunamis to transpire in the Colombian Caribbean.

The occurrence of meteotsunamis in the Colombian Caribbean, an instantaneous driver of coastal morphodynamics, was investigated using a wavelet analysis applied to water-level readings obtained from three tide gauges. These tide gauges, located in Colombia and Panama, have been collecting data in the southern area of the Caribbean Sea over the period 2013–2022. After the discovery of one event with meteotsunami-like characteristics, the atmospheric conditions and total water levels associated with this event were analyzed. Flooding and a sudden sea-level oscillation associated with this event were reported in various coastal towns located between the southwest of Barranquilla and Santa Marta, encompassing approximately 132 km of the coastline.

As part of the investigation to explore potential triggers of the phenomenon, meteorological and seismological data were gathered prior and during the day of the event. For the latter, no records of earthquakes were registered in seismological catalogs, rendering unlikely the hypothesis that the sudden water-level oscillation was caused by an earthquake. An analysis of data from onshore meteorological stations in the Southern Caribbean coast showed oscillations in the values of sea-level pressure and wind velocity and direction, but the data available were not conclusive to link that variability to the sudden water-level oscillation.

At the regional scale, the analysis included imagery from the stationary satellite GOES-13 and reanalysis data from ECMWF models (Figures 34–38). Despite the finer resolution of ECMWF with respect to other reanalysis models (e.g., NOAA), the resolution is not fine enough to capture the localized and short-lived changes of atmospheric pressure that commonly trigger meteotsunamis. Nevertheless, analysis of the data indicated that, prior to the event, a cold humid system moved northward over the relatively warm waters of the Caribbean Sea. It is suggested that the contrasting values in humidity and temperature resulting from the cold front passing over the relatively warmer sea surface induced the initial conditions (e.g., atmospheric instability and lower convection) that gave place to the meteotsunami. Identifying the processes that amplified the wave heights through a resonance effect was hindered by the lack of meteorological stations with high temporal resolution and vertical atmospheric soundings in the area of influence of the meteotsunami. As the frequency of meteotsunamis is overshadowed by that of storms, and water levels produced by the event were comparable to those produced by moderate storms, it is considered that an investment in additional stations should not be a public priority at the moment. Instead, limited resources should be allocated to keeping the existing stations fully operational (i.e., no gaps in data), and to increasing the rate of atmospheric pressure sampling at the airport of Santa Marta from readings every hour to every minute. Along these same lines, tide gauge stations in Santa Marta, San Andrés, Ballenas and Cartagena (Figure 30 for location of tide gauges) need to be regularly maintained to guarantee the reliability of their data.

Objective 4. Provide feasible alternative methodological approaches to track coastline morphodynamics in areas with limited pre-existing information and lack of ongoing monitoring programs.

Data from oceanographic and coastal environments, including data taken from wave buoys, tide gauges and some of the meteorological stations in proximity to the coastline, are administered by DIMAR, a branch of the Colombian Navy. Efforts are currently made by the institution to facilitate accessibility to information using their web page (https://cecoldo.dimar.mil.co/web), but for access to high temporal resolution data (≤ 1 hour), it is still necessary to make a formal request before a permission to download the data is granted. In addition, metadata are rarely provided and gaps in the time series are common. As a means to overcome the limitations associated with data availability, my research relied on a combination of the limited observational data with reanalysis and wave simulations. In addition, processing of radar (Alos-Palsar and Sentinel) and satellite data (Landsat and Planet imagery) supported the assessment of VLM and changes to the coastline and lagoons over time.

The information from these multiple sources provided the explanatory variables that, among others, have contributed to driving the geomorphic changes in the deltaic barrier of the Magdalena River for 1973–2020. It is considered that the methods followed in this research are a reliable approach to better understand the short- and medium-term drivers of coastal morphodynamics and are feasible to be replicated in other areas with limited data availability.

5.1 Future Work

If enough resources are allocated, there are multiple opportunities to further explore the processes analyzed in this research through establishing either continuous monitoring programs or visiting the study area as needed during specific events (e.g., during storms, meteotsunamis, washouts). Three universities with faculty involved in researching coastal environments and a government-funded marine-research centre located within a short driving distance from the park (<100 km) offer ideal conditions to build partnerships with the park managers and grassroots organizations in Ciénaga, Pueblo Viejo, and Tasajera.

After establishing the characteristics of some of the drivers of coastal morphodynamics, several gaps in knowledge persist. In fact, little is known about the amounts of sediment mobilized across and along the deltaic barrier. The paragraphs that follow provide some general approaches to fill this gap in knowledge.

This research strongly relied on satellite and meteorological data; however, future work will benefit from a stronger field component to gather seasonal topographic data. Periodic surveys of the morphology of the terrain—using, for example UAV or terrestrial laser scanners—will enable researchers to narrow down the critical distances and minimum barrier heights for the occurrence of overwashes and lagoon breachings. Moreover, high resolution digital elevations models will allow for more accurate tracing of the coastline along the MHWL as determined by tidal conditions.

Additionally, assessing the rates of sediment transport across the barrier, particularly during overwashes and breachings, will help researchers to better understand the onshore-offshore dynamics and volume of sediments transported during extreme events (e.g., storms, washouts) and healing of lagoons. Sherwood et al. (2014) provide details of modelling and field devices used to quantify water-level gradients and sand transport across a barrier during storms. In the study area, as the occurrence of washouts is closely related to the stage of the Magdalena River, identifying the contribution of the seaward transport of sediment through inlets originated by washouts can shed light on the relevance of sporadic campaigns led by park staff to clean some of the former waterways connecting the Magdalena River to the coastline.

Aiming to get insights into the relationship between subaerial and submarine elevation changes, an additional step includes coupling onshore topographic and bathymetric data. However, high waves and a lack of piers in the area make nearshore bathymetry measurements challenging. Alternatively, using unmanned underwater vehicles can lessen the operational navigation difficulties. Along these same lines, little is known about the volumes and seasonality of alongshore sediment transport and how it is modulated by the interplay of shoreline orientation and wave angle along the coastline.

After taking some sediment cores inside the Cuatro Bocas and Manatíes lagoons in 2019, it was attempted to quantify sedimentation rates inside the lagoons using a dating method (^{210}Pb). Nonetheless, bioturbation along the sediment core and/or abrupt changes in the sedimentation rates rendered the results of the dating questionable. Hence, a lesson learned from the sediment sampling is that even sheltered areas inside the large lagoons are prone to disruptions in the sedimentation rates; it is, therefore, advisable that future sediment coring to quantify sedimentation rates considers sampling inside small and less active (e.g., without the effect of breachings) lagoons such as Ciénaga del Medio or Salinas (see Figure 14 for location of lagoons).

In conjunction with numerical models, observational research offers tools for better understanding barriers response to atmospheric, oceanographic and vertical land motion forcing. Beyond providing specificities about the drivers of coastal morphodynamics at a local level, the findings of this dissertation provide research-based data to support science-based management of deltaic barriers elsewhere facing sea-level rise and a reduction of sediment supply due to human activities.

Chapter 6. References

Aagaard, T., Kroon, A., 2019. Decadal behaviour of a washover fan, Skallingen Denmark. Earth Surf. Process. Landforms esp.4610. https://doi.org/10.1002/esp.4610

Amato, V., Aucelli, P.P.C., Corrado, G., Di Paola, G., Matano, F., Pappone, G., Schiattarella, M., 2020. Comparing geological and Persistent Scatterer Interferometry data of the Sele River coastal plain, southern Italy: Implications for recent subsidence trends. Geomorphology 351, 106953. https://doi.org/10.1016/j.geomorph.2019.106953

Andrade, C.A., Thomas, Y.F., Lerma, A.N., Durand, P., Anselme, B., 2013. Coastal Flooding Hazard Related to Swell Events in Cartagena de Indias, Colombia. coas 29, 1126–1137. https://doi.org/10.2112/JCOASTRES-D-12-00028.1

Anthony, E.J., Brunier, G., Besset, M., Goichot, M., Dussouillez, P., Nguyen, V.L., 2015. Linking rapid erosion of the Mekong River delta to human activities. Sci Rep 5, 14745. https://doi.org/10.1038/srep14745

Appendini, C.M., Urbano-Latorre, C.P., Figueroa, B., Dagua-Paz, C.J., Torres-Freyermuth, A., Salles, P., 2015. Wave energy potential assessment in the Caribbean Low Level Jet using wave hindcast information. Applied Energy 137, 375–384. https://doi.org/10.1016/j.apenergy.2014.10.038

Asano, T., Yamashiro, T., Nishimura, N., 2012. Field observations of meteotsunami locally called "abiki" in Urauchi Bay, Kami-Koshiki Island, Japan. Nat Hazards 64, 1685–1706. https://doi.org/10.1007/s11069-012-0330-2

Ashton, A.D., Lorenzo-Trueba, J., 2018. Morphodynamcis of Barrier Response to Sea-Level Rise, in: Moore, L.J., Murray, A.B. (Eds.), Barrier Dynamics and Response to Changing. Springer, Cham, Switzerland, pp. 277–304.

Aubrey, D.G., Speer, P.E., 1984. Uprdrift migration of tidal inlets. Journal of Geology 92, 531–545.

Bailey, L.P., Clare, M.A., Rosenberger, K.J., Cartigny, M.J.B., Talling, P.J., Paull, C.K., Gwiazda, R., Parsons, D.R., Simmons, S.M., Xu, J., Haigh, I.D., Maier, K.L., McGann, M., Lundsten, E., 2021. Preconditioning by sediment accumulation can produce powerful turbidity currents without major external triggers. Earth and Planetary Science Letters 562, 116845. https://doi.org/10.1016/j.epsl.2021.116845

Battjes, J.A., 1974. Surf Similarity, in: ASCE. Presented at the Proceedings of the 14th Conference of Coastal Engineering, The Netherlands, pp. 466–480.

Bernal. G., 1996. Caracterización geomorfológica de la llanura deltáica del río Magdalena con énfasis en el sistema lagunar de la Ciénaga Grande de Santa Marta, Colombia. Boletín de Investigaciones Marinas y Costeras Invemar 25, 19–48.

Bernal, G., Osorio, A.F., Urrego, L., Peláez, D., Molina, E., Zea, S., Montoya, R.D., Villegas, N., 2016. Occurrence of energetic extreme oceanic events in the Colombian Caribbean coasts and some approaches to assess their impact on ecosystems. Journal of Marine Systems 164, 85–100. https://doi.org/10.1016/j.jmarsys.2016.08.007

Bianchi, T., 2016. Deltas and humans. A Long relationship now threatened by global change. Oxford University Press, New York.

Blackwell, E., Shirzaei, M., Ojha, C., Werth, S., 2020. Tracking California's sinking coast from space: Implications for relative sea-level rise. Sci. Adv. 6, eaba4551. https://doi.org/10.1126/sciadv.aba4551

Boak, E.H., Turner, I.L., 2005. Shoreline Definition and Detection: A Review. Journal of Coastal Research 214, 688–703. https://doi.org/10.2112/03-0071.1

Carvajal, M., Contreras-López, M., Winckler, P., Sepúlveda, I., 2017. Meteotsunamis Occurring Along the Southwest Coast of South America During an Intense Storm. Pure Appl. Geophys. 174, 3313–3323. https://doi.org/10.1007/s00024-017-1584-0

Catuneanu, O., 2006. Principles of sequence stratigraphy. Elsevier, Italy.

Church, J.A., Clark, P.U., Cazenave, A., Gregory, J.M., Jevrejeva, S., Leverman, A., Merrifield, M.A., Milne, G.A., Nerem, R.S., Nunn, P.D., Payne, A.J., Pfeffer, W.T., Stammer, D., Unnikrishnan, A.S., Bex, V., Midgley, P.M., 2013. Sea level change, in: Stocker, T.F., Oin, D., Plattner, G.K., Tignor, M., Allen, S.K., Boschung, J., Nauels, A., Xia, Y. (Eds.), Climate Change 2013: Contribution of Working Group I to the Fifth Assessment Report of the Intergovernmental Panel on Climate Change. Cambridge University Press, Cambridge.

Churchill, D.D., Houston, S.H., Bond, N.A., 1995. The Daytona Beach Wave of 3-4 July 1992: a shallow-water gravity wave forced by a propagating squall line. Bulletin of the American Meteorological Society 76, 21–32.

Colmenares, P., Mesa, M., Roncancio, J., Pedraza, P., Contreras, A., Cardona, A., Silva, C., Romero, J., Alvarado, S., Romero, O., Vargas, F., Santamaría, F., 2007. Geología de la plancha 18.

Conery, I., Walsh, J.P., Reide Corbett, D., 2018. Hurricane Overwash and Decadal-Scale Evolution of a Narrowing Barrier Island, Ocracoke Island, NC. Estuaries and Coasts 41, 1626–1642. https://doi.org/10.1007/s12237-018-0374-y

Cooper, J.A.G., Green, A.N., Meireles, R.P., Klein, A.H.F., Souza, J., Toldo, E.E., 2016. Sandy barrier overstepping and preservation linked to rapid sea level rise and geological setting. Marine Geology 382, 80–91. https://doi.org/10.1016/j.margeo.2016.10.003

Cooper, J.A.G., Green, A.N., Loureiro, C., 2018. Geological constraints on mesoscale coastal barrier behaviour. Global and Planetary Change 168, 15–34. https://doi.org/10.1016/j.gloplacha.2018.06.006

Cowell, P.J., Kinsela, M.A., 2018. Shoreface Controls on Barrier Evolution and Shoreline Change, in: Moore, L.J., Murray, A.B. (Eds.), Barrier Dynamics and Response to Changing Climate. Springer International Publishing, Cham, pp. 243–275. https://doi.org/10.1007/978-3-319-68086-6_8

Cueto, J.E., Otero Díaz, L.J., Ospino-Ortiz, S.R., Torres-Freyermuth, A., 2022. The role of morphodynamics in predicting coastal flooding from storms on a dissipative beach with sea level rise conditions. Nat. Hazards Earth Syst. Sci. 22, 713–728. https://doi.org/10.5194/nhess-22-713-2022

Davidson-Arnott, R., 2010. Introduction to coastal processes and geomorphology, 1st ed. Cambridge University Press, Cambridge.

Davies-Vollum, K.S., Zhang, Z., Agyekumhene, A., 2019. Impacts of lagoon opening and implications for coastal management: case study from Muni-Pomadze lagoon, Ghana. J Coast Conserv 23, 293–301. https://doi.org/10.1007/s11852-018-0658-1

De Jong, M.P.C., Battjes, J.A., 2004. Low-frequency sea waves generated by atmospheric convection cells. J. Geophys. Res. 109, C01011. https://doi.org/10.1029/2003JC001931

Dean, B., Collins, I., Divoky, D., Hatheway, D., Scheffner, N., 2005. Wave Setup (Focused Study Report). Federal Emergency Management Agency.

Del Río, L., Gracia, F.J., 2013. Error determination in the photogrammetric assessment of shoreline changes. Nat Hazards 65, 2385–2397. https://doi.org/10.1007/s11069-012-0407-y

Di Paola, G., Alberico, I., Aucelli, P.P.C., Matano, F., Rizzo, A., Vilardo, G., 2018. Coastal subsidence detected by Synthetic Aperture Radar interferometry and its effects coupled with future sea-level rise: the case of the Sele Plain (Southern Italy). J Flood Risk Management 11, 191–206. https://doi.org/10.1111/jfr3.12308

Dillenburg, S.R., Barboza, E.G., 2009. Long-and Short-term Progradation of a Regressive Barrier in Southern Brazil. Journal of Coastal Research 56, 599–601.

Dixon, T., Amelung, F., Ferrerett, F.N., Rocca, F., Dokka, R., Sella, G., Kim, S., Wdowinski, S., Whitman, D., 2006. Subsidence and flooding in New Orleans. Nature 441, 587–588. https://doi.org/doi.org/10.1038/441587a

Dixon, T. Dokka, R. 2008. Earth Scientists and Public Policy: Have We Failed New Orleans? Eos, Transactions American Geophysical Union 89, 96–97.

Dokka, R.K., 2006. Modern-day tectonic subsidence in coastal Louisiana. Geol 34, 281. https://doi.org/10.1130/G22264.1

Dolan, Hayden, P., May, P., May, S., 1980. The reliability of shoreline change measurements from aerial photographs. Shore & Beach 48, 42–49.

Domps, B., Marmain, J., Guerin, C.A., 2022. A Reanalysis of the October 2016 “Meteotsunami” in British Columbia with Help of High-Frequency Radars and Autoregressive Modeling. IEEE Geosci. Remote Sensing Lett. 19, 1–5. https://doi.org/10.1109/LGRS.2021.3066849

Donnelly, C., Kraus, N., Larson, M., 2006. State of Knowledge on Measurement Modeling of Coastal Overwash. Journal of Coastal Research 22, 965–991. https://doi.org/10.2122/04-0431.1

Dragani, W.C., D’Onofrio, E.E., Grismeyer, W., Fiore, M.M.E., Campos, M.I., 2009. Atmospherically-induced water oscillations detected in the port of Quequén, Buenos Aires, Argentina. Physics and Chemistry of the Earth, Parts A/B/C 34, 998–1008. https://doi.org/10.1016/j.pce.2009.08.008

Durán, R., Guillén, J., Ruiz, A., Jiménez, J.A., Sagristà, E., 2016. Morphological changes, beach inundation and overwash caused by an extreme storm on a low-lying embayed beach bounded by a dune system (NW Mediterranean). Geomorphology 274, 129–142. https://doi.org/10.1016/j.geomorph.2016.09.012

Dusek, G., DiVeglio, C., Licate, L., Heilman, L., Kirk, K., Paternostro, C., Miller, A., 2019. A Meteotsunami Climatology along the U.S. East Coast. Bulletin of the American Meteorological Society 100, 1329–1345. https://doi.org/10.1175/BAMS-D-18-0206.1

El-Ashry, M.T., Wanless, H.R., 1965. Birth and early growth of a tidal delta. The Journal of Geology 73, 404–406.

El-Fishawi, N.1989. Coastal Erosion in Relation to Sea-Level Changes, Subsidence and River Discharge, Nile Delta Coast. Acta Mineralogica-Petrographica XXX, 161–171.

El Heraldo. Contratan Obras del Kilómetro 19 Con Firma Edgardo Navarro Vives. Available online: https://www.elheraldo.co/local/contratan-obras-del-kilometro-19-con-firma-edgardo-navarro-vives-167730 (accessed on 10 May 2021).

Elster, Carola, Perdomo, L., Polanía, J., Schnetter, M. L., 1999. Control of Avicennia germinans recruitment and survival by Junonia evarete larvae in a disturbed mangrove forest in Colombia. J. Trop. Ecol. 15, 791–805. https://doi.org/10.1017/S0266467499001182

Elster, C., Perdomo, L., Schnetter, M.L., 1999. Impact of ecological factors on the regeneration of mangroves in the Cienaga Grande de Santa Marta, Colombia. Hydrobiologia 413, 35–46.

Eshqi Molan, Y., Lu, Z., 2020. Modeling InSAR Phase and SAR Intensity Changes Induced by Soil Moisture. IEEE Trans. Geosci. Remote Sensing 58, 4967–4975. https://doi.org/10.1109/TGRS.2020.2970841

Farr, T.G., Rosen, P.A., Caro, E., Crippen, R., Duren, R., Hensley, S., Kobrick, M., Paller, M., Rodriguez, E., Roth, L., Seal, D., Shaffer, S., Shimada, J., Umland, J., Werner, M., Oskin, M., Burbank, D., Alsdorf, D., 2007. The Shuttle Radar Topography Mission. Rev. Geophys. 45, RG2004. https://doi.org/10.1029/2005RG000183

Ferreira, Ó., 2003. Prediction of the impact of cluster storms and their importance in coastal evolution, in: Coastal Engineering 2002. Presented at the Proceedings of the 28th International Conference, World Scientific Publishing Company, Cardiff, Wales, pp. 2725–2730. https://doi.org/10.1142/9789812791306_0227

Fisher, J.S., Stauble, D.K., 1977. Impact of Hurricane Belle on Assateague Island washover. Geology 5, 765–768.

FitzGerald, D.M., 1996. Geomorphic variability and morphologic and sedimentologic controls on tidal inlets. Journal of Coastal Research 23, 47–71.

FitzGerald, D.M., Fenster, M.S., Argow, B.A., Buynevich, I.V., 2008. Coastal Impacts Due to Sea-Level Rise. Annual Review of Earth and Planetary Sciences 36, 601–647. https://doi.org/10.1146/annurev.earth.35.031306.140139

Franceschetti, G., Lanari, R., 2018. Synthetic Aperture Radar Processing, 1st ed. CRC Press. https://doi.org/10.1201/9780203737484

Fruergaard, M., Kroon, A., 2016. Morphological response of a barrier island system on a catastrophic event: the AD 1634 North Sea storm. Earth Surf Processes Landf 41, 420–426. https://doi.org/10.1002/esp.3863

Galloway, W.E., Hobday, D.K., 1983. Terrigenous Clastic Depositional Systems. Springer-Verlag, New York.

Gómez, J. F., 2015. Dune and Coastal Evolution in Isla Salamanca National Park (M.Sc.). Wilfrid Laurier University, Waterloo, Ontario.

Gómez, J.F., Byrne, M.L., Hamilton, J., Isla, F., 2016. Historical Coastal Evolution and Dune Vegetation in Isla Salamanca National Park, Colombia. Journal of Coastal Research 33, 632. https://doi.org/10.2112/JCOASTRES-D-15-00189.1

Gómez, J.F., Kwoll, E., Walker, I.J., Shirzaei, M., 2021. Vertical Land Motion as a Driver of Coastline Changes on a Deltaic System in the Colombian Caribbean. Geosciences 11, 300. https://doi.org/10.3390/geosciences11070300

Gómez, J.F., Kwoll, E., Walker, I.J., Orejarena, A.F., 2023. Examining the Hydro-Climatic Drivers of Lagoon Breaching and Healing in a Deltaic Barrier. Geosciences 13, 118. https://doi.org/10.3390/geosciences13040118

Gregory, J.M., Griffies, S.M., Hughes, C.W., Lowe, J.A., Church, J.A., Fukimori, I., Gomez, N., Kopp, R.E., Landerer, F., Cozannet, G.L., Ponte, R.M., Stammer, D., Tamisiea, M.E., van de Wal, R.S.W., 2019. Concepts and Terminology for Sea Level: Mean, Variability and Change, Both Local and Global. Surv. Geophys 40, 1251–1289. https://doi.org/10.1007/s10712-019-09525-z

Hapke, C.J., Brenner, O., Hehre, R., Reynolds, B.J., 2013. Coastal Change from Hurricane Sandy and the 2012-13 Winter Storm Season: Fire Island, New York (No. 1231). United States Geological Survey, Reston, Virginia.

Hastenrath, S., 1990. Diagnostic and Prediction of Anomalous River Discharge in Northern South America. Journal of Climate 3, 1080–1096.

Heathfield, D.K., Walker, I.J., Atkinson, D.E., 2013. Erosive water level regime and climatic variability forcing of beach-dune systems on south-western Vancouver Island, British Columbia, Canada: Erosive Water Level Regime and Climate Variability Forcing. Earth Surface Processes and Landforms 38, 751–762. https://doi.org/10.1002/esp.3350

Heezen, B.C., 1956. Turbidity currents from the Magdalena River. Geological Society of America Bulletin 66, 1572.

Heidarzadeh, M., Šepić, J., Rabinovich, A., Allahyar, M., Soltanpour, A., Tavakoli, F., 2020. Meteorological Tsunami of 19 March 2017 in the Persian Gulf: Observations and Analyses. Pure Appl. Geophys. 177, 1231–1259. https://doi.org/10.1007/s00024-019-02263-8

Hein, C.J., Fitzgerald, D.M., Cleary, W.J., Albernaz, M.B., De Menezes, J.T., Klein, A.H., 2013. Evidence for a transgressive barrier within a regressive strandplain system: Implications for complex coastal response to environmental change. Sedimentology 60, 469–502. https://doi.org/10.1111/j.1365-3091.2012.01348.x

Hensley, S., Munjy, R., Rosen, P., 2001. Interferometric Synthetic Aperture Radar (IFSAR), in: Digital Elevation Model Technologies and Applications: The DEM Users Manual. American Society for Photogrammetry and Remote Sensing, Bethesda, Maryland, pp. 143–206.

Hesp, P., Short, A.D., 1999. Barrier morphodynamics, in: Handbook of Beach and Shoreface Morphodynamics. John Wiley & Sons, Chichester, pp. 307–333.

Houser, C., Hamilton, J., Meyer-Arendt, K., Oravetz, J., 2007., in: EOF Analysis of Morphological Response to Hurricane Ivan. Presented at the Coastal Sediments 2007. Proceedings of 6th International Symposium on Coastal Engineering and Science of Coastal Sediment Processes, American Society of Civil Engineers, New Orleans, pp. 1–10.

Houser, C., Hamilton, S., 2009. Sensitivity of post-hurricane beach and dune recovery to event frequency. Earth Surf. Process. Landforms 34, 613–628. https://doi.org/10.1002/esp.1730

Hsu, S.A. 1988. Coastal Meteorology. Academic Press, San Diego, Ca.

Hudock, J.W., Flaig, P.P., Wood, L.J., 2014. Washover Fans: A Modern Geomorphologic Analysis and Proposed Classification Scheme To Improve Reservoir Models. Journal of Sedimentary Research 84, 854–865. https://doi.org/10.2110/jsr.2014.64

Idárraga-García, J., Romero, J., 2010. Neotectonic study of the Santa Marta Fault System, Western foothills of the Sierra Nevada de Santa Marta, Colombia. Journal of South American Earth Sciences 29, 849–860. https://doi.org/10.1016/j.jsames.2009.11.004

Idárraga-García, J., Vargas, C.A., 2014. Morphological Expression of Submarine Landslides in the Accretionary Prism of the Caribbean Continental Margin of Colombia, in: Krastel, S., Behrmann, J.-H., Völker, D., Stipp, M., Berndt, C., Urgeles, R., Chaytor, J., Huhn, K., Strasser, M., Harbitz, C.B. (Eds.), Submarine Mass Movements and Their Consequences, Advances in Natural and Technological Hazards Research. Springer International Publishing, Cham, pp. 391–401. https://doi.org/10.1007/978-3-319-00972-8_35

James, T., Gowan, E.J., Hutchinson, I., Clague, J.J., Barrie, J.V., Conway, K.W., 2009. Sea-level change and paleogeographic reconstructions, southern Vancouver Island, British Columbia, Canada. Quaternary Science Reviews 28, 1200–1216. https://doi.org/10.1016/j.quascirev.2008.12.022

Jankowski, K.L., Törnqvist, T.E., Fernandes, A.M., 2017. Vulnerability of Louisiana's coastal wetlands to present-day rates of relative sea-level rise. Nat Commun 8, 14792. https://doi.org/10.1038/ncomms14792

Kim, H., Kim, M.S., Lee, H.-J., Woo, S.-B., Kim, Y.-K., 2016. Seasonal Characteristics and Mechanisms of Meteo-tsunamis on the West Coast of Korean Peninsula. Journal of Coastal Research 75, 1147–1151. https://doi.org/10.2112/SI75-230.1

Kim, M.S., Woo, S.B., Eom, H., You, S.H., 2021. Occurrence of pressure-forced meteotsunami events in the eastern Yellow Sea during 2010–2019. Nat. Hazards Earth Syst. Sci. 21, 3323–3337. https://doi.org/10.5194/nhess-21-3323-2021

Kjerfve, B., 1981. Tides of the Caribbean Sea. Journal of Geophysical Research 86, 4243–4247.

Kombiadou, K., Costas, S., Carrasco, A.R., Plomaritis, T.A., Ferreira, Ó., Matias, A., 2019. Bridging the gap between resilience and geomorphology of complex coastal systems. Earth-Science Reviews 198, 102934. https://doi.org/10.1016/j.earscirev.2019.102934

Lazarus, E.D., 2016. Scaling laws for coastal overwash morphology: Overwash Scaling. Geophysical Research Letters 43, 12,113-12,119. https://doi.org/10.1002/2016GL071213

Le Cozannet, G., Bulteau, T., Castelle, B., Ranasinghe, R., Wöppelmann, G., Rohmer, J., Bernon, N., Idier, D., Louisor, J., Salas-y-Mélia, D., 2019. Quantifying uncertainties of sandy shoreline change projections as sea level rises. Sci Rep 9, 42. https://doi.org/10.1038/s41598-018-37017-4

Leatherman, S.P., Williams, A.J., Fisher, J.S., 1977. Overwash sedimentation associated with a large-scale northeaster. Marine Geology 24, 109–121.

Leatherman, S.P., 1979. Migration of Assateague Island, Maryland, by inlet and overwash processes. Geology 7, 104–107. https://doi.org/doi-org.ezproxy.library.uvic.ca/10.1130/0091-7613(1979)7<104:MOAIMB>2.0.CO;2

Leatherman, S.P., 1983. Barrier dynamics and landward migration with Holocene sea-level rise. Nature 301, 415–417. https://doi.org/doi.org/10.1038/301415a0

Lentz, E.E., Hapke, C.J., Stockdon, H.F., Hehre, R.E., 2013. Improving understanding of near-term barrier island evolution through multi-decadal assessment of morphologic change. Marine Geology 337, 125–139. https://doi.org/10.1016/j.margeo.2013.02.004

Li, X., Huang, G., Kong, Q., 2018. Atmospheric Phase Delay Correction of D-InSAR Based on Sentinel-1A. ISPRS - International Archives of the Photogrammetry, Remote Sensing and Spatial Information Sciences XLII–3, 955–960. https://doi.org/10.5194/isprs-archives-XLII-3-955-2018

Lorenzo-Trueba, J., Ashton, A.D., 2014. Rollover, drowning, and discontinuous retreat: Distinct modes of barrier response to sea-level rise arising from a simple morphodynamic model. Journal of Geophysical Research: Earth Surface 119, 779–801. https://doi.org/10.1002/2013JF002941

Losada, I.J., Reguero, B.G., Méndez, F.J., Castanedo, S., Abascal, A.J., Mínguez, R., 2013. Long-term changes in sea-level components in Latin America and the Caribbean. Global and Planetary Change 104, 34–50. https://doi.org/10.1016/j.gloplacha.2013.02.006

Luo, Q., Perissin, D., Zhang, Y., Jia, Y., 2014. L- and X-Band Multi-Temporal InSAR Analysis of Tianjin Subsidence. Remote Sensing 6, 7933–7951. https://doi.org/10.3390/rs6097933

Matias, A., Ferreira, Ó., Vila-Concejo, A., Garcia, T., Dias, J.A., 2008. Classification of washover dynamics in barrier islands. Geomorphology 97, 655–674. https://doi.org/10.1016/j.geomorph.2007.09.010

Mazzotti, S., Lambert, A., Van der Kooij, M., Mainville, A., 2009. Impact of anthropogenic subsidence on relative sea-level rise in the Fraser River delta. Geology 37, 771–774. https://doi.org/10.1130/G25640A.1

McBride, R.A., 1999. Spatial and temporal distribution of historical and active tidal inlets: Delmarva Peninsula and New Jersey, USA, in: Coastal Sediments '99. Presented at the Coastal Sediments '99, American Society of Civil Engineers, New York, pp. 1505–1521.

Mendoza, E.T., Trejo-Rangel, M.A., Salles, P., Appendini, C.M., Lopez-Gonzalez, J., Torres-Freyermuth, A., 2013. Storm characterization and coastal hazards in the Yucatan Peninsula. Journal of Coastal Research 65, 790–795. https://doi.org/10.2112/SI65-134.1

Minderhoud, P.S.J., Middelkoop, H., Erkens, G., Stouthamer, E., 2020. Groundwater extraction may drown mega-delta: projections of extraction-induced subsidence and elevation of the Mekong delta for the 21st century. Environ. Res. Commun. 2, 011005. https://doi.org/10.1088/2515-7620/ab5e21

Miselis, J.L., Andrews, B.D., Nicholson, R.S., Defne, Z., Ganju, N.K., Navoy, A., 2016. Evolution of Mid-Atlantic Coastal and Back-Barrier Estuary Environments in Response to a Hurricane: Implications for Barrier-Estuary Connectivity. Estuaries and Coasts 39, 916–934. https://doi.org/10.1007/s12237-015-0057-x

Monserrat, S., Vilibic, I., Rabinovich, A.B., 2006. Meteotsunamis: atmospherically induced destructive ocean waves in the tsunami frequency band. Natural Hazards and Earth System Sciences 6, 1035–1051.

Moore, L.J., 2000. Shoreline Mapping Techniques. Journal of Coastal Research 16, 111–124.

Moore, L.J., List, J.H., Williams, S.J., Stolper, D., 2010. Complexities in barrier island response to sea level rise: Insights from numerical model experiments, North Carolina Outer Banks. J. Geophys. Res. 115, F03004. https://doi.org/10.1029/2009JF001299

Moore, L.J., Murray, A.B., 2018. Barrier Dynamics and Response to Changing Climate (Preface), in: Moore, L.J., Murray, A.B. (Eds.), Barrier Dynamics and Response to Changing Climate. Springer International Publishing, Cham, pp. vii–xvii.

Morrison, K., Bennett, J.C., Nolan, M., Menon, R., 2011. Laboratory Measurement of the DInSAR Response to Spatiotemporal Variations in Soil Moisture. IEEE Trans. Geosci. Remote Sensing 49, 3815–3823. https://doi.org/10.1109/TGRS.2011.2132137

Morrison, K., Bennett, J.C., Nolan, M., 2013. Using DInSAR to Separate Surface and Subsurface Features. IEEE Trans. Geosci. Remote Sensing 51, 3424–3430. https://doi.org/10.1109/TGRS.2012.2226183

Morton, R.A., Sallenger, A., 2003. Morphological impacts of extreme storms on sandy beaches and barrier. Journal of Coastal Research 19, 560–573.

Mount, J., Twiss, R., 2005. Subsidence, Sea Level Rise, and Seismicity in the Sacramento–San Joaquin Delta. SFEWS 3. https://doi.org/10.15447/sfews.2005v3iss1art7

Murray-Wallace, C.V., Woodroffe, C.D., 2014. Quaternary Sea-Level Changes. A Global Perspective, 1st ed. Cambridge University Press, New York.

Nienhuis, J.H., Ashton, A.D., Giosan, L., 2015. What makes a delta wave-dominated? Geology 43, 511–514. https://doi.org/10.1130/G36518.1

Odum, W.E., 1982. Environmental Degradation and the Tyranny of Small Decisions. BioScience 32, 728–729.

Oliver-Cabrera, T., Wdowinski, S., 2016. InSAR-Based Mapping of Tidal Inundation Extent and Amplitude in Louisiana Coastal Wetlands. Remote Sensing 8, 393. https://doi.org/10.3390/rs8050393

Orejarena-Rondón, A.F., Sayol, J.-M., Hernández-Carrasco, I., Cáceres-Euse, A., Restrepo, J.C., Orfila, A., 2022. Spatio-temporal variability of mean wave energy flux in the Caribbean Sea. J. Ocean Eng. Mar. Energy. https://doi.org/10.1007/s40722-022-00246-x

Ortiz-Royero, J.C., Otero, L.J., Restrepo, J.C., Ruiz, J., Cadena, M., 2013. Cold fronts in the Colombian Caribbean Sea and their relationship to extreme wave events. Nat. Hazards Earth Syst. Sci. 13, 2797–2804. https://doi.org/10.5194/nhess-13-2797-2013

Ortiz Royero, J.C., Cera, S.H., Gomes, H., 2021. Coastal Meteo-marine Parameters of Hurricane Matthew along the Colombian Caribbean Coast: Establishing a Baseline of Knowledge. Journal of Coastal Research 38. https://doi.org/10.2112/JCOASTRES-D-20-00108.1

Osorio, A.F., Mesa, J.C., Bernal, G.R., Montoya, R.D. 2009. Forty years of wave hindcast using Wave Watch III model and calibration with several sources at the Caribbean Sea. Boletín Científico CIOH 37–56.

Ospino, S., Restrepo, J.C., Otero, L., Pierini, J., Alvarez-Silva, O., 2018. Saltwater Intrusion into a River with High Fluvial Discharge: A Microtidal Estuary of the Magdalena River, Colombia. Journal of Coastal Research 34, 1273. https://doi.org/10.2112/JCOASTRES-D-17-00144.1

Otero, L.J., Ortiz-Royero, J.C., Ruiz-Merchan, J.K., Higgins, A.E., Henriquez, S.A., 2016. Storms or cold fronts: what is really responsible for the extreme waves regime in the Colombian Caribbean coastal region? Natural Hazards and Earth System Sciences 16, 391–401. https://doi.org/10.5194/nhess-16-391-2016

Pardo, J.M., Lozano, A., Herrera, G., Mulas, J., Rodríguez, A., 2013. Instrumental monitoring of the subsidence due to groundwater withdrawal in the city of Murcia (Spain). Environ Earth Sci 70, 1957–1963. https://doi.org/10.1007/s12665-013-2710-7

Paris, G., Machete, M.N., Dart, R.L., Haller, K.M., 2000. Maps and Database of Quaternary Folds and Faults in Colombia and its Offshore Regions (Open File No. 0284). United States Geological Survey, Denver.

Pattiaratchi, C.B., Wijeratne, E.M.S., 2014. Observations of meteorological tsunamis along the south-west Australian coast. Nat Hazards 74, 281–303. https://doi.org/10.1007/s11069-014-1263-8

Pattiaratchi, C.B., Wijeratne, E.M.S., 2015. Are meteotsunamis an underrated hazard? Phil. Trans. R. Soc. A. 373, 20140377. https://doi.org/10.1098/rsta.2014.0377

Pepe, A., Calò, F. 2017. A Review of Interferometric Synthetic Aperture RADAR (InSAR) Multi-Track Approaches for the Retrieval of Earth’s Surface Displacements. Applied Sciences 7, 1264. https://doi.org/10.3390/app7121264

Perez, I., 2018. Génesis, propagación e impacto de los tsunamis meteorológicos en la costa bonaerense, Argentina. Universidad de Buenos Aires. PhD Dissertation.

Perez, I., Dragani, W., 2021. Numerical study of meteotsunamis driven by atmospheric gravity waves in coastal waters of Buenos Aires Province, Argentina. Nat Hazards 106, 1599–1618. https://doi.org/10.1007/s11069-020-04485-9

Pierce, J.W., 1970. Tidal Inlets and Washover Fans. The Journal of Geology 78, 230–234. https://doi.org/10.1086/627504

Polcari, M., Albano, M., Montuori, A., Bignami, C., Tolomei, C., Pezzo, G., Falcone, S., La Piana, C., Doumaz, F., Salvi, S., Stramondo, S., 2018. InSAR Monitoring of Italian Coastline Revealing Natural and Anthropogenic Ground Deformation Phenomena and Future Perspectives. Sustainability 10, 3152. https://doi.org/10.3390/su10093152

Portos-Amill, L., Nienhuis, J.H., de Swart, H.E., 2023. Gradual Inlet Expansion and Barrier Drowning Under Most Sea Level Rise Scenarios. JGR Earth Surfce, Prediction in coastal geomorphology 1–20. https://doi.org/10.1029/2022JF007010

Poveda, G., 2004. La hidroclimatología de Colombia: Una síntesis desde la escala inter-decadal hasta la escala diurna. Revista de la Academia Colombiana de Ciencias Exactas, Físicas y Naturales 28, 201–222.

Proudman, J., 1929. The effects on the sea of changes in atmospheric pressure. Geophysical Journal International 2, 197–209.

Pugh, D., 2004. Changing Sea Levels: Effects of Tides, Weather and Climate, 1st ed. Cambridge Univesity Press, Cambridge.

Pugh, D., Woodworth, P., 2014. Sea-Level Science: Understanding Tides, Surges, Tsunamis and Mean Sea-Level Changes. Cambridge University Press, Cambridge. https://doi.org/10.1017/CBO9781139235778

Rabinovich, A.B., Monserrat, S., 1996. Meteorological Tsunamis near the Balearic and Kuril Islands: Descriptive and Statistical Analysis. Natural Hazards 13, 55–90.

Rabinovich, A.B., 2020. Twenty-Seven Years of Progress in the Science of Meteorological Tsunamis Following the 1992 Daytona Beach Event. Pure Appl. Geophys. 177, 1193–1230. https://doi.org/10.1007/s00024-019-02349-3

Rabinovich, A.B., Šepić, J., Thomson, R.E., 2021. The meteorological tsunami of 1 November 2010 in the southern Strait of Georgia: a case study. Nat Hazards 106, 1503–1544. https://doi.org/10.1007/s11069-020-04203-5

Rabinovich, A.B., Šepić, J., Thomson, R.E., 2023. Strength in Numbers: The Tail End of Typhoon Songda Combines with Local Cyclones to Generate Extreme Sea Level Oscillations on the British Columbia and Washington Coasts during Mid-October 2016. Journal of Physical Oceanography 53, 131–155. https://doi.org/10.1175/JPO-D-22-0096.1

Rampino, M.R., Sanders, J.E., 1981. Evolution of the barrier islands of southern Long Island, New York. Sedimentology 28, 37–47.

Rao, J.S., Liu, H., 2017. Discordancy Partitioning for Validating Potentially Inconsistent Pharmacogenomic Studies. Sci Rep 7, 15169. https://doi.org/10.1038/s41598-017-15590-4

Restrepo-Ángel, J.D., Mora-Páez, H., Díaz, F., Govorcin, M., Wdowinski, S., Giraldo-Londoño, L., Tosic, M., Fernández, I., Paniagua-Arroyave, J.F., Duque-Trujillo, J.F., 2021.

Coastal subsidence increases vulnerability to sea level rise over twenty first century in Cartagena, Caribbean Colombia. Sci Rep 11, 18873. https://doi.org/10.1038/s41598-021-98428-4

Restrepo, J.C., Ortíz, J.C., Pierini, J., Schrottke, K., Maza, M., Otero, L., Aguirre, J., 2014. Freshwater discharge into the Caribbean Sea from the rivers of Northwestern South America (Colombia): Magnitude, variability and recent changes. Journal of Hydrology 509, 266–281. https://doi.org/10.1016/j.jhydrol.2013.11.045

Restrepo, J.C., Schrottke, K., Traini, C., Ortiz, J.C., Orejarena, A., Otero, L., Higgins, A., Marriaga, L., 2016. Sediment Transport Regime and Geomorphological Change in a High-Discharge Tropical Delta (Magdalena River, Colombia): Insights from a Period of Intense Change and Human Intervention (1990–2010). Journal of Coastal Research 32, 575–589. https://doi.org/doi.org/10.2112/JCOASTRES-D-14-00263.1

Restrepo, J.D., Kjerfve, B., 2000. Magdalena river: interannual variability (1975–1995) and revised water discharge and sediment load estimates. Journal of Hidrology 235, 137–149.

Restrepo, J.D., Kjerfve, B., Hermelin, M., Restrepo, J.C., 2006. Factors controlling sediment yield in a major South American drainage basin: the Magdalena River, Colombia. Journal of Hydrology 316, 213–232. https://doi.org/10.1016/j.jhydrol.2005.05.002

Rey, W., Salles, P., Torres-Freyermuth, A., Ruíz-Salcines, P., Teng, Y.-C., Appendini, C.M., Quintero-Ibáñez, J., 2019. Spatiotemporal Storm Impact on the Northern Yucatan Coast during Hurricanes and Central American Cold Surge Events. JMSE 8, 2. https://doi.org/10.3390/jmse8010002

Rich, A., Keller, E.A., 2013. A hydrologic and geomorphic model of estuary breaching and closure. Geomorphology 191, 64–74. https://doi.org/10.1016/j.geomorph.2013.03.003

Rico, E., 1967. Las Obras de Bocas de Ceniza. Colpuertos, Barranquilla.

Roberts, H.H., 1997. Dynamic changes of the Holocene Mississippi River Delta Plain: The Delta Cycle. Journal of Coastal Research 13, 605–627.

Robertson, C., Nelson, T.A., Boots, B., Wulder, M.A., 2007. STAMP: spatial–temporal analysis of moving polygons. J Geograph Syst 9, 207–227. https://doi.org/10.1007/s10109-007-0044-2

Rohli, R.V., Li, C., 2021. Meteorology for Coastal Scientists. Springer International Publishing, Cham. https://doi.org/10.1007/978-3-030-73093-2

Romero-Otero, G.A., Slatt, R.M., Pirmez, C., 2015. Evolution of the Magdalena Deepwater Fan in a Tectonically Active Setting, Offshore Colombia, in: Bartolini, C., Mann, P. (Eds.), Memoir 108: Petroleum Geology and Potential of the Colombian Caribbean Margin. AAPG. https://doi.org/10.1306/13531953M1083656

Ruggiero, P., 2004. Wave run-up on a high-energy dissipative beach. J. Geophys. Res. 109, C06025. https://doi.org/10.1029/2003JC002160

Salaree, A., Mansouri, R., Okal, E.A., 2018. The intriguing tsunami of 19 March 2017 at Bandar Dayyer, Iran: field survey and simulations. Nat Hazards 90, 1277–1307. https://doi.org/10.1007/s11069-017-3119-5

Sallenger, A. H., Jeffrey, H., Gelfenbau, G., Stumpf, R.P., Hansen, M., 1995. Large Wave at Daytona Beach, Florida, Explained as a Squall-line Surge. Journal of Coastal Research 11, 1383–1388.

Sallenger Jr., A.H., 2000. Storm impact scale for barrier islands. Journal of Coastal Research 16, 890–895.

Sansosti, E., Berardino, P., Manunta, M., Serafino, F., Fornaro, G., 2006. Geometrical SAR image registration. IEEE Trans. Geosci. Remote Sensing 44, 2861–2870. https://doi.org/10.1109/TGRS.2006.875787

Šepić, J., Vilibić, I., Rabinovich, A.B., Monserrat, S., 2015. Widespread tsunami-like waves of 23-27 June in the Mediterranean and Black Seas generated by high-altitude atmospheric forcing. Sci Rep 5, 11682. https://doi.org/10.1038/srep11682

Sherwood, C.R., Long, J.W., Dickhudt, P.J., Dalyander, P.S., Thompson, D.M., Plant, N.G., 2014. Inundation of a barrier island (Chandeleur Islands, Louisiana, USA) during a hurricane: Observed water-level gradients and modeled seaward sand transport. JGR Earth Surface 119, 1498–1515. https://doi.org/10.1002/2013JF003069

Sherwood, C.R., Ritchie, A.C., Over, J.R., Kranenburg, C.J., Warrick, J.A., Brown, J.A., Wright, C.W., Aretxabaleta, A.L., Zeigler, S.L., Wernette, P.A., Buscombe, D.D., Hegermiller, C.A., 2023. Sound-Side Inundation and Seaward Erosion of a Barrier Island During Hurricane Landfall. JGR Earth Surface 128. https://doi.org/10.1029/2022JF006934

Shirzaei, M., Walter, T.R., 2011. Estimating the Effect of Satellite Orbital Error Using Wavelet-Based Robust Regression Applied to InSAR Deformation Data. IEEE Trans. Geosci. Remote Sensing 49, 4600–4605. https://doi.org/10.1109/TGRS.2011.2143419

Shirzaei, M., Bürgmann, R., 2012. Topography correlated atmospheric delay correction in radar interferometry using wavelet transforms: TCAD REDUCTION IN INSAR USING WAVELETS. Geophys. Res. Lett. 39, n/a-n/a. https://doi.org/10.1029/2011GL049971

Shirzaei, M., 2013. A Wavelet-Based Multitemporal DInSAR Algorithm for Monitoring Ground Surface Motion. IEEE Geosci. Remote Sensing Lett. 10, 456–460. https://doi.org/10.1109/LGRS.2012.2208935

Shirzaei, M., Bürgmann, R., Fielding, E.J., 2017. Applicability of Sentinel-1 Terrain Observation by Progressive Scans multitemporal interferometry for monitoring slow ground motions in the San Francisco Bay Area: Sentinel-1 Multitemporal Interferometry. Geophys. Res. Lett. 44, 2733–2742. https://doi.org/10.1002/2017GL072663

Shirzaei, M., Bürgmann, R., 2018. Global climate change and local land subsidence exacerbate inundation risk to the San Francisco Bay Area. Sci. Adv. 4, eaap9234. https://doi.org/10.1126/sciadv.aap9234

Shirzaei, M., Freymueller, J., Törnqvist, T.E., Galloway, D.L., Dura, T., Minderhoud, P.S.J., 2021. Measuring, modelling and projecting coastal land subsidence. Nat Rev Earth Environ 2, 40–58. https://doi.org/10.1038/s43017-020-00115-x

Srinivas, R., Dean, R.G., 1996. Cross-shore hydrodynamics and profile response modelling. Coastal Engineering 27, 195–221.

Stockdon, H.F., Holman, R.A., Howd, P.A., Sallenger, A.H., 2006. Empirical parameterization of setup, swash, and runup. Coastal Engineering 53, 573–588. https://doi.org/10.1016/j.coastaleng.2005.12.005

Stockdon, H.F., Sallenger, A.H., Holman, R.A., Howd, P.A., 2007. A simple model for the spatially-variable coastal response to hurricanes. Marine Geology 238, 1–20. https://doi.org/10.1016/j.margeo.2006.11.004

Storms, J.E.A., Weltje, G.J., Terra, G.J., Cattaneo, A., Trincardi, F., 2008. Coastal dynamics under conditions of rapid sea-level rise: Late Pleistocene to Early Holocene evolution of barrier–lagoon systems on the northern Adriatic shelf (Italy). Quaternary Science Reviews 27, 1107–1123. https://doi.org/10.1016/j.quascirev.2008.02.009

Stutz, M.L., Pilkey, O.H., 2002. Global Distribution and Morphology of Deltaic Barrier Island Systems. Journal of Coastal Research 36, 694–707. https://doi.org/10.2112/1551-5036-36.sp1.694

Swift, D.J.P., 1975. Barrier-Island genesis: evidence from the Central Atlantic shelf, Eastern U.S.A. Sedimentary Geology 14, 1–43.

Swift, D.J.P., Thorne, J.A., 1991. Sedimentation on Continental margins, I: A General model for shelf sedimentation, in: Shelf Sand and Sandstone Bodies: Geometry, Facies and Sequence Stratigraphy. U.S.A.

Syvitski, J.P.M., Kettner, A.J., Overeem, I., Hutton, E.W.H., Hannon, M.T., Brakenridge, G.R., Day, J., Vörösmarty, C., Saito, Y., Giosan, L., Nicholls, R.J., 2009. Sinking deltas due to human activities. Nature Geoscience 2, 681–686. https://doi.org/10.1038/ngeo629

Teatini, P., Tosi, L., Strozzi, T., 2011. Quantitative evidence that compaction of Holocene sediments drives the present land subsidence of the Po Delta, Italy. J. Geophys. Res. 116, B08407. https://doi.org/10.1029/2010JB008122

Thieler, R., Young, R., 1991. Quantitative Evaluation of Coastal Geomorphological Changes in South Carolina After Hurricane Hugo. Journal of Coastal Research 8, 187–200.

Törnqvist, T.E., Wallace, D.J., Storms, J.E.A., Wallinga, J., van Dam, R.L., Blaauw, M., Derksen, M.S., Klerks, C.J.W., Meijneken, C., Snijders, E.M.A., 2008. Mississippi Delta subsidence primarily caused by compaction of Holocene strata. Nature Geosci 1, 173–176. https://doi.org/10.1038/ngeo129

Torregroza-Espinosa, A.C., Restrepo, J.C., Correa-Metrio, A., Hoyos, N., Escobar, J., Pierini, J., Martínez, J.-M., 2020. Fluvial and oceanographic influences on suspended sediment dispersal in the Magdalena River Estuary. Journal of Marine Systems 204, 103282. https://doi.org/10.1016/j.jmarsys.2019.103282

Tosi, L., Da Lio, C., Strozzi, T., Teatini, P., 2016. Combining L- and X-Band SAR Interferometry to Assess Ground Displacements in Heterogeneous Coastal Environments: The Po River Delta and Venice Lagoon, Italy. Remote Sensing 8, 308. https://doi.org/10.3390/rs8040308

United States Geological Survey. Latest Earthquakes Report. Available online: https://earthquake.usgs.gov/earthquakes (accessed on 8 January 2021).

Van de Lageweg, W.I., Bryan, K.R., Coco, G., Ruessink, B.G., 2013. Observations of shoreline–sandbar coupling on an embayed beach. Marine Geology 344, 101–114. https://doi.org/10.1016/j.margeo.2013.07.018

Van Heteren, S., 2014. Barrier Systems, in: Coastal Environments and Global Change. John Wiley & Sons, pp. 194–226.

Vargas, C. A., Idárraga-García, J., 2014. Age Estimation of Submarine Landslides in the Aguja Submarine Canyon, Northwestern Colombian, in: Submarine Mass Movements and Their Consequences: 6th International Symposium, Advances in Natural and Technological Hazards Research. Switzerland, pp. 629–638. https://doi.org/10.1007/978-3-319-00972-8_35

Vilardo, G., Ventura, G., Terranova, C., Matano, F., Nardò, S., 2009. Ground deformation due to tectonic, hydrothermal, gravity, hydrogeological, and anthropic processes in the Campania Region (Southern Italy) from Permanent Scatterers Synthetic Aperture Radar Interferometry. Remote Sensing of Environment 113, 197–212. https://doi.org/10.1016/j.rse.2008.09.007

Vilibić, I., 2008. Numerical simulations of the Proudman resonance. Continental Shelf Research 28, 574–581. https://doi.org/10.1016/j.csr.2007.11.005

Vilibić, I., Denamiel, C., Zemunik, P., Monserrat, S., 2021a. The Mediterranean and Black Sea meteotsunamis: an overview. Nat Hazards 106, 1223–1267. https://doi.org/10.1007/s11069-020-04306-z

Vilibić, I., Horvath, K., Strelec Mahović, N., Monserrat, S., Marcos, M., Amores, Á., Fine, I., 2014. Atmospheric processes responsible for generation of the 2008 Boothbay meteotsunami. Nat Hazards 74, 25–53. https://doi.org/10.1007/s11069-013-0811-y

Vilibić, I., Rabinovich, A.B., Anderson, E.J., 2021b. Special issue on the global perspective on meteotsunami science: editorial. Nat Hazards 106, 1087–1104. https://doi.org/10.1007/s11069-021-04679-9

Von Erffa, A.F., 1973. Sedimentation, transport und erosion an der nordkuste kolumbiens zwischen Barranquilla und der Sierra Nevada de Santa Marta. Boletín de Investigaciones Científicas Colombo-Alemán 7, 155–209.

Vučetić, T., Vilibić, I., Tinti, S., Maramai, A., 2009. The Great Adriatic flood of 21 June 1978 revisited: An overview of the reports. Physics and Chemistry of the Earth, Parts A/B/C 34, 894–903. https://doi.org/10.1016/j.pce.2009.08.005

Walker, I.J., Davidson-Arnott, R.G.D., Bauer, B.O., Hesp, P.A., Delgado-Fernandez, I., Ollerhead, J., Smyth, T.A.G., 2017. Scale-dependent perspectives on the geomorphology and evolution of beach-dune systems. Earth-Science Reviews 171, 220–253. https://doi.org/10.1016/j.earscirev.2017.04.011

Werner, C., Wegmüller, U., Strozzi, T. Wiesmann, A. 2000. Gamma SAR and interferometric processing software. Presented at the ERS-ENVISAT Symposium, Gothemburg, Sweden.

Yague-Martinez, N., Prats-Iraola, P., Rodriguez Gonzalez, F., Brcic, R., Shau, R., Geudtner, D., Eineder, M., Bamler, R., 2016. Interferometric Processing of Sentinel-1 TOPS Data. IEEE Trans. Geosci. Remote Sensing 54, 2220–2234. https://doi.org/10.1109/TGRS.2015.2497902

Yuill, B., Lavoie, D., Reed, D.J., 2009. Understanding Subsidence Processes in Coastal Louisiana. Journal of Coastal Research 10054, 23–36. https://doi.org/10.2112/SI54-012.1

Zăinescu, F.I., Vespremeanu-Stroe, A., Tătui, F., 2019. The formation and closure of the Big Breach of Sacalin spit associated with extreme shoreline retreat and shoreface erosion. Earth Surf. Process. Landforms 44, 2268–2284. https://doi.org/10.1002/esp.4639

Zhang, J.-Z., Huang, H., Bi, H., 2015. Land subsidence in the modern Yellow River Delta based on InSAR time series analysis. Nat Hazards 75, 2385–2397. https://doi.org/10.1007/s11069-014-1434-7

Zoccarato, C., Minderhoud, P.S.J., Teatini, P., 2018. The role of sedimentation and natural compaction in a prograding delta: insights from the mega Mekong delta, Vietnam. Sci Rep 8, 11437. https://doi.org/10.1038/s41598-018-29734-7

Chapter 7. List of Appendices

7.1 **Appendix 1.** VLM rates for 2017–2021 as derived from Sentinel 1A/B data and coastline changes for 2010–2020. Data are shown for pixels aggregations of 1.5 km² and 5.0 km²

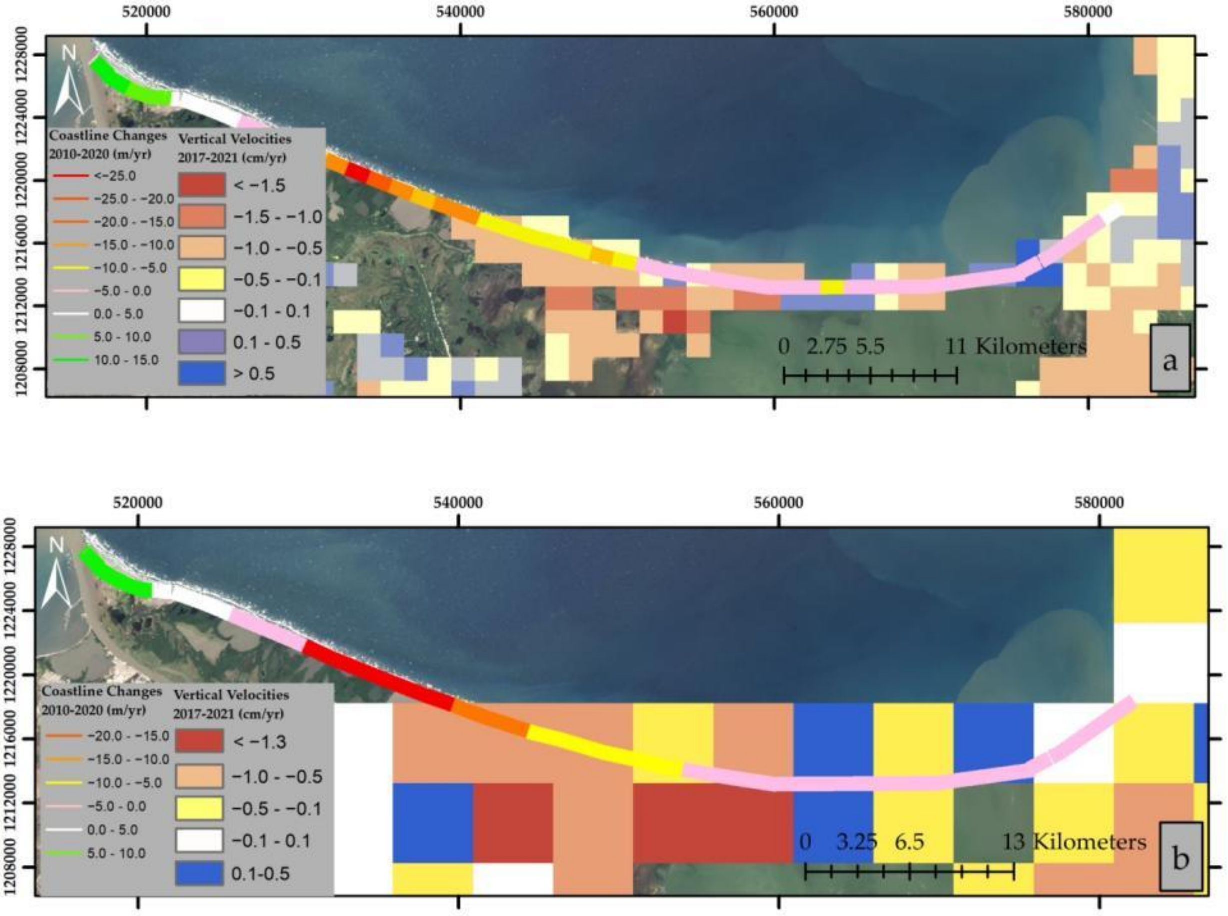

VLM rates for 2017–2021 as derived from Sentinel 1A/B data and coastline changes for 2010–2020. Data was aggregated in (**a**) 1.5-km and (**b**) 5.0-km sections.

7.2 **Appendix 2.** Video showing coastline and lagoon changes for 1973-2020.

https://www.mdpi.com/arcticle/10.3390/geosciences13040118/s1. Alternatively, see attached file: Appendix2.zip

7.3 **Appendix 3**. Breaching and Healing Events for 1973-2020.

Date	**LAGOON**			
	El Torno	**Las Piedras**	**La Atascosa**	**Cuatro Bocas**
1978-11-14	X	X?		
1979-01-07	X			
1979-02-12	X			
1984-01-30	X	X	X	X
1984-09-02	X	X	X	X
1984-12-23		X		
1985-01-24		X		
1985-01-08		X		
1985-02-09		X		
1985-02-25	X	X	X	X
1985-04-30	X	X	X	X
1986-01-11	X	X	X	X
1986-03-16	X	X	X	X
1986-07-06			X	X
1986-08-07			X	X
1986-09-08			X?	X
1986-11-11				X
1986-12-13				X
1986-12-29	X	X	X	X
1987-01-14			XX	XX
1987-01-30			X	X
1987-03-19			X	X
1987-07-25				X
1987-08-10				X
1987-10-13			X	X

1988-05-16	X	X	X	X
1988-06-01			X	
1988-09-21			X	
1988-10-23			X	X
1988-11-08			X	
1989-01-11			X	
1989-10-26			X	
1989-12-21			X	
1990-07-09	X	X	X	X
1991-03-14	X	X	X	X
1991-04-15		X		
1991-06-02		X		
1991-11-09		X		
1991-11-25		X?		
1991-12-11		X?		
1996-07-17	X	X	X	X
1996-08-21		X		
1996-09-03		X		
1996-09-19		X		
1996-10-05		X		
1996-10-21		XX		
1997-03-05	X	X	X	X
1997-03-11	X	X?	X	X
1997-10-08		X		
1998-03-01	X	X	X	X
1998-03-17		X		
1998-04-02		X		
1998-04-18		X		
1998-05-20		X		
1998-06-21		X?		
1998-09-09		X		
1998-09-25		X		
1998-12-30		X?		
1999-01-31		X		
1999-04-05		X		

1999-07-02		X		
1999-10-14		X		
1999-10-22		X		X
1999-11-23		X		X
2000-03-14		X		X
2000-05-09		X		X
2000-05-25		X		
2000-06-02		X		
2000-06-26		X		X
2000-07-02		X		
2000-08-21		X		
2000-11-25		X		
2001-01-12		X		
2001-05-02		X	X	X?
02/21/2001		X		X?
2001-03-01		X		
2001-11-28			X	X
2001-12-14				X
2002-05-01				X
2002-03-04	X	X	X	X
2002-06-24			X	X
2002-11-15				X?
2003-02-19		X?		X?
2003-03-17				X
2003-08-01				X
2003-12-20			X	X
2004-01-01			X	X
2004-01-21				X
2004-01-30				X
2004-02-22				X
2004-03-09			X	X
2004-03-25			X	X
2004-05-12			X	X
2004-05-12			X	X
2004-07-31			X	X

2004-11-04			X?	X?
2004-11-20			X?	X
2004-12-06			X	X?
2005-02-15	X	X	X	X
2005-02-24	X	X	X	x
2005-05-31			X	X?
2005-10-06			X	X
2005-12-09			X	X
2006-07-21			X	X
2006-08-22			X	X
2006-09-07				X
2006-11-01				X
2006-11-10	X	X	X	X
2006-12-28				X
2007-01-29	X	X	X	X
2007-03-02			🟩	X
2007-04-19		X	🟩	
2007-06-22		X	🟩	
2007-07-24		X	X	X
2007-11-29		X	X	X
2008-01-16		X		
2008-02-21		X		
2008-03-20		X		
2008-05-04		X	X	
2008-07-05		X	X	
2008-05-23		X?	X?	X?
2008-06-16		X		
2008-12-09			X	
2008-10-14			X	
2008-11-15			X	X?
2008-12-17			X	X
2008-12-31			X	
2009-01-30			X	
2009-02-03			X	
2009-03-07	PUERTO COLOMBIA PIER COLLAPSED			

2009-03-23			X	X
2009-04-03			X	
009-04-10	X		X	X
2009-05-18			X	
2009-05-26			X	
2009-06-27			X	X
2009-08-26			X	X
2009-09-10			X	X
2009-09-24			X	X
2009-10-01				X
2009-10-17				X
2009-10-26				X
2009-11-09				X?
2009-11-26			X	X
2009-12-21	X	X	X	X
2010-02-05	X	X	X	X
2010-06-05				X
2010-07-20				X
2010-08-12				X
2010-08-29			X	X
2010-10-04			X	X
2010-10-23			X	
2010-11-11			X	X
2010-12-07				X
2010-12-24			X	X
2011-01-11			X	X
2011-01-30			X	X
2011-02-09			X	X
2011-03-05	X	X	X	X
2011-03-13			X	X
2011-03-23		X		
2011-04-30	X	X	X	X
2011-05-20	X	X	X	X
2011-06-17		X	X	X
2011-07-19		X	X?	X

2011-07-25		NA	X	X
2011-08-04	X	X	X	X
2011-09-05	X	X	X	X
2011-09-21	X	X	X	X
2011-10-07				X
2011-10-23		X		
2011-11-24		X		X
2011-12-10		X	X	X
2011-12-28		X	X	X
2012-01-27		X	X	X
2012-02-27	X	X	X	X
2012-03-12	X	X	X	X
2012-07-21	X	X	X	X
2012-07-27	X	X	X	X
2012-11-28	X	X	X	X
2013-01-27	X	X	X	X
2013-01-29	X	X	X	X
2013-03-27	X	X	X	X
2013-12-12	X	X	X	X
2013-12-15	X	X	X	X
2014-01-21	X	X	X	X
2014-03-20	X	X	X	X
2014-07-23	X	X	X	X
2014-11-27	X	X	X	X
2015-02-25	X	X	X	X
2015-04-09	X	X	X	X
2015-04-17				X
2015-04-22	X	X	X	X
2015-05-11				X
2015-07-13				X
2015-07-30				X
2015-10-22				X
2015-11-06				X
2015-12-24	X	X	X	X
2016-05-01				X

2016-05-25				X
2016-06-02			X	X
2016-02-23			X	X
2016-03-01			X	X
2016-03-11			X	X
2016-03-26			X	X
2016-04-14			X	X
2016-05-06			X	X
2016-05-13			X	X
2016-05-19			X	X
2016-07-17			X	X
2016-08-02			X	X
2016-08-27			X	X
2016-09-26	X	X	X	X
2016-10-15	X	X	XX	X
2016-12-12			X	X
2017-02-25			X	X
2017-03-03	X	X	X	X
2017-03-21			X	X
2017-04-06			X	X
2017-04-12			X	X
2017-07-14			X	
2017-07-18			X	
2017-07-19	High Water Levels at around 8:30 a.m. as reported by readings of tide gauge in Santa Marta			
2017-07-24			XX	
2018-04-09			X	
2018-04-25			X	
2018-05-26	X	X	X	X
2018-06-03	X	X	X	
2018-07-08	X	X	X	X
2018-07-13	X	X	X	X
2018-07-15			X	
2018-08-31			X	

2018-11-30	X 🟩	X 🟩	X	
2018-12-30	X 🟩	X 🟩	X	X 🟩
2019-01-15			X	
2019-02-06			X	
2019-02-25			X 🟩	
2019-05-22			X	
2019-06-15		X 🟩	X	X 🟩
2019-08-27			X	
2019-10-05			X	
2019-11-22			X	
2020-01-19			X	
2020-01-26			X	
2020-08-10	X 🟩	X 🟩	X 🟩	X 🟩
2020-09-05		X	X 🟩	X 🟩
2020-09-06		X		
2020-09-21		X	🟩	🟩
30/11/2020		X		
29/12/2020	X 🟩	X	X 🟩	X 🟩

LEGEND	
▨	Inlet getting healed
🟩	Inlet completely healed
X	Lagoon breached
XX	More than one breach along the same lagoon

7.4 **Appendix 4.** Relative Humidity on July 19, 2017.

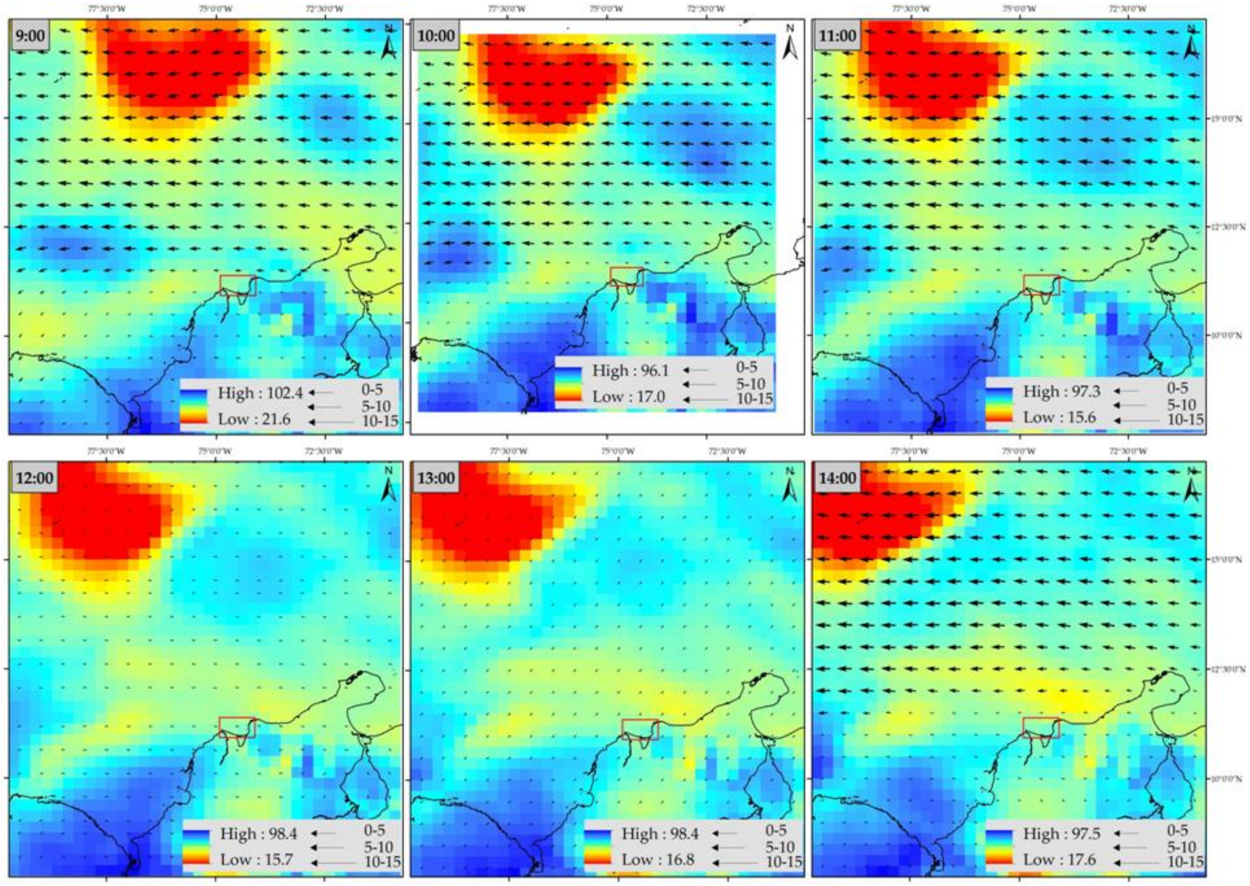

7.5 **Appendix 5.** Video showing northward displacement of cold front along the Colombian Caribbean coast on July 19, 2017.

See attached file: Appendix5_Goes_13_Band6_IR.mp4.

7.6 Appendix 6. Readings of hourly pressure from onshore stations on July 19, 2017.

For location of stations see Figure 30 in manuscript.

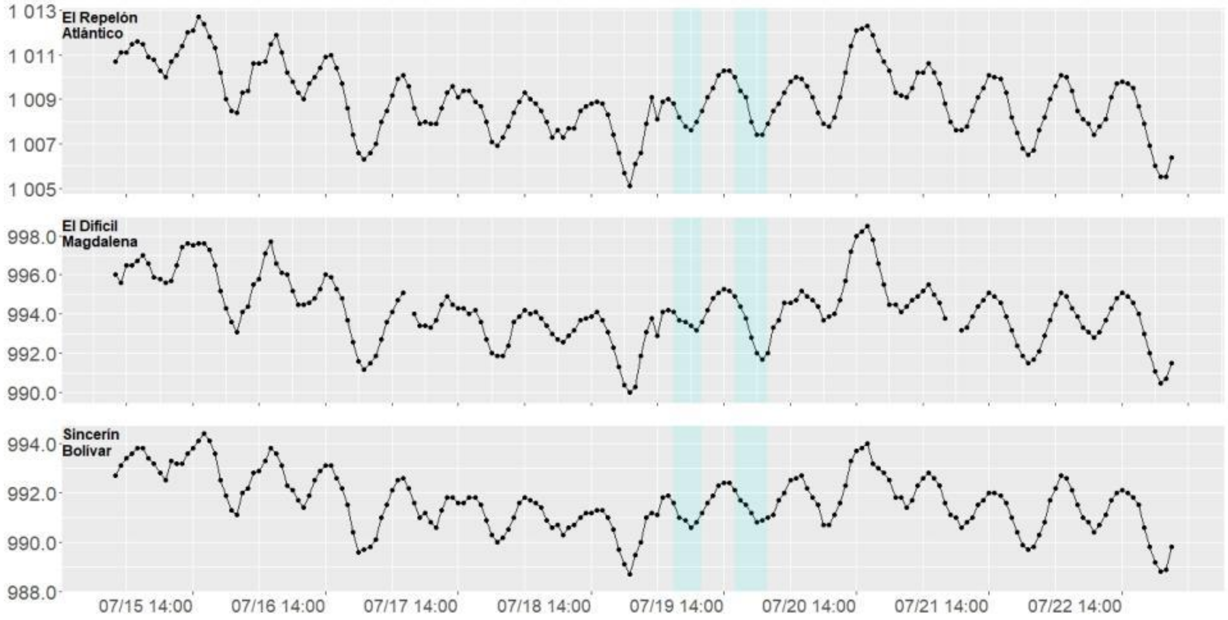

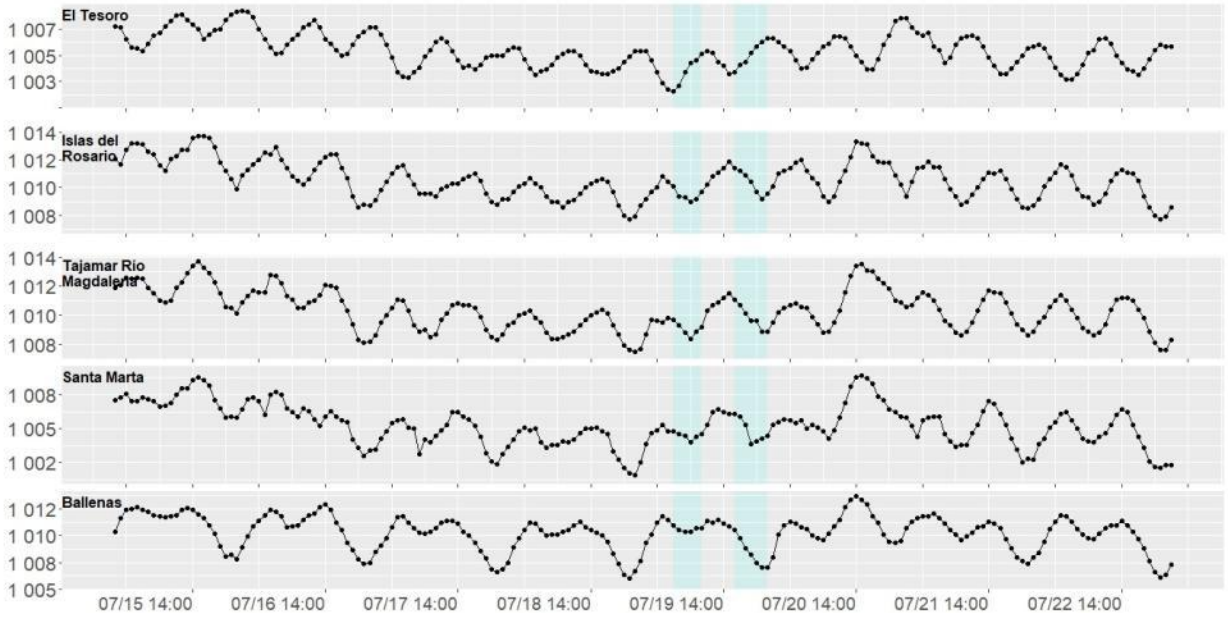

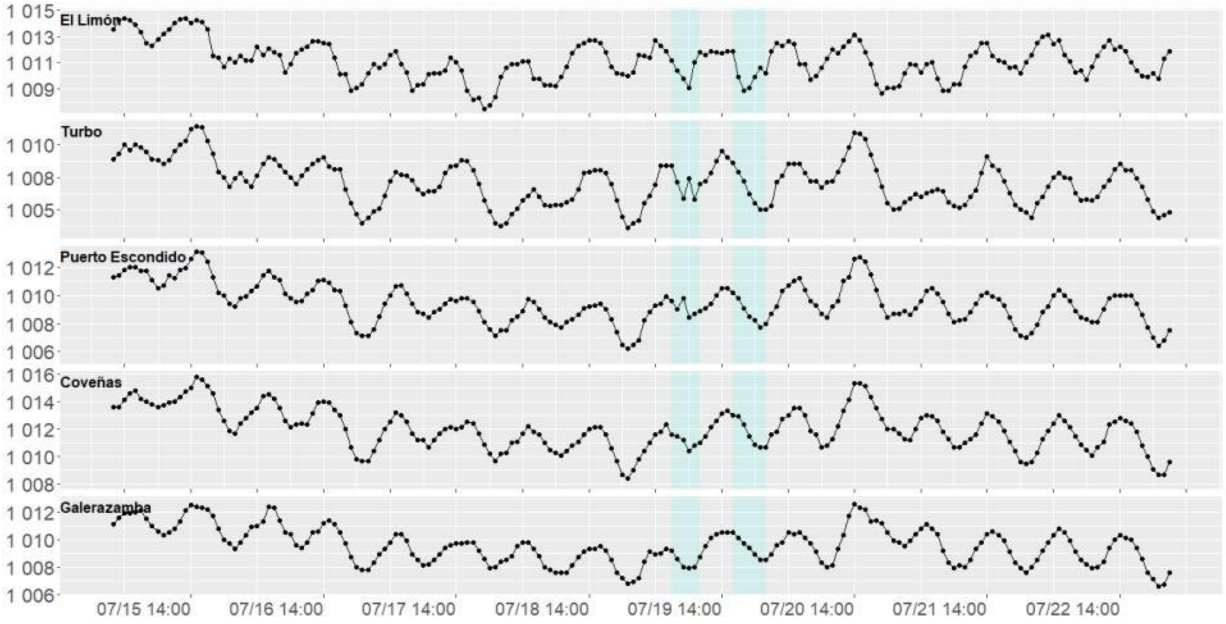
El Limón
1 015
1 013
1 011
1 009
Turbo
1 010
1 008
1 005
Puerto Escondido
1 012
1 010
1 008
1 006
Coveñas
1 016
1 014
1 012
1 010
1 008
Galerazamba
1 012
1 010
1 008
1 006
07/15 14:00
07/16 14:00
07/17 14:00
07/18 14:00
07/19 14:00
07/20 14:00
07/21 14:00
07/22 14:00

7.7 **Appendix 7.** Readings of hourly wind direction and speed in Riohacha, Galerazamba and El Tesoro on July 19, 2017.

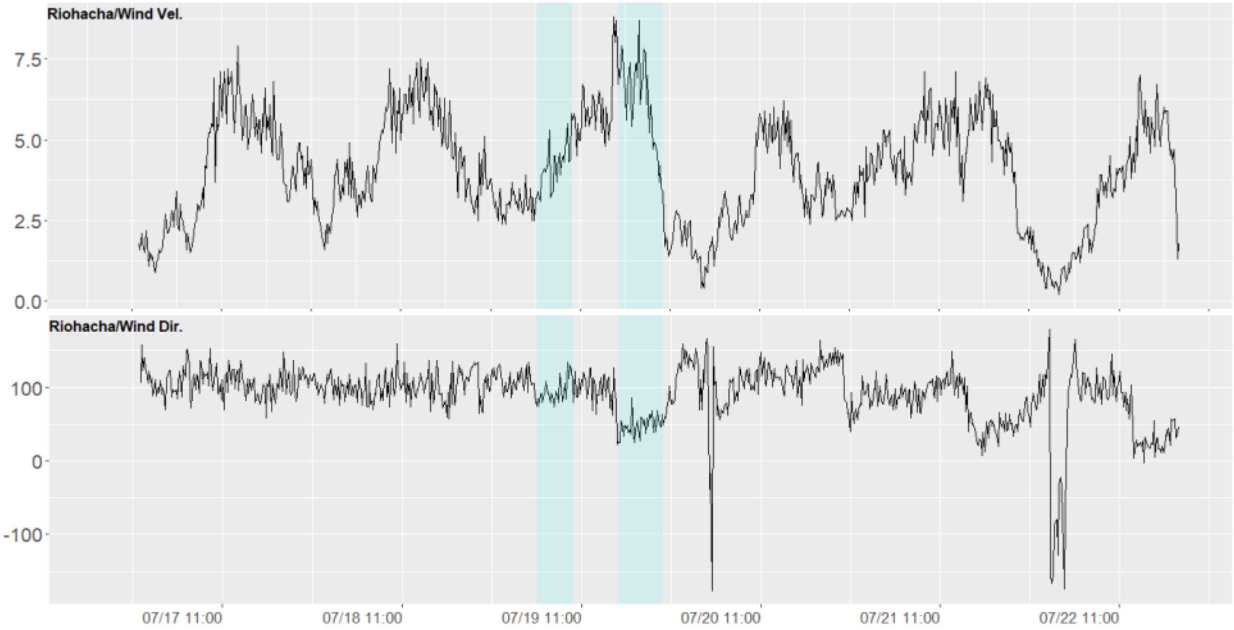

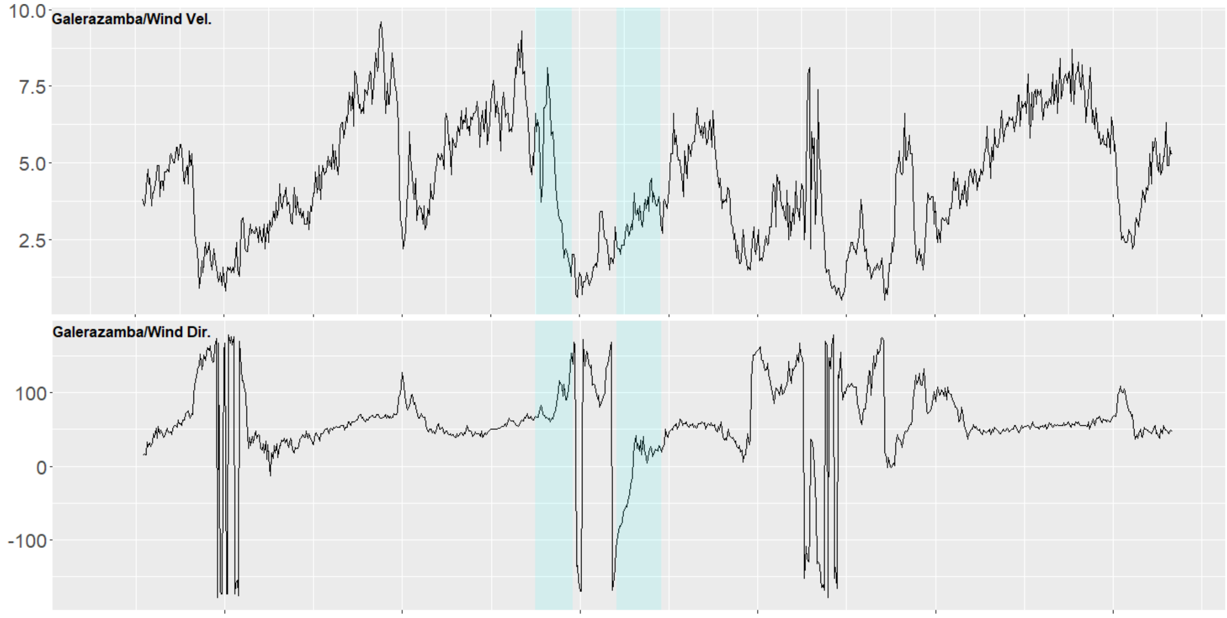

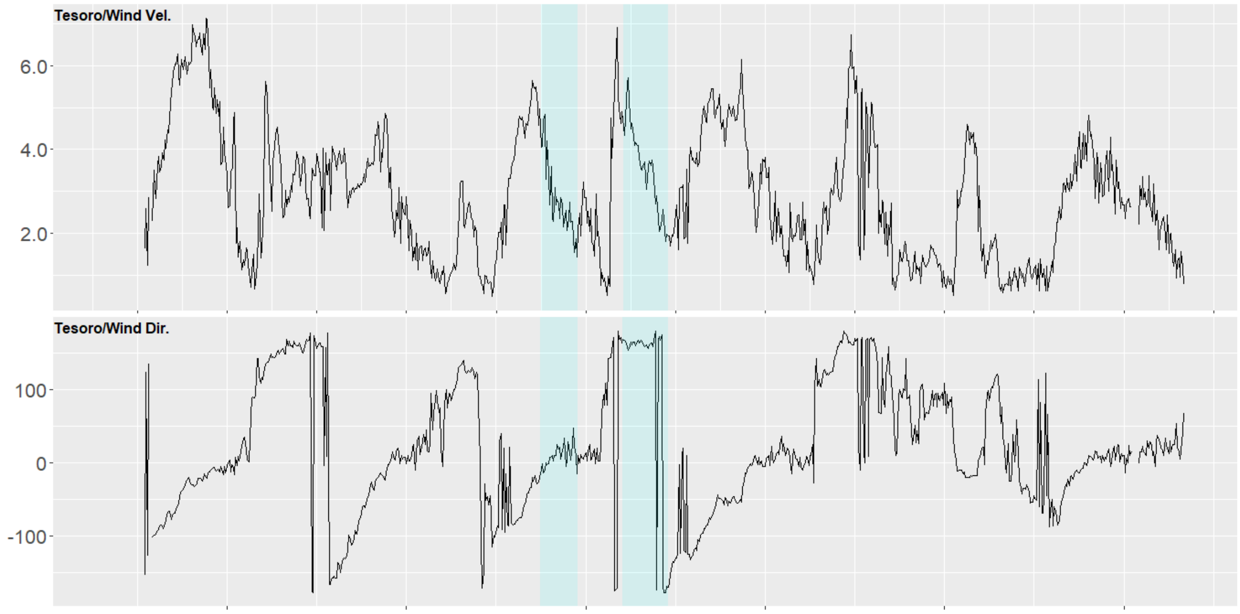

Appendix 8. Video showing atmospheric conditions around San Andrés Island on September 3, 2017.

See attached file: Appendix8_Goes_13_Band6_IR.mp4.